A. COVER PAGE

Project Title: Reducing slip-and-fall accidents in the workplace: Role of small-scale roughness of floor surfaces to improve friction	
Grant Number: 5R21OH012126-02	**Project/Grant Period:** 09/30/2021 - 09/29/2023
Reporting Period: 09/30/2022 - 09/29/2023	**Requested Budget Period:** 09/30/2022 - 09/29/2023
Report Term Frequency: Final	**Date Submitted:** 01/27/2025
Program Director/Principal Investigator Information: KURT E BESCHORNER , PHD BS **Phone Number:** 412-624-7577 **Email:** beschorn@pitt.edu	**Recipient Organization:** UNIVERSITY OF PITTSBURGH AT PITTSBURGH UNIVERSITY OF PITTSBURGH OFFICE OF SPONSORED PROGRAMS PITTSBURGH, PA 152133320 **UEI:** MKAGLD59JRL1 **EIN:** 1250965591A6 **RECIPIENT ID:**
Change of Contact PD/PI: NA	
Administrative Official: JENNIFER E WOODWARD 3520 FIFTH AVE PITTSBURGH, PA 152133320 **Phone number:** 412-624-7400 **Email:** osp@pitt.edu	**Signing Official:** GRETCHEN MADONIA 300 MURDC 3420 Forbes Ave Pittsburgh, PA 15260 **Phone number:** 412-624-2184 **Email:** gam179@pitt.edu
Human Subjects: NA	**Vertebrate Animals:** NA
hESC: No	**Inventions/Patents:** No

B. ACCOMPLISHMENTS

B.1 WHAT ARE THE MAJOR GOALS OF THE PROJECT?

Fall-related injuries burden over 140,000 workers annually, causing significant human suffering and an economic cost of $10 billion in Workers' Compensation. Approximately half of occupational falls are caused by slipping. Slipping is initiated by low friction between the shoe and floor, and commonly occurs in the presence of liquid contaminants (e.g., oil, water). While falling risk varies depending on gait, shoe type, and attentiveness; all workers experience a lower falling risk through the implementation of high-friction flooring. Current approaches to high-friction flooring depend on trial-and-error methods that lead to inefficient design and suboptimal frictional properties. Instead, there is a need for evidence-based understanding of the flooring design factors that control the friction at the shoe-floor interface.

Based on our preliminary studies and the scientific literature on surface topography, we contend that existing models of shoe-floor friction have failed to adequately predict slipping because they do not account for small-scale roughness. Recent analytical models of rubber friction on rough surfaces have conclusively demonstrated the importance of small-scale topography, down to the nanometer scale. Furthermore, our preliminary data has demonstrated that this small-scale topography cannot be measured using conventional techniques, yet it varies widely among current flooring materials. The purpose of this R21 project is to use novel measurements of small-scale floor topography to develop and validate a mechanics-based predictive model for shoe-floor friction. Once this predictive model is established, it will enable the development of high-performance floorings that drastically reduce the incidence of slip-and-falls. The central hypothesis of this project is that variations in small-scale topography, which are unmeasurable using current techniques, account for presently-unexplained friction variations between floor surfaces. The long-term goal of this research is to substantially reduce the incidence of occupational falls by enabling science-based design and maintenance strategies to modify floor topography in order to achieve higher friction. This research is innovative because it will employ novel experimental methods and analysis techniques that have never been applied to flooring surfaces, and because it will develop a mechanics-based model to predict the relationship between floor structure and friction performance, where prior research has relied on empirical correlations. The proposed research leverages newly emerging approaches for surface characterization and analysis established by PI Jacobs, combined with PI Beschorner's leading-edge measurements and modeling of shoe friction. The research consists of two related but independent aims.
Aim 1: Quantify the dependence of shoe-floor friction performance on small-scale topography. This Aim will investigate the ability of small-scale topography to explain variations in shoe-floor friction performance that cannot be explained using current measurement techniques. The friction performance of 20 floor surfaces will be measured using a shoe-floor tribometer that has been validated for predicting human slips. We will use novel topography approaches—based on three techniques: stylus profilometry, cross-section optical microscopy, and scanning electron microscopy (SEM)—to measure surface topography down to the nanometer scale. Spectral analysis will be used to quantify floor roughness by considering the full range of size scales.
Hypothesis 1: Roughness parameters that consider the full range of scales will improve our ability to predict COF values compared with those using just stylus profilometry.
Aim 2: Establish a predictive mechanics-based model for shoe-floor friction based on multiscale surface topography. A multiscale finite element model will be developed to simulate the viscoelastic contributions to friction across all scales from nanometers to centimeters. The model will be developed and validated using 40 different types of flooring: the 20 surfaces from Aim 1 (used to develop the model), plus an additional 20 floor surfaces in Aim 2 (used to validate the model). Samples will be representative of real-world flooring including variations in material and surface treatment. Building on an established 2-scale model developed by the PIs, the new model will integrate topography data across an unprecedented eight orders of magnitude of size. The newly developed model will be compared to a conventional (statistical) model to investigate the following hypothesis:
Hypothesis 2: A mechanics-based model using multiscale topography will more accurately predict shoe-floor friction compared with conventional approaches, i.e., statistical models based on stylus profilometry.
Successful completion of this research will reveal the role of currently-unmeasured topography on shoe-floor friction and establish a valid model of shoe-floor friction that outperforms current methods. Working with an industry trade group, the Tile Council of North America (TCNA), this research will achieve impact by guiding the evidence-based development of high-friction flooring for workplaces. This work addresses priorities in the National Occupational Research Agenda sectors: Traumatic Injury (cross-sector); Services; Healthcare and Social Assistance; Transportation, Warehousing and Utilities; and Wholesale and Retail Trade.

B.1.a Have the major goals changed since the initial competing award or previous report?

No

B.2 WHAT WAS ACCOMPLISHED UNDER THESE GOALS?

File Uploaded : Final Progress Report R21OH012126.pdf

B.3 COMPETITIVE REVISIONS/ADMINISTRATIVE SUPPLEMENTS

For this reporting period, is there one or more Revision/Supplement associated with this award for which reporting is required?

No

B.4 WHAT OPPORTUNITIES FOR TRAINING AND PROFESSIONAL DEVELOPMENT HAS THE PROJECT PROVIDED?

NOTHING TO REPORT

B.5 HOW HAVE THE RESULTS BEEN DISSEMINATED TO COMMUNITIES OF INTEREST?

NOTHING TO REPORT

B.6 WHAT DO YOU PLAN TO DO DURING THE NEXT REPORTING PERIOD TO ACCOMPLISH THE GOALS?

Not Applicable

FINAL PROGRESS REPORT

Principal Investigator Information:
Kurt E. Beschorner, Ph.D.
University of Pittsburgh
Swanson School of Engineering
4420 Bayard St #306
Pittsburgh, PA 15213
412-624-7577
beschorn@pitt.edu

Institution to which award was made:
University of Pittsburgh
Office of Research
123 University Place
Pittsburgh, PA 15213-2303

A.Table of Contents

B.List of Terms and Abbreviations

AFM: atomic force microscopy
A(L): nominal area of contact
$A(\lambda)$: apparent area of contact
B: ratio Δ_i/λ_i
C^{1D}: one-dimensional PSD
C^{iso}: two-dimensional PSD
COF: coefficient of friction
C(q): power spectral density
E: complex modulus (Studies #3 and #4)
E: elastic modulus (study #5)
E^*: composite modulus
E': elastic contact modulus
E'': loss modulus
F: normal force
F_i: Floor *i*
$F_{pulloff}$: pull-off force
G: energy released from elastic deformation (study #6)
G: shear modulus (Studies #3 and #4)
G(q): coefficient incorporating roughness, material properties, speed, and pressure
H: Hurst exponent
L: largest wavelength
M_w: Molar mass
N: ratio of characteristic length and wavelength (ℓ/d)
NCD: nanocrystalline diamond
PDMS: Polydimethylsiloxane
Pk = Reduced peak height
PSD: Power spectral density
P(q): ratio of $A(\lambda)$ to A(L)
R: RMS radius of curvature (study #5)
R: radius of a soft spherical probe (study #6)
Ra = Roughness average
RMS: R_q, root mean square roughness
RMS slope: $\bar{g}$, RMS slope
Rp = Maximum profile peak height
Rq = Root mean square roughness
Rz = Mean roughness depth
SEM: scanning electron microscopy
S_j: Shoe *j*
S_o: macroscopic yield strength
S_y: corrected scale-dependent yield strength
TEM: transmission electron microscopy
UNCD: ultrananocrystalline diamond
Wa = Waviness average
a: contact radius
b: rigid-body displacement
c: prefactor
d: wavelength
e_{el}: elastic energy per unit contact area required to conform to the roughness
h^*: length scale effect
h_p: depth of plastic deformation
$h_{rms}^{(1/2)}$: a geometric descriptor of the rough topography
k: numerical constant

ℓ: characteristic length
m_0: Spectral moment which measures variance
m_2: Spectral moment which measures slope
m_4: Spectral moment which measures curvature
q: wavevector
q_1: largest wavevector
q_L: smallest wavevector
s: length of corresponding path along the contact circle
w_{appr}: work of adhesion for making contact
w_{int}: intrinsic work of adhesion
$w^{(\ell)}$: coarse-grained work-of-adhesion field
w_{loc}: fracture energy
w_{PT}: apparent work of adhesion
w_{retr}: work of adhesion for breaking contact
w_{rms}^2: variance of the random field w_{loc}
$w_{rms}^{(\ell)}$: variance of $w^{(\ell)}$
Δa: excursion from the contact line
Δ_i: amplitude of the composite PSD at wavelength I (index in the power-spectrum array)
$(-\Delta_s)^{1/2}$: fractional laplacian
Θ: angle along the contact perimeter
δA: the contact area swept out by the moving crack front
δG: restoring force
η: areal asperity density
λ: Wavelength
λ_1: smallest wavelength
λ_c: lower (cut-off) wavelength limit available
λ_u: upper wavelength limit available
μ: coefficient of friction
$\bar{v}$: sliding velocity
n: Poisson's ratio
σ_0: normal pressure
ϕ: angle between the sliding direction and the slope direction
ω: Wavevector ($\omega = 2\pi / \lambda$)

C.Abstract

The primary goal of this R21 study was to use novel measurements of small-scale floor topography to develop and validate a mechanics-based predictive model for shoe-floor friction. This project was motivated by the high rate of slip-and-fall accidents and the opportunity for high friction footwear and flooring to ameliorate the impacts of these injurious events. In this research study, we developed novel methods to characterize the topography of flooring across 7 orders of magnitude and characterized time-dependent shoe materials across 9 orders of magnitude. We developed an implementation of a friction mechanics model to predict coefficient of friction based on these inputs. Shoe-floor coefficient of friction data was collected in oily conditions for 184 shoe-floor combinations to assess the ability of traditional roughness metrics as well as mechanics models to predict shoe-floor friction. We implemented both statistical analyses and mechanics-based analyses to determine the predictive ability of floor topography across different scale ranges. The key accomplishment in this study was the validation of such a computational model that predicts the impact of time-dependent shoe materials and scale-dependent flooring topography. This model has high potential for impact given its high degree of accuracy for predicting oily friction, the extensive validation that was performed in this study demonstrating its ability to predict both impacts of flooring and shoe materials, and its low required level of expertise required to use the model. The implementation of the model was made possible because of advances in characterizing flooring surfaces and shoe materials that were facilitated during this research. The model also revealed the scales of flooring topography and the frequencies of shoe

materials that contribute most to oily friction. Thus, findings of the model already have generated knowledge that inform design for footwear and flooring manufacturers.

D. Section 1 of the Final Progress Report: Key Findings

D.1. Significant or Key Findings.

The primary goal of this R21 study was to use novel measurements of small-scale floor topography to develop and validate a mechanics-based predictive model for shoe-floor friction. The key accomplishment in this study was the validation of such a computational model that predicts the impact of time-dependent shoe materials and scale-dependent flooring topography. This model has high potential for impact given its high degree of accuracy for predicting oily friction, the extensive validation that was performed in this study demonstrating its ability to predict both impacts of flooring and shoe materials, and its low required level of expertise required to use the model. The implementation of the model was made possible because of advances in characterizing flooring surfaces and shoe materials that were facilitated during this research. The model also revealed the scales of flooring topography and the frequencies of shoe materials that contribute most to oily friction. Thus, findings of the model already have generated knowledge that inform design for footwear and flooring manufacturers.

Aim 1: Quantify the dependence of shoe-floor friction performance on small-scale topography.

To accomplish this aim, we advanced new methodology of characterizing floor topography across scales including at smaller scales. Quantification across these scales led to new understanding of how surface roughness varies across different flooring scales, its impact on shoe-floor friction, and basic science knowledge on the relationships between topography material properties, and contact dynamics.

Key Finding 1: Multiscale topography contributes to shoe-floor friction and relates to material properties and influences contact mechanics.

Key Finding 2: Combining stylus profilometry combined with an innovative use of scanning electron microscopy, we have characterized surface topography features from a scale of 10 nm to 10 mm.

Key Finding 3: We identified the scales that most contributed to shoe-floor oily friction. Multiscale characterization of flooring tiles (above 10 micron wavelength) outperformed common roughness parameters that primarily focus on a single scale. Sub-micron scale topography did not meaningfully contribute to oily shoe-floor friction.

Aim 2: Establish a predictive mechanics-based model for shoe-floor friction based on multiscale surface topography.

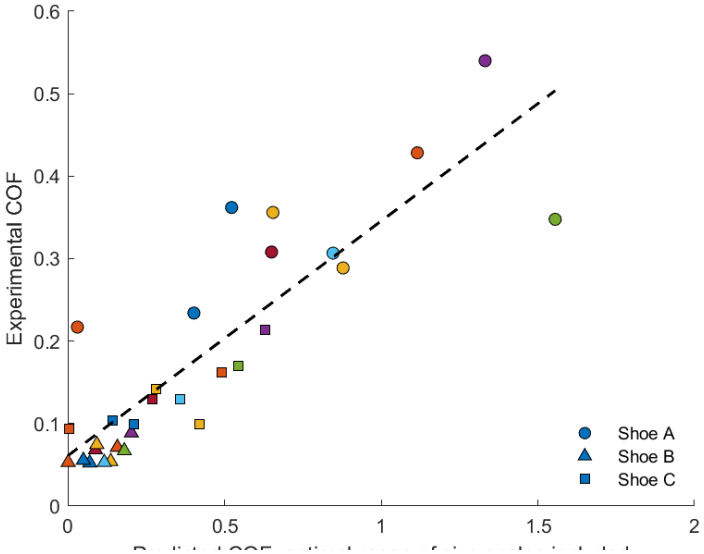

Figure 1: Scatter plot of experimentally-measured COF (y-axis) against predicted COF when excluding small-scale features. Marker types indicate different shoes, while colors represent different flooring.

We implemented methods to utilize a multiscale mechanics model that was highly accurate and represents the most successful modeling effort to date for predicting shoe-floor friction.

Key Finding 4: To benchmark the predictive ability of traditional methods (stylus profilometry), we performed statistical analyses associating these traditional surface parameters (roughness or waviness) on shoe-floor COF. These models were only moderately predictive and were notably less predictive than previously reported in studies that systematically modified surface roughness through sandblasting. Thus, this further motivated the urgent need for rigorous mechanics models since standard roughness measurement methods provided limited information into a floor's friction performance if applied in real world environments.

Key Finding 5: The mechanics-based model accurately predicted oily shoe-floor friction. The RMS error was 40% lower than prior mechanics models and is simpler to use because it does not require expertise associated with finite element modeling. Finally, the present model better simulates the impact of shoe outsole material since it

utilizes dynamic mechanical analysis, which is better at capturing the frequency range that most contributes to friction.
Key Finding 6: We optimized the multiscale mechanics model improving understanding of shoe-floor friction mechanisms, and informing new metrics for shoes and flooring. Specifically, friction was caused by the interaction of topography with length scales above 20 μm up to 10 mm and time-dependent material properties between 1 kHz to 100 kHz. This informs new methods of analyzing surface topography and of measuring shoe material properties that can assist floor and footwear manufacturers in developing and assessing new products.

D.2. Translation of findings:

Translation and dissemination efforts have focused on two pathways: 1) disseminating scientific knowledge to the research community, 2) disseminating knowledge to footwear companies and the flooring industry.
1: Scientific knowledge to research community: This research has been communicated to the scientific community through 6 peer-reviewed published manuscripts (1 more in review and 2 more in preparation), and an MS published dissertation. One talk included a Keynote lecture at the Qualicer meeting (Barcelona, February, 2024).
2. Dissemination to footwear designers: Research has been communicated via one-on-one meetings with five footwear companies. In addition, the research was presented at Footwear Biomechanics Symposium, which is largely attended by footwear brands. The research was also disseminated to flooring companies via the Tile Council of North America who we met with routinely to discuss progress and findings. The keynote at the Qualicer Meeting (described in the prior section) was well attended by footwear manufacturers.

D.3. Research Outcomes/Impact.

D.3.1. Potential outcomes

We anticipate that the model developed in this study will lead to a reduction in slip-and-fall accidents because footwear companies will be able to produce footwear with higher friction performance. Specifically, this research guides the development and selection of materials with higher friction performance. We have already partnered with a footwear company (Decathlon) on this research. We expect to engage with other footwear companies who will implement this model and use testing methods informed by our research (i.e., testing outsole material viscoelastic properties at the frequency identified in this study). Thus, this study is expected to affect shoe design as an intermediate outcome and reduce slips as an end outcome.

D.3.2. Intermediate outcomes:

None but intermediate outcomes are anticipated in the next 3-4 years**.**

D.3.1. End outcomes: None

Barriers and obstacles impeding progress

1. Multiscale models using finite element methods could not be verified

We originally intended to develop the model using finite element methods based on our prior work. After creating topography with more realistic shapes (i.e., using a sinusoidal surface instead of a sawtooth surface), this method was unable to match trends observed in empirical data. We therefore pivoted to a different model that has been widely used in the tire industry but rarely used for shoes.

2. Small-scale features did not contribute to shoe-floor friction

Contrary to our central hypothesis at the beginning of the study, small-scale features did not meaningfully contribute to shoe-floor friction. In fact, the predictive ability of the shoe-floor friction models improved when small-scale topography was omitted. This also is a fortunate outcome since measuring small-scale topography requires specialized equipment and expertise.

Section 2 of the Final Progress Report: Scientific Report.

E. Methodology, Results and Discussion

E.1. Study #1: The need for better metrics for floor-tile topography: Conventional metrics correlate only modestly with shoe-floor friction [1]

E.1.1. Methods

E.1.1.1.Materials

In this study, 26 porcelain tiles were originally evaluated to determine their surface roughness and shoe-floor COF. During the study, three of the tiles were identified as exterior (outdoor) tiles, which were determined to have a fundamentally different surface than indoor tiles and were excluded from the analyses leaving 23 remaining indoor tiles (26 – 3 excluded tiles). The tiles were sourced across 3 manufacturers and within manufacturers, the tiles had different finishing processes and/or different product lines. Four of the included tiles were known to be made of an unglazed porcelain, 9 tiles were glazed, and the glaze status of the remaining 10 tiles was not disclosed by the tile manufacturer. Four shoes were used in the friction measurements, differing in style, material, tread pattern, and advertised slip resistance. These shoes included Rockport K71224 (Shoe A, Hardness: 53), Vans Off the Wall Old Skool Skate Shoes 721278 (Shoe B, Hardness: 52), the SRMax Atlanta Men's Soft Toe SRM 3700 (Shoe C, Hardness: 52), and the DS Work Service 6671 (Shoe D, Hardness: 59). Prior studies have reported viscoelastic material properties for three of the four shoes in this study ([2], Shoes A, C, and D in the present study correspond with Shoes B, C, and A, respectively, in the cited study). All shoes were approximately Men's Size 9 or Women's size 10. The shoes were selected based on prior COF results. These shoes spanned friction performance (high and low values of the measured COF) and two categories of labeling ("slip resistant" as labeled by their manufacturer and not labeled slip resistant). The basis for selecting a high- and low-COF shoe was made from experimental results of our past research [3, 4].

Table 1: List of tile products included in the study. The tile manufacturer is listed along with the product line and the described finish type. The code is used to identify the product throughout the manuscript.

Manufacturer	Tile Product	Finish	Tile Code
Crossville	Graphite	Polished	BPOL
Crossville	Graphite	Unpolished Sheen	BUPS
Fired Earth	Piemonte	Matte	PPM
Fired Earth	Piemonte	Polished	PPP
Fired Earth	Piemonte	Satin-Bone	PBS
Fired Earth	Piemonte	Satin-Pearl	PPS
Crossville	Roasted Chestnut	Polished	APOL
Crossville	Roasted Chestnut	Unpolished Sheen	AUPS
Crossville	Venho Verde	Unpolished Sheen	CUPS
Fired Earth	Umbria	Polished	UMBP
Fired Earth	Umbria	Matte	UMBM
Fired Earth	Umbria	Satin	UMBS
Fired Earth	Lombardia	Polished	LMBP
Fired Earth	Lombardia	Matte	LMBM
Fired Earth	Lombardia	Satin	LMBS
Crossville	State of Grace	Unpolished Sheen	FUPS
Crossville	State of Grace	Satin	FSAT

Crossville	Juno	Unpolished Sheen	EUPS
Crossville	Juno	Honed	EHON
American Wonder	Asher Haze	Finish 1	AH1
American Wonder	Asher Haze	Finish 2	AH2
American Wonder	Venato	Polished	VPOL
American Wonder	Polar Style	White	PSW

E.1.1.2.Measurements of coefficient of friction

The COF was measured using the STEPS machine (XRDS Systems, LLC, Andover, MA) [5], which applies horizontal and vertical forces, to slide the shoe across a flooring sample and apply a normal force, respectively (Figure 1). A force plate under the flooring sample measures reaction forces, and the sliding speed of the shoe is measured by feedback from the horizontal motor. The tests were conducted using a shoe-floor angle of 17° (+/- 2) and a sliding speed of 0.5 m/s with a vertical applied force of 250 N (temperature: mean of 23°C with a standard deviation of 1.9°C; relative humidity: mean of 37% with a standard deviation of 13%). The force and speed parameters were held within 10% over a 50 ms test duration. Prior research has found that the under-shoe conditions at the moment of slip onset are approximately a shoe-floor angle of 15-24 degrees, a slipping speed of about 0.1 to 0.3 m/s that rapidly increases in speed during the slip, and a vertical force of approximately 130-320 N [6, 7]. Validation studies determined that testing conditions of 17° shoe-floor angle, 0.5 m/s, 250 N vertical force, and an averaging time of 50 ms produced the best predictions of human slips [6, 8] and repeatable results [8]. All tests were performed with a contaminant of canola oil (61.2 cP [5]) to reduce adhesion and isolate hysteresis friction [9, 10]. Prior research has found that canola oil leads to consistently low COF relative to other common contaminants [4, 11-13]. This finding is true even for shoes with tread [5, 12] that have minimal hydrodynamic effects [14-16] suggesting that these low COF results are due to a reduction in the adhesion component of friction. Furthermore, modeling studies have found that hysteresis friction predictions correlate well with oily friction [9, 17] suggesting that hysteresis friction is the dominant mechanism in oily conditions.

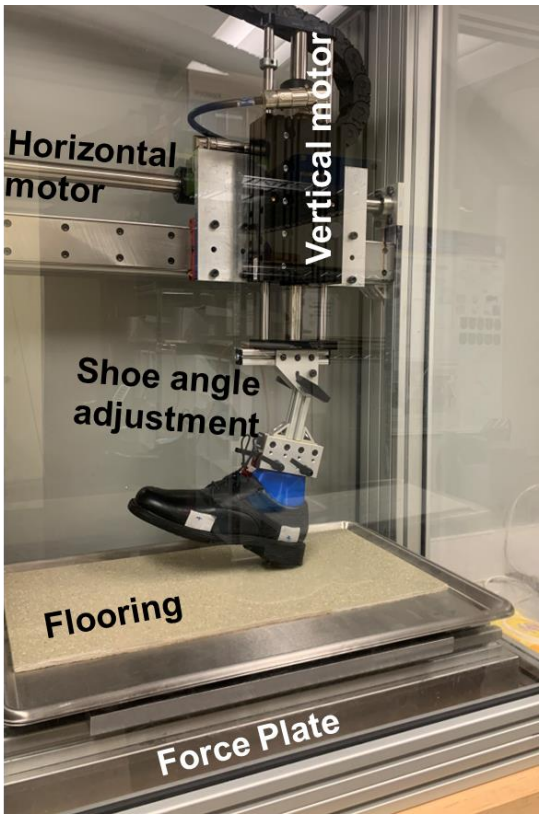

Figure 1: STEPS device used to measure shoe-floor COF. The vertical and horizontal motors create the motion profile, the shoe-floor angle adjustment is used to adjust the shoe to the specified angle and then locked during trials, and the force plate measures the ground reaction forces.

Three trial replicates were repeated over three different days (nine trials total) for each shoe/floor combination. The tiles and shoes were cleaned after each day of testing. The canola oil was poured onto the floor surface beneath the landing area of the shoe and was sufficiently thick that adding additional fluid did not increase the surface thickness. The canola oil was spread and reapplied as needed between tests to ensure consistent coverage.

The COF was calculated by averaging the ratio of the horizontal force to the normal force over the 50 ms testing period (Figure 2). COF values were averaged across all 9 trial replicates and sessions. The COF values were averaged over these nine trials. Preliminary review of the data revealed that COF values scaled to the performance of the four different shoes leading to highly variable COF values across shoes (Figure 3A). The relative performance between flooring surfaces was consistent across all of the shoes (i.e., a high-COF floor as measured with one shoe also tended to have relatively higher COF with other shoes). To remove the variation caused by the shoes, the COF values for tiles were scaled (*Scaled COF (F_i, S_j), Eq. (1)*) the scaled COF value (for flooring F_i and shoe S_j) relative to the average COF value across all tiles for a single shoe (*mean(COF(S_j))*: the mean COF value for shoe S_j, horizontal lines on Figure 3A); a process that was repeated for each shoe (i.e., each shoe-floor COF value was divided by the average COF value across all tiles for that particular shoe) (Figure 3B). By using scaled COF to remove the variation across shoes, we were able to reduce the coefficient of variation (across shoes, within each flooring) from a mean of 93% (based on raw COF values, Figure 3A) to a mean of 10.0% (based on scaled COF values, Figure 3B). This enabled us to accomplish the stated purpose of establishing the relationship between floor roughness and shoe-floor COF while reducing variation caused by the shoe design.

$$Scaled\ COF\ \left(F_i, S_j\right) = \frac{COF\left(F_i, S_j\right)}{mean\left(COF\left(S_j\right)\right)} \qquad \text{Eq. (1)}$$

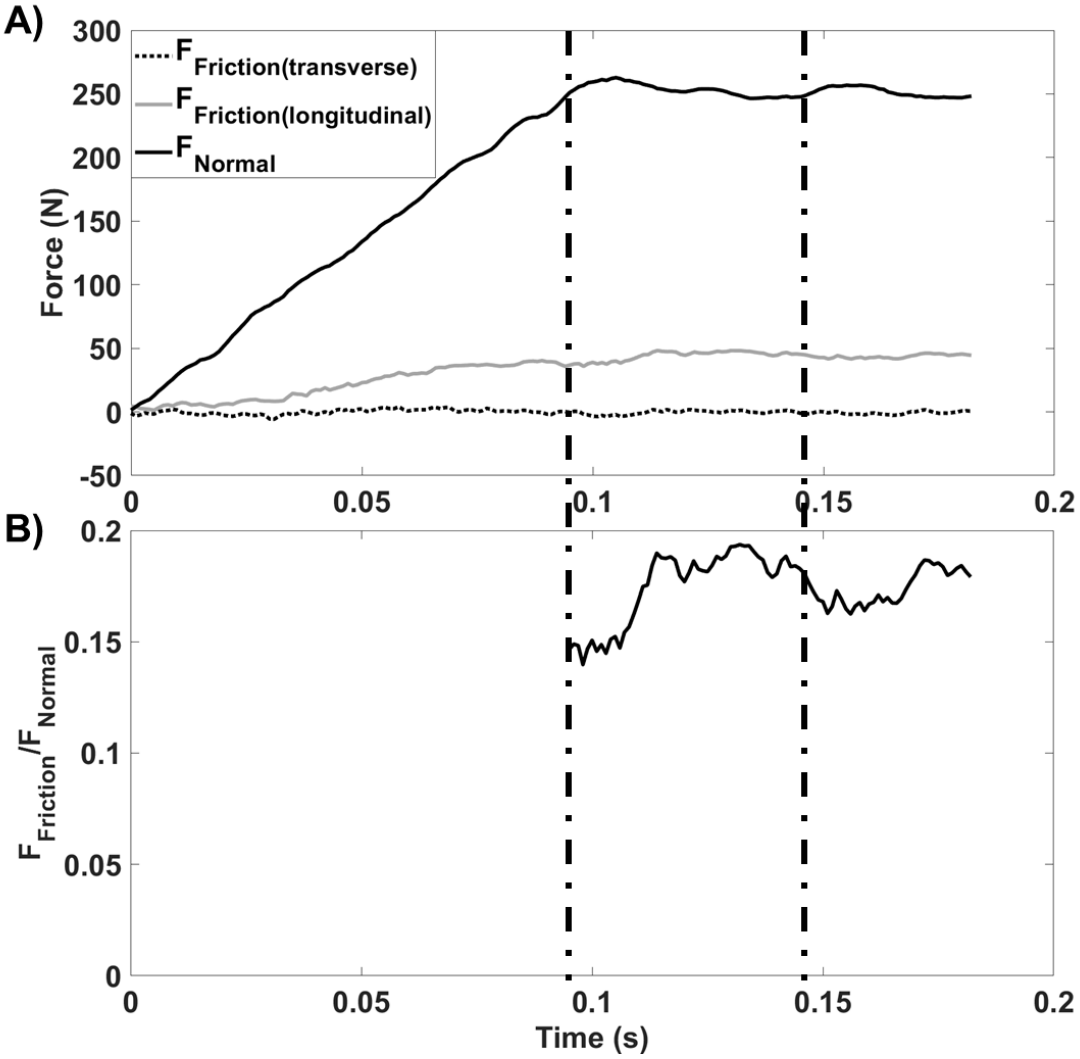

Figure 2: Representative kinetic data from a shoe-floor friction trial. A) The time-series data for ground reaction force, where 0 s represents shoe contact with the floor surface. Both the longitudinal friction (in the direction of sliding) and the transverse friction (perpendicular to the direction of sliding) were measured. B) The time-series of the ratio of the resultant friction force to the normal force. The COF was calculated as the average of this time-series data over a 50 ms period (between the two vertical lines).

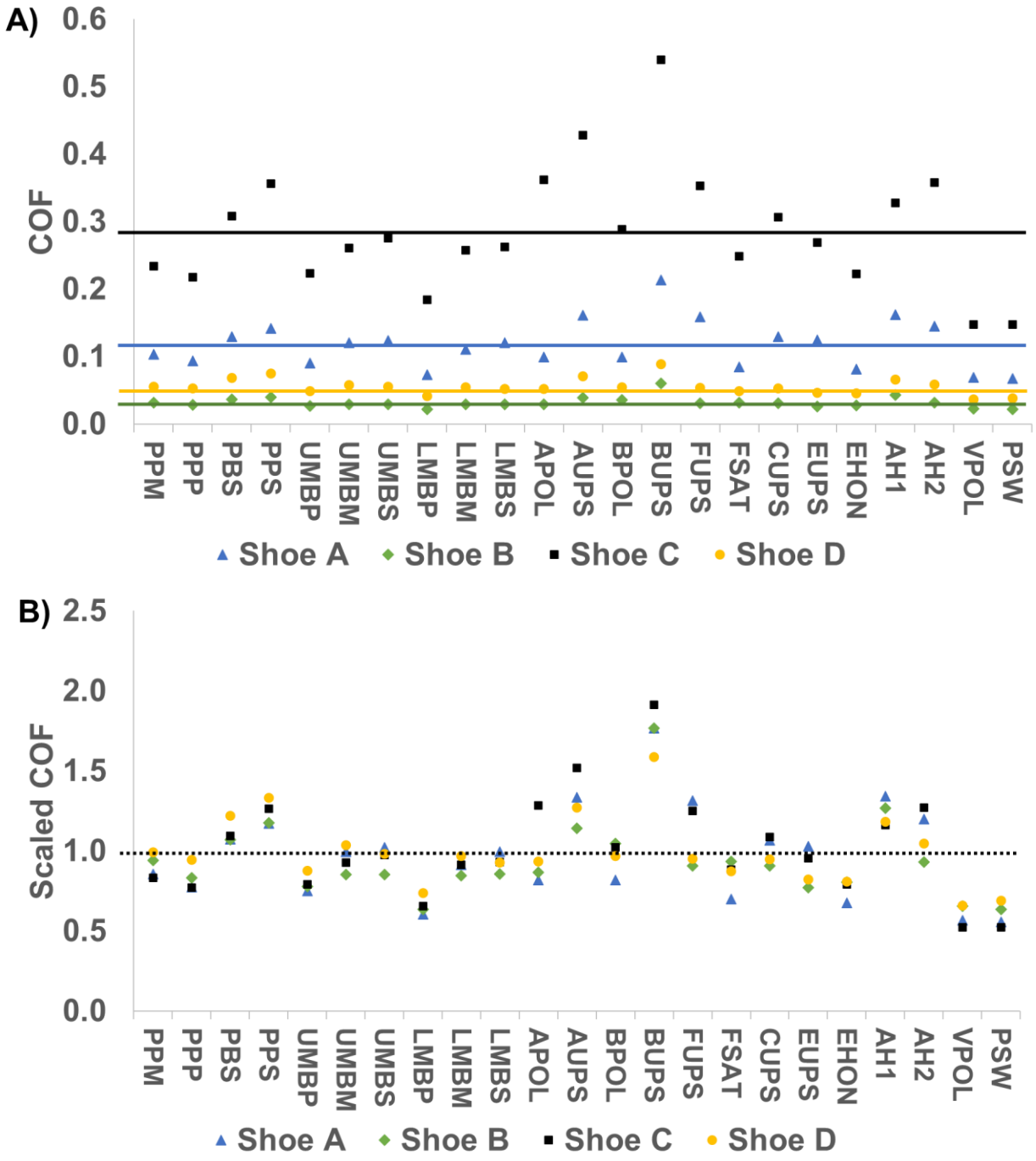

Figure 3: Friction performance between floors (along x-axis) and across shoes (different markers). A) In this graph, the y-axis represents the measured COF values and the horizontal lines represent the mean COF for a particular shoe (top to bottom: Shoe C, Shoe A, Shoe D, Shoe B). B: In this graph, the y-axis is the scaled COF (Eq. 1), such that the mean value for all shoes must be equal to one (horizontal dashed line).

E.1.1.3.Measurements of surface topography

Surface topography data for the porcelain were collected on a stylus profilometer (DektakXT, Bruker, Billerica, Massachusetts, USA). One-dimensional line scans were taken at different scanning speeds ranging from 1 µm/s to 60 µm/s (Figure 4a-g). A total of 18 measurements were taken for each flooring surface at 6 different scan lengths, 0.05, 0.15, 0.3, 1.5, 3, 10 mm with three repetitions each.

The lateral spacing of data points ranged from 40 nm to 2 µm. The radius of the stylus profiler was measured using scanning electron microscopy (Fig. 4h) and determined to be 1.46 µm. The stylus measurements were collected with random orientations with respect to the tile edges, and did not show any significant variation with direction. To remove the tilt of the sample and the bowing artifact from the tool, a parabolic correction was applied to all the measurements. The corrected height measurements are shown in Figure 4a-g. All surface measurements have been made publicly available via DOI (see Data Availability), to enable others to examine and reuse the topography data, following FAIR data practices [18].

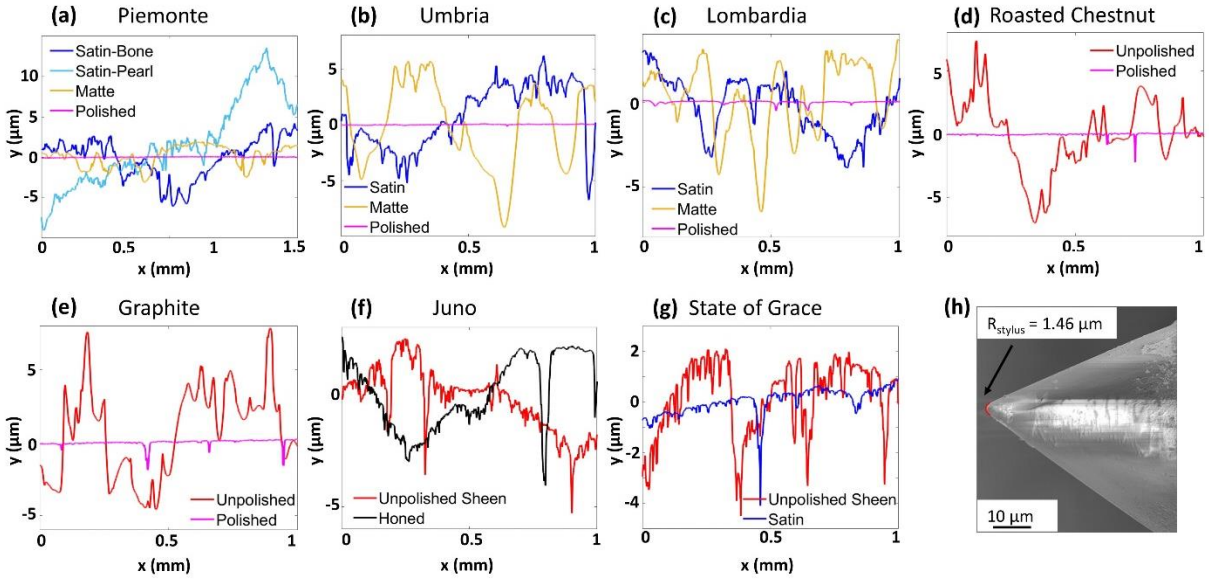

Figure 4: Surface topography was measured using a stylus profilometer. Representative images are shown here comparing different products and polishing conditions. The end-radius of the stylus tool was measured using a scanning electron microscope (Sigma 500VP, Zeiss, Oberkochen, Germany) at 1000X magnification with the secondary-electron detector.

Common roughness parameters were computed according to ASME B46.1 [19]. According to this standard, the raw measured profile is filtered such that small-wavelength “noise” is removed, resulting in the “primary profile,” which is used to compute *P* parameters such as P_a, P_q, etc. This profile can further be filtered into the smaller-scale “roughness,” which is used to compute *R* parameters, and the larger-scale “waviness,” which is used to compute *W* parameters. In the present investigation, four parameters were reported, R_a, R_q, R_p, and W_a, where the subscript *a* designates the arithmetic average deviation from the mean line, and the subscript *q* designates the root-mean-square deviation from the mean line, each for the respective profile (*R* or *W*). R_p designates the maximum height of the profile above its mean line as measured in the analyzed region. These four parameters were chosen because they have previously been suggested to correlate with friction performance [20]. Bruker’s Vision64 mapping and analysis software was used to compute these parameters, with cutoff wavelengths chosen per ISO 4287. For a stylus measurement of a surface with an R_a of approximately $0.02<R_a<10$ µm, the “noise” cutoff is set to 8 µm, and the roughness-waviness cutoff is set at 2.5 µm. The evaluation length was set at half of the scan length.

E.1.1.4.Statistical analyses

Bivariate correlation analyses (Pearson) were performed comparing the roughness parameters R_a, R_q, W_a, and R_p to the scaled COF for each tile (i.e., averaged across the four shoes). Nonparametric correlation analyses were used to supplement the Pearson analyses since the roughness parameters were slightly positively skewed. The r-values and p-values for each correlation were assessed to determine significance of the correlation. Pearson correlation analyses were

performed across the roughness parameters to determine the degree of covariation across these parameters. The significance level was set at 0.05 (i.e., 95% confidence).

E.1.2. Results

The average COF observed across the porcelain tiles was 0.123 and ranged from 0.022 to 0.540. The COF values across all shoe-floor conditions had a standard deviation of 0.111. The average scaled COF across these tiles was 1 (by definition), with a minimum of 0.515, a maximum of 1.89, and a standard deviation of 0.272 across tiles. The average roughness value for R_a was 1.9 µm (range of 0.0 to 7.3 µm, standard deviation of 1.7 µm), for R_q was 2.4 µm (range of 0.0 to 8.6 µm, standard deviation of 2.0 µm), for R_p was 4.7 µm (range of 0.1 to 15.0 µm, standard deviation of 4.4 µm), and for W_a was 1.6 µm (range of 0.1 to 5.7 µm, standard deviation of 1.5 µm). The dataset is available as Open Access [21].

Positive but weak correlations were observed between each roughness parameter and the COF, with r-values between 0.374 and 0.760 (Figure 5). The r value (t-value, p-value, RMS error of scaled mean COF) between COF and each roughness parameter were as follows: R_a was 0.546 (t_{21}=2.99; p=0.007; RMSE=0.224), R_q was 0.535 (t_{21}=2.90; p=0.009, RMSE=0.226), R_p was 0.760 (t_{21}=5.36, p<0.001, RMSE=0.174), and W_a was 0.374 (t_{21}=1.85, p=0.078, RMSE=0.248). Similar results were observed using nonparametric analyses. Each of the parameters were correlated with each other, with r-values ranging from 0.649 (between R_p and W_a) to 0.991 (between R_q and R_a) (Figure 6). The correlation between all roughness and waviness parameters had a p-value of less than 0.001.

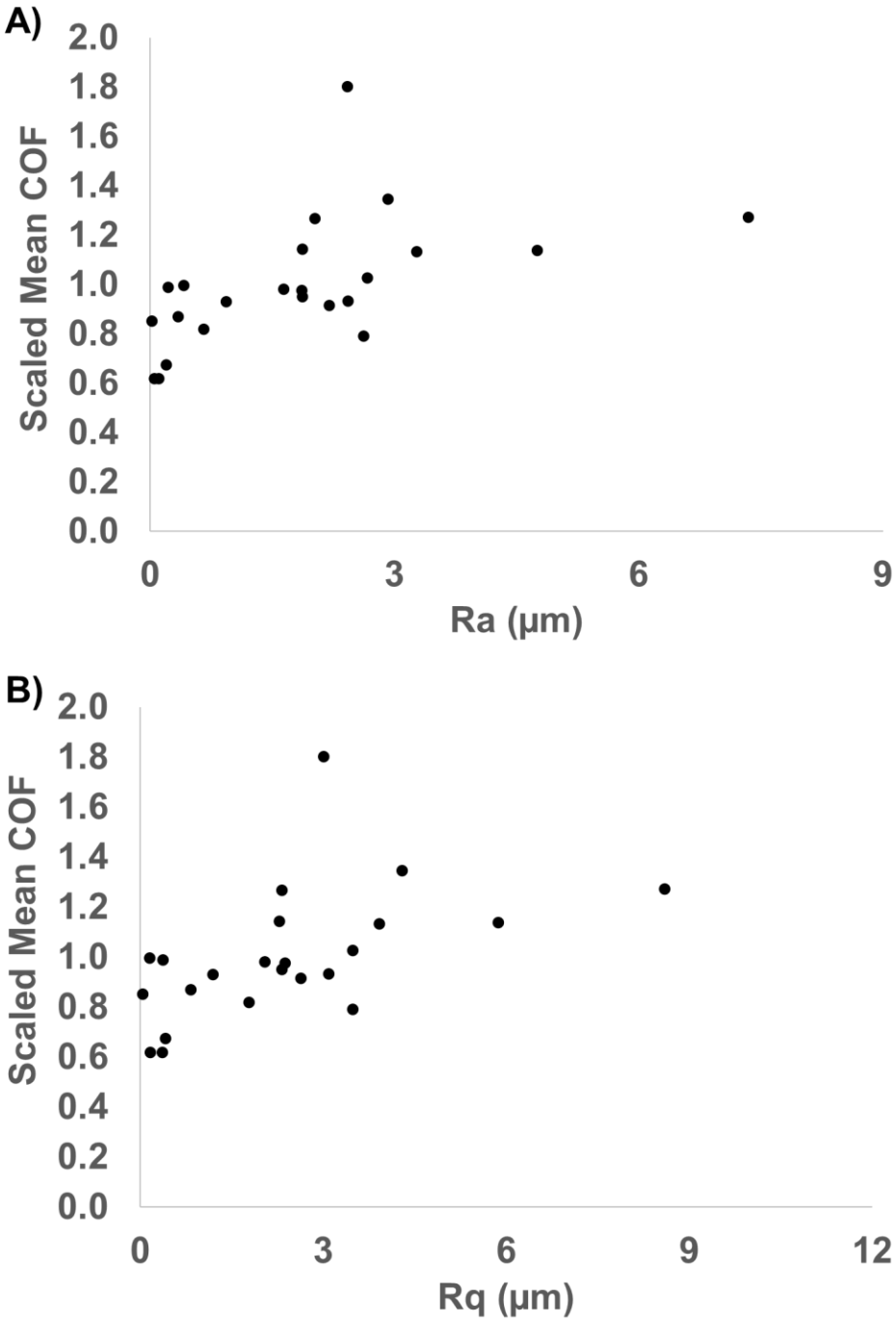
A)
Scaled Mean COF
2.0
1.8
1.6
1.4
1.2
1.0
0.8
0.6
0.4
0.2
0.0
0
3
6
9
Ra (μm)
B)
Scaled Mean COF
2.0
1.8
1.6
1.4
1.2
1.0
0.8
0.6
0.4
0.2
0.0
0
3
6
9
12
Rq (μm)

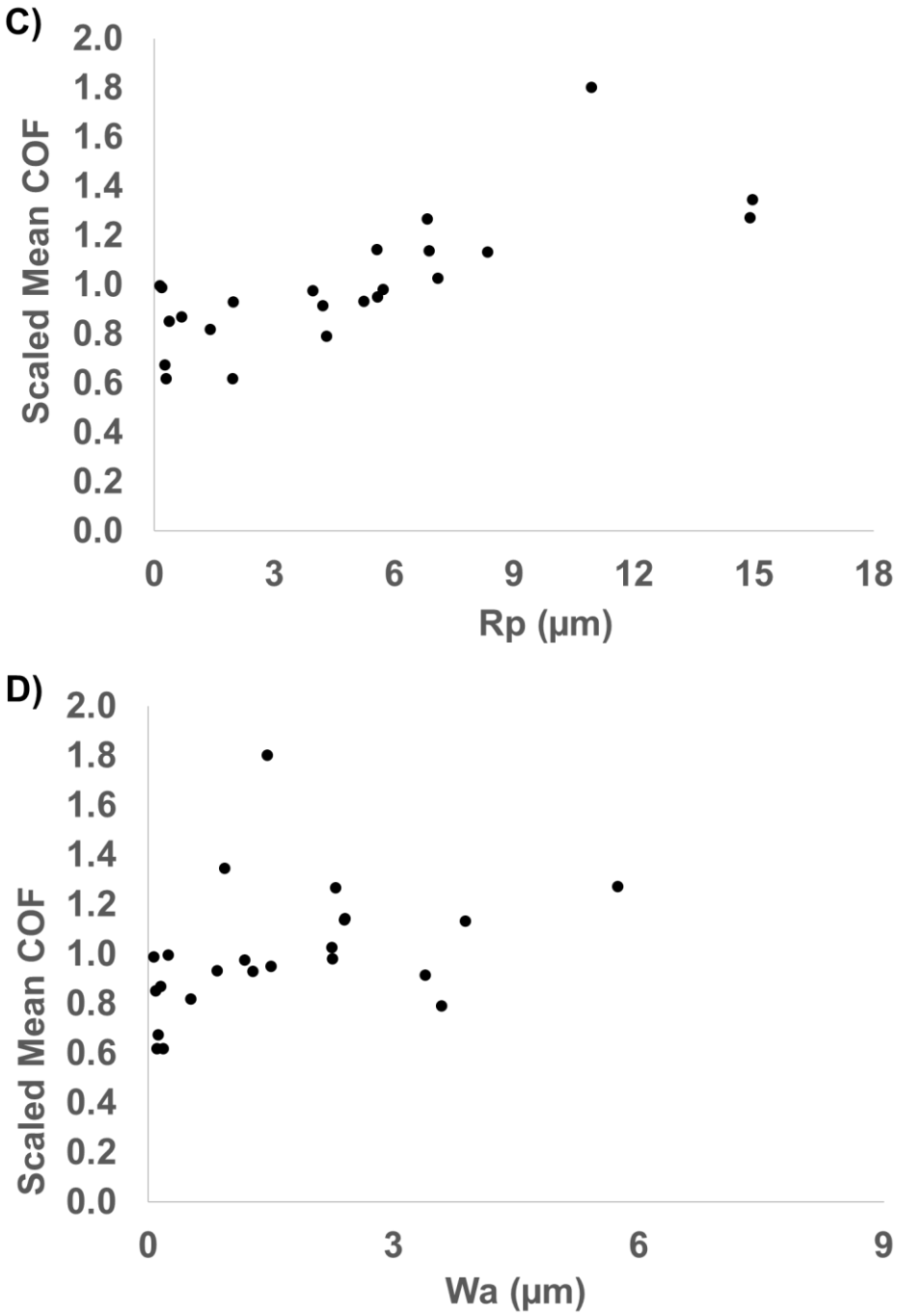

Figure 5: Correlations between roughness parameters (x-axis) and the scaled mean COF values (y-axis). The scaled mean COF values were the scaled values (Figure 3B) averaged across the four shoe conditions. Different panels represent different roughness parameters: A) R_a, B) R_q, C) R_p, D) W_a.

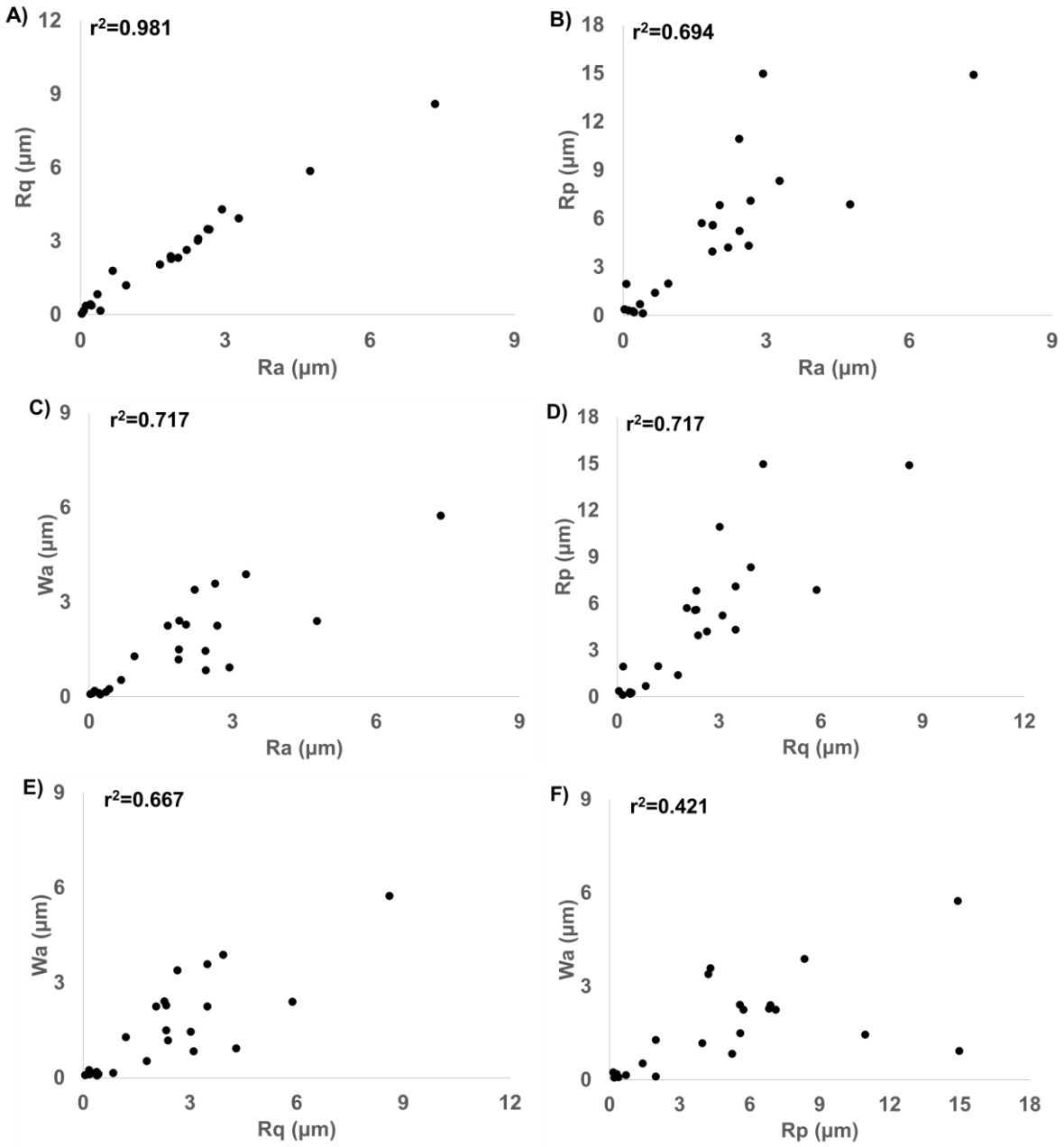

Figure 6: Correlations across roughness (R) and waviness (W) metrics. A) Correlation between R_q and R_a; B) correlation between R_p and R_a; C) correlation between W_a and R_a; D) correlation between R_p and R_q; E) correlation between W_a and R_q; F) correlation between W_a and R_p.

E.1.3. Discussion

Positive yet modest correlations were observed between COF performance and roughness values. These results indicate that the scale of roughness that can be measured by a profilometer and parameterized are correlated with the friction results but lack critical information needed for accurate predictions. Notably, the best-fit lines were associated with an RMS error of between 17% and 25% of the mean COF. The correlations across roughness parameters were also strong, indicating redundant information across the roughness parameters. As such, the strength of the correlations was similar across the roughness parameters.

The results from this study were consistent with results from previous research indicating weak correlation between large-scale roughness and shoe-floor friction. The correlations found here were weaker than those of the research discussed earlier on systematically modified (e.g., sandblasted)

surfaces [11, 20, 22, 23], but are consistent with research that examined a cross-section of flooring products [24]. Moreover, these weak correlations may explain why Verma et. al. did not find a significant correlation between floor roughness and actual slip rate in real-world restaurants where flooring product heterogeneity is likely [25].

The positive correlations between roughness parameters and coefficient of friction are typically explained by hydrodynamic or viscoelastic mechanisms, and this investigation sheds further light on this mechanism. First, prior flooring roughness research has suggested that a primary mechanism connecting roughness to friction performance is a hydrodynamic effect where larger void volumes (associated with higher peaks) permit greater drainage capacity during the squeeze-film effect and reduce the impact of hydrodynamic pressures [20, 22]. Second, prior modeling studies [9, 17, 26, 27] have demonstrated that higher peaks generate greater deformation. This greater deformation is associated with increased energy loss and friction due to viscoelastic hysteresis. For the present results, if the first (hydrodynamic) mechanism were dominant, then the impact of roughness would be expected to be greater for shoes where hydrodynamic effects were large and lesser for shoes where hydrodynamic effects were small. However, an increase in friction performance was observed in the present study despite the use of slip-resistant shoes, which are known to be associated with minimal hydrodynamic effects [14, 28, 29]. Therefore, we propose that the critical mechanism connecting roughness to oily friction performance is the deformation caused by the floor asperities into the shoe material.

Furthermore, this material deformation mechanism provides a logical basis for why Rp had the strongest correlation. The conforming of the shoe material to the floor surface would indicate that the shoe must deform around the contour of the asperity peaks whereas the shoe material may fail to fill in the valleys of the flooring. Thus, peaks (well captured by Rp) may contribute to friction more than valleys. On the other hands, parameters like Ra, Rq, and Wa that give equal weight to valleys as peaks, may be capturing topographical information that is less relevant to friction. Additional modeling of viscoelastic hysteresis and its ability to predict experimentally measured coefficient of friction may provide increased evidence for this proposed mechanism.

Multiple sources may account for unexplained variance in our study. First, the roughness or waviness parameters captured by a stylus profilometer provide statistical descriptions of the surface that may not fully capture all relevant features. Specifically, stylus profilometry captures larger-scale features and is missing the smaller-scale features, which likely contribute to friction [27]. Prior models of friction integrate across length scales [26, 27] indicating that smaller-scale features should add friction to the larger-scale features. Interestingly, the measured friction level was still >60% of the mean friction even at roughness levels approaching 0 (Figure 5). This surprisingly high friction even in the apparent absence of roughness indicates a source of unexplained friction that could arise from small-scale features of flooring that are undetectable by stylus profilometry and/or not captured by the metrics used in this study. Furthermore, research by Ding *et al.* identified that information about roughness at one scale is not predictive of roughness at smaller scales, so it cannot be assumed that the unmeasured smaller scales will vary systematically with the measured larger scales [30]. Shoes have a frequency-dependent viscoelastic response, which adds further weight to the suggestion of the important contribution of a variety of size scales to viscoelastic hysteresis friction [26, 27].

Other potential, though likely smaller, sources of unexplained variance may be the role of hydrodynamic pressures, other topographical features that could be captured with stylus profilometry but are not included in the roughness parameters using in this study, adhesion, and differences across shoe designs. Previous researchers have hypothesized that topography may create channels for fluid to disperse and may be relevant in the presence of hydrodynamic effects [20, 31]. As mentioned previously, hydrodynamic effects are unlikely to be present for the slip-resistant shoes [15, 32], which have consistent tread channels (Shoes C and D) and likely only impacted the shoes with fewer tread features (Shoes A and B). Thus, these pressures may contribute to some unexplained variance. Unexplained friction variation may also occur because the roughness metrics do not consider the number of asperities. The number of floor asperities may affect the contact pressure at each asperity [33] (fewer asperities would increase the contact pressure) and therefore may influence friction [17, 34]. Adhesion that is not blocked by the fluid lubricant is expected to be small [10, 11] but is another potential source of unexplained variance. Lastly, features of the shoe (tread geometry and material)

may also contribute to unexplained variance although the consistency in floor performance across shoes indicates that this contribution is small.

This study adds to the body of evidence suggesting that care should be taken when attempting to make design recommendations for slip-resistant floors based solely on the common surface metrics that are calculated from stylus profilometry measurements. The correlation between roughness parameters measured by stylus with COF performance, although positive, is not strong enough to warrant using these measurements in place of friction measurements. Documents have been released by SlipSTD, making classification groups for surfaces depending on their roughness Pk value and surface profile; they also make some suggestions for where these different floor groups are appropriate for installation [35]. This group also suggested that the Rz roughness parameter of floors in pedestrian areas should be monitored for maintenance notification purposes. While the present study found correlations between Rz and friction performance, further work is necessary to achieve better prediction of flooring to keep workers safe. New methods and/or new metrics may be required to more accurately predict shoe-floor friction and to keep people safe from slip-and-fall accidents.

This study has limitations that should be considered. While the study used more widely varying floor products than many previous studies, the only materials included were porcelain. The correlations may be even poorer when considering a more heterogenous set of materials including polymer-based tiles or natural stone tiles. Canola oil was the only contaminant used in this study. When considering less-viscous fluids, where adhesion would have a stronger contribution to friction, other phenomena would become relevant including the spreading coefficient of the surface-fluid combinations [36, 37] and the material- and topography-dependent real-area of contact [9, 38, 39]. Lastly, validation of the COF results using human slip responses would provide additional validation on the role of roughness on human safety.

E.1.4. Conclusion

This study demonstrates that commonly used roughness parameters from stylus profilometry are only somewhat correlated to friction and do not represent a reliable method of predicting the shoe-floor coefficient of friction. It is anticipated that considering additional scales of topography could enhance predictions and be useful for designing and developing new flooring surfaces. This study indicates that, in the development of slip-resistant flooring or the monitoring of existing floor surfaces, direct measurements of COF will have more utility than utilizing common roughness parameters as a proxy measure for COF performance.

E.2. Study #2: Evaluating scanning electron microscopy for the measurement of small-scale topography

E.2.1. Methods

E.2.1.1. Experimental methods: Preparing samples for SEM topography

The present investigation employs and compares various methods for creating a sample for SEM investigation. Cross-sectioning is a commonly used technique in materials science for revealing the internal structure of a material, and the same general approach can be used to reveal the surface topography. As described in Khanal *et al.* [40], this is an effective technique as long as efforts are taken to preserve the original surface and prevent damage. The cross-section approach requires time and effort to perform but has the advantage that it can be performed on any part, component, or sample. By contrast, Khanal *et al.* [40] also described the “wedge-deposition method”, where a material is deposited on a wedge or thin blade, and then imaged in profile. As discussed at length in Ref. [40] the wedge-deposition approach is significantly simpler, requiring no sample preparation at all; but it has the disadvantage that it only applies for materials that can be deposited (for instance, coatings that are deposited by evaporation, physical vapor deposition, chemical vapor deposition, spray coating, etc.). In Khanal *et al.*, one method for cross-sectioning was compared to the wedge-deposition method using TEM. By contrast, the present work uses SEM instead of TEM (harnessing the advantages discussed above), and compares four separate methods of sample creation, as shown in Fig. 7.

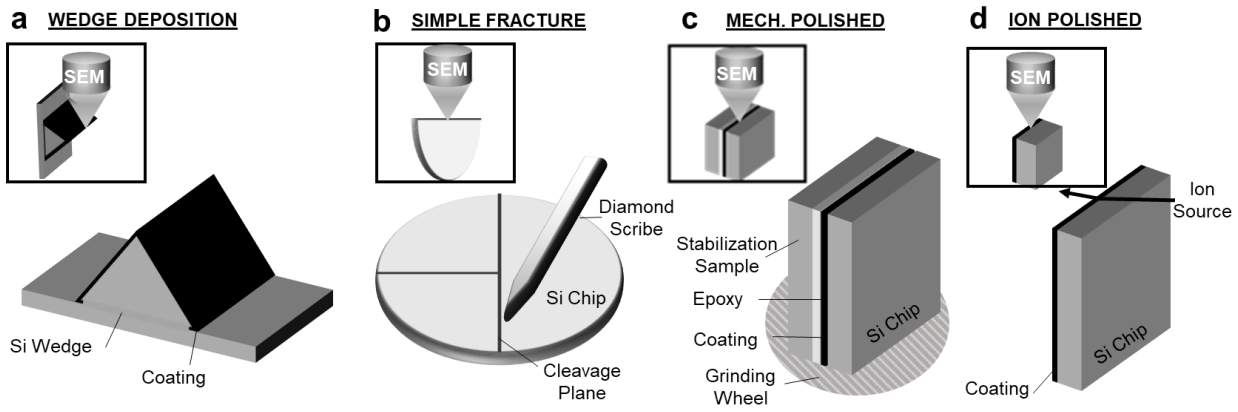

Figure 7: Four different options for sample-preparation were evaluated and compared. (a) Method 1: The "wedge-deposition" method involves coating a wedge or thin blade with the material of interest and then imaging the apex of the wedge in profile in the SEM. It requires no further sample preparation and is applicable to any material that is deposited as a coating, for example those fabricated using physical vapor deposition, chemical vapor deposition, or spray coating. (b) Method 2: The "simple-fracture" method involves scribing the material of interest and then controllably breaking the material into pieces, exposing the fractured surface. This method involves little sample preparation, and is applicable to any brittle material, for example, silicon wafers and other functional materials used in electronics. (c) Method 3: In the "mechanical-polished" method, the sample is mounted in resin and subjected to grinding and polishing, as is common in materials science. This is often known as "metallographic sample preparation," and is quite a general technique which can be used on metal samples, but also ceramics, polymers, composites, and many other materials. (d) Method 4: Finally, the "ion-polished" method uses grazing-incidence ion milling to gently remove material without significant damage. It is the most time- and equipment-intensive technique but is useful for samples that suffer damage during polishing or otherwise are inapplicable for the other sectioning techniques.

In the present investigation, the same ultrananocrystalline diamond surface was prepared using each of the four techniques described in Fig. 7. While these techniques are extensively documented in other works, a brief description of their implementation will be included here. First, in Method 1, a sample was created using the wedge-deposition method (Fig. 7a), exactly as described in Khanal et al. *[40]*. A microfabricated wedge (Hysitron Picoindenter wedge substrates, Bruker, Billerica, MA) was coated with UNCD, deposited using a tungsten hot-filament chemical vapor deposition system with parameters as explained in Ref *[41]*. The wedge-deposition method is simple to perform, requiring nothing more than the addition of a witness sample to the chamber where the deposition is occurring. The witness sample can be a wedge, similar to the one used here, but could also be any sharp blade-like sample, including a razor blade or a thin foil of metal. The only relevant consideration is that the coating on the witness sample should be representative of the coating on the real-world use-case. This may require matching the material of the witness sample to that of the use-case, and/or matching the height and other conditions during the deposition.

The same material was also used to create cross-section samples. In particular, a silicon wafer was inserted in the same deposition run that was used for the wedge-deposition sample (described above), ensuring that the material is as similar as possible. The coated silicon wafer was then used to create cross-sections in three different ways. In Method 2, the simple-fracture method was used (Fig. 7b), whereby the wafer was scribed using a diamond scribe and cleaved into pieces, exposing the fracture surfaces. Because of the brittle behavior of the silicon and the diamond materials, the fracture process is expected to induce very little damage into the surface topography or sub-surface structure. This technique therefore presents a nearly equipment-free method to produce SEM sections of brittle materials with little time or effort. In Method 3, this same UNCD-coated silicon wafer was subjected to the mechanical-polishing technique (Fig. 7c); this process is also called metallographic sample preparation, and is exceptionally common in materials science and engineering [42]. While not required, the present investigation used the common practice of including an additional (sacrificial)

sample of the same material mounted within the same epoxy resin. This practice prevents the possibility that differences in polishing rate between the mounting resin and the sample could cause rounding of the surface of interest. In this case, an auto-polishing system (MultiPrep 8, Allied, Compton, California, USA) was used to mechanically polish the sample to a sub-micron surface polish. After leveling the sample using grinding, the sample was polished using successively finer grits, progressing along 9, 6, 3, 1, 0.5, and 0.01 µm slurries. Each step was used to remove a material thickness approximately corresponding to three times the grit size of the previous polishing step. After polishing, the sample was sonicated in ethanol for 15 min to remove any residue present from the polishing process prior to imaging. Finally, in Method 4, a sample was created from this same wafer using the process of ion-polishing (Fig. 7d). Here, the material is milled using a beam of Ar ions that approach the cross-section of interest at a grazing-incidence angle. In this work a Fischione Instruments model 1060 ion mill using an argon plasma at 4keV a focus of 50%, a grazing incidence of 7^{o} from the surface, and a lateral rocking angle of 70^{o}. Prior to milling a UNCD-coated silicon coupon was released from the bulk using the simple-fracture method described above, but any cutting or breaking method could have been used to expose the surface. Once exposed, the glancing-angle ions were used to remove material, exposing the fresh surface.

E.2.1.2. Data processing methods: Extracting quantitative topography from side-view SEM images

Once the samples were created, they were imaged in profile using SEM, as shown in Fig. 8a. Images were collected on a field-emission scanning electron microscope (Sigma VP, Zeiss, Oberkochen, Germany). Samples were mounted using double-sided carbon tape to mitigate sample-charging effects. The sample and chamber were then plasma cleaned using an EM Kleen with an RF of 50 W, pressure of 45 mTorr and a run time of 8 mins (stable plasma exposure was approximately 6 mins). This was done to mitigate any carbon deposition on the sample under high acceleration voltages. The samples were then imaged using an aperture setting of 7.5 mm, an acceleration voltage of 15kV and an in-lens secondary electron detector. Once imaged, the profile of the surface was quantified (Fig. 8b). Generally, there is flexibility in how this step is performed. For some samples, edge-finding routines such as those that come standard in programs like ImageJ or MATLAB can be used to find the boundary between the light-colored sample and the dark-colored background. In the present work, a manual point-picking method was used, where a trained user visually selects a sequential line of points that define the boundary. Here, this was implemented through a custom algorithm (MATLAB, MathWorks, Natick, MA) that has been used extensively in prior investigations (for example, Ref. [43]). Similar algorithms exist in ImageJ and other freely-available software. This profile extraction must be performed in calibrated units, using the scale bar of the SEM image. The final result is a series of x,y coordinates (Fig. 8c), not dissimilar from the output of a stylus profiler.

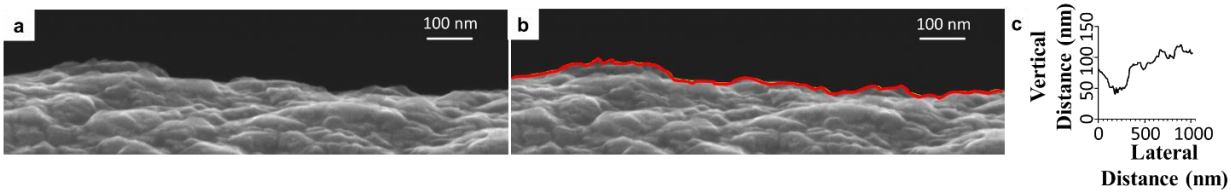

Figure 8: Extraction of a quantitative profile. (a) A side-view SEM image reveals the boundary between the boundary between the light-colored material and the dark-colored vacuum. (b) This boundary is digitized using automatic edge-detection algorithms or manual point-picking, resulting in a quantitative 2D line profile (red line). (c) This line profile can be used and analyzed similar to the output of a stylus profilometer.

Surface topography data was not collected in the present investigation, instead using the data from our prior investigation. However, because this data will become important in the data analysis section, we explicitly specify that this data was collected on a stylus profilometer (DektakXT, Bruker,

Billerica, Massachusetts, USA). One-dimensional line scans were taken at different scanning speeds ranging from 1 µm/s to 100 µm/s. A total of 16 measurements were taken for each flooring surface at 8 different scan lengths, 0.05, 0.15, 0.3, 1.5, 3, 10, 25, 50 mm with two repetitions each. The lateral spacing of data points ranged from 40 nm to 5 µm. These measurements were collected at random orientation and did not show any significant variation with direction. To remove the tilt of the sample and the bowing artifact from the tool, a parabolic correction was applied to all the measurements.

E.2.1.3. Topography-analysis Methods: Computing metrics for (1) a multiscale analysis using the power spectral density (PSD); and (2) scalar analysis: the root-mean-square (RMS) parameters

First, a multiscale analysis of topography was performed using the one-dimensional power spectral density, a widely used (e.g., [44]) multiscale topography metric. The PSD separates the surface topography into contributions from different wavevectors. From a mathematical standpoint, the PSD is the Fourier transform of the autocorrelation function, or equivalently the square of the Fourier transforms of the height itself. Here we compute the PSD C(q) according to the practices described in Ref. [45]:

$$C(q) = L^{-1}\left|\tilde{h}(q)\right|^2 = L^{-1}\left|\int_0^L h(x)e^{-iqx}dx\right|^2 \quad (2)$$

We note that the details of the calculation of the PSD can vary across different software implementations. Here, we use the open-source analysis code from the freely-available web application https://contact.engineering, which is fully documented in Ref. [46]. We note further that a power spectral density can be calculated from 2D (line-scan) or 3D (area-scan) measurements of topography; at all points in this paper, we compute PSD using the line-scan approach to ensure an apples-to-apples comparison across all techniques.

Second, the surface topography was analysis using scalar roughness parameters: the RMS height h_{rms}, RMS slope h'_{rms}, and the RMS curvature h''_{rms}. From a real-space measurement, these quantities can be computed in real-space from the line profiles as: [47]

$$h_{rms}^2 = \frac{1}{L}\int_0^L h^2(x)dx, \qquad h_{rms}'^2 = \frac{1}{L}\int_0^L \left(\frac{dh}{dx}\right)^2 dx, \qquad h_{rms}''^2 = \frac{1}{L}\int_0^L \left(\frac{d^2h}{dx^2}\right)^2 dx \quad (3)$$

However, the value computed from a single measurement will vary strongly with the size scale of that particular measurement (as discussed in Ref. [47]). To avoid this problem, these same parameters can be calculated equivalently, according to Parseval's law, in frequency space. Here, we combine the computed power spectral densities from each measurement (different techniques and different length scales) and then take the averaged PSD as a complete representation of the surface. Then, we integrate over the positive-frequency domain, according to Ref. [47].

$$h_{rms}^2 = \frac{1}{\pi}\int_0^\infty C(q)\,dq, \qquad h_{rms}'^2 = \frac{1}{\pi}\int_0^\infty q^2 C(q)\,dq, \quad h_{rms}''^2 = \frac{1}{\pi}\int_0^\infty q^4 C(q)\,dq \quad (4)$$

The result yields RMS parameters that describe the surface as a whole, rather than any individual measurement.

E.2.1.4. Statistical Methods: Evaluating the statistical significance of differences between surfaces

One of the main goals of this paper is to quantitatively compare measured surface topography across techniques, which requires a method to determine whether two power spectral densities have statistically significantly differences or are (statistically) indistinguishable. To achieve this, we followed and slightly adapted the method established by Chrostowski *et al.* [48, 49]. In particular, a statistical

comparison was performed pairwise between all PSDs, using the four-step approach shown in Fig. 9 and described below.

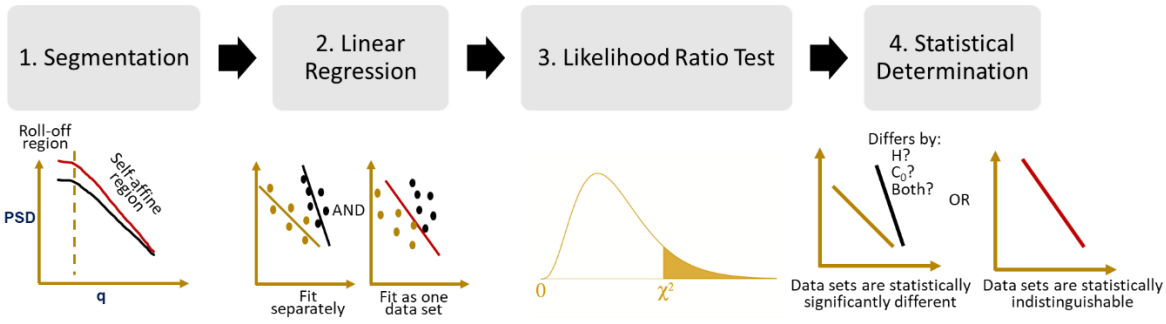

Figure 9: Statistical comparisons of PSDs. This flow-chart demonstrates the statistical comparison of two PSDs. First, if needed, the two PSDs are divided into regions of interest; a typical division for many surfaces is between the 'roll-off region' and 'self-affine region'. In the present data, this segmentation was only used to remove the artifacted portion of the curves. Second, the Wilk's test (main text) is performed for the two curves in the region of interest, determining whether they are distinguishable or indistinguishable. Third, if distinguishable, ordinary-least squares is used to determine whether they differ in slope (i.e. fractal dimension, or Hurst exponent [50]) or in offset (i.e. magnitude of the power spectral density).

First, segmentation. If needed, the two PSDs under comparison are divided into regions of interest, such as the 'roll-off region' or the 'self-affine region'. The reason for this step is that many PSDs (such as the blue line in Fig. 12) contain regions of distinct slopes; therefore, it may not make sense to perform statistical testing on the curve as a whole. In the present analysis, this segmentation was only used to remove the artifacted (q^{-4}) portions of the SEM-measured PSDs; the remainder of the curve was not subdivided further.

Second, regression analysis. In this step, we performed linear regression to the log-log data. While any arbitrarily complex equation can be fitted to the measured data (with or without weighting) [48], linear regression was chosen here for simplicity and ease of use. Assuming a portion of the one-dimensional PSD can be described by a power-law equation $C^{1D}(q) = C_0 q^{-1-2H}$, then the log-log plot can be fit to a line according to: $\ln(C^{1D}) = \ln(C_0) + (-1-2H)\ln(q)$. For each pair of measured power spectral densities, three separate line fits are generated using ordinary least squares regression (which include log transformation for both C(q) and q): one fit using the first PSD, one fit using the second PSD, and one fit to both of the PSDs as a combined data set. Each of the three fits yields best-fit values for C_0 and H, and each one yields a maximum likelihood of those fit values, designated $\max L\left(C_0, H \middle| C^{1D}_{measured}\right)$. The maximum likelihood function is a standard statistical output; its form will vary with the underlying equation that was fit, but it is straightforward to calculate and is automatically output from most statistical software. For simplicity of notation, we designate all fit parameters by θ_i and all measurements of PSDs as Y_i, following the notation of Ref. [48]. For the linear-regression analysis, we further designate the two separate measurements using the subscripts 1 and 2, and the combined data using the subscript $1 \cup 2$.

Third, likelihood-ratio test (also called the Wilk's test). Finally, we compute determine the statistical similarity of the two PSDs using hypothesis testing. While the fit will *always* be better with more fitting parameters, a likelihood-ratio test enables the evaluation of whether the improvement in fit is better than it would be from random chance. This statistical test uses the test statistic the log-likelihood ratio:

$$W_{test} = -2\ln\left[\frac{\max L(\theta_{1\cup 2}|Y_{1\cup 2})}{\max L(\theta_1|Y_1) * \max L(\theta_2|Y_2)}\right] \quad (5)$$

According to Wilk's theorem, if the null hypothesis is correct (i.e., the two PSDs are indistinguishable), then the test statistic should be equal to a chi-squared distribution with the number of degrees of freedom equal to the difference in model parameters. Since the numerator has two fit parameters (as mentioned, θ contains both fit parameters C_0 and H), and the denominator has four fit parameters, then the critical value of the test statistic, for 95% confidence and 2 degrees-of-freedom, is W_{crit}= 5.991.

Fourth, statistical determination. Finally, if $W_{test} > W_{crit}$, then the null hypothesis can be rejected, and the two PSDs are considered statistically significantly different. Otherwise, the null hypothesis cannot be rejected, and two PSDs must be considered indistinguishable. In the former case, the linear regression can be used to determine whether the primary differences are in the slope (i.e. Hurst exponent, fractal dimension) or the intercept (i.e., the vertical offset of the curves). Of course, the individual values for H and C_0 can still be reported if the data sets fail the likelihood-ratio test, but their differences cannot be considered meaningful. See Ref. [48] for an excellent discussion of the number of measurements that should be required to resolve differences of varying sizes.

E.2.2. Results and Discussion

E.2.2.1.Extracting topography, and topography metrics, from SEM images

Representative images from the side-view SEM measurements are shown in Fig. 10. Examples are shown at two different magnifications for all four of the samples. Qualitatively, the samples appear approximately similar, though some differences are apparent. First, for the wedge sample (Fig. 10a), the appearance of the material in the lower half of the image is significantly different from the material in the lower half of the cross-section samples (Fig. 10b-c). This reflects the fact that the cross-section samples reveal the inside of the sample, i.e., the silicon sub-surface material, while the wedge sample looks only at the surface itself, i.e., only the UNCD material. However, this sub-surface material is not being characterized in this investigation. Rather, only the boundary between the light-colored material and black background is being found; therefore, this sub-surface difference will have no effect on results. Furthermore, while there is a difference in thickness of the sample between the various preparations, this effect was extensively studied in Khanal *et al.* [40] and it was determined not to have an effect on the statistical characterization of the surface. For each sample preparation, one image was collected in three locations at six different magnifications.

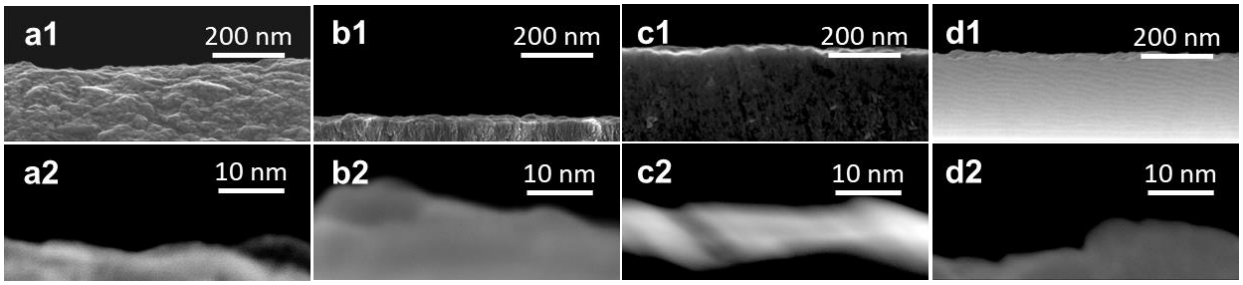

Figure 10: Side-view SEM images of the surface. The various sample preparations (from Fig. 1) were imaged in profile in the SEM to reveal the surface topography. Representative images are shown here, at two different magnifications (50,000x (top) and 1000,000x (bottom)) for each sample: (a) wedge deposition; (b) simple fracture; mechanical polished (c); and ion polished (d). In each image, the lighter-colored region represents the UNCD material and the black region on top represents vacuum. Therefore, the boundary between them represents one line profile of the surface of interest, extracted as shown in Fig. 2. We note that some blurring of the edge is visible in these images due to charging; this is a common corner effect in SEM, and thus its impact on results will be explicitly discussed.

First, the multiscale metric—the power spectral density—was computed (see Methods) from the extracted topography profiles. Figure 11 shows the complete results from the wedge-deposition sample. The PSD was computed from each individual profile and then all PSDs are averaged together for a single multiscale statistical representation of the surface as a whole. There are no adjustable

fitting parameters in the PSD analysis, it is shown that the measurements across scales from nm to mm all align reasonably well. For clarity, the typical slope of common topography artifacts (q^{-4}) is shown in red. Second, the scalar metrics—the RMS height hrms, and RMS slope h'rms—were computed (see Methods) in frequency space from the averaged PSD. The results for the wedge-deposition sample resulted in h_{rms} = 14.8 nm and h'_{rms} = 0.46. The values were calculated only from the reliable region. All quantitative topography measurements used in the present paper are uploaded to a repository and are freely available (see Data Availability statement for details). The following section will evaluate the accuracy of SEM-measured topography across size scales.

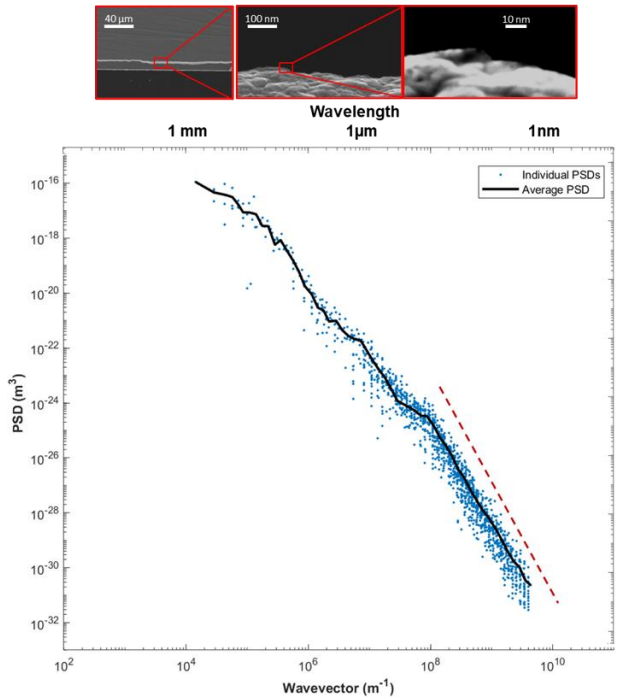

Figure 11: Multiscale analysis of SEM-measured topography using the power spectral density. After the surface was imaged (see Fig. 10), then the topography profiles were extracted (see Fig. 8), and each individual profile was used to compute its PSD (see Methods). Each individual PSD is plotted here (points) for the wedge-deposition sample. Then, all individual PSDs are averaged to create one single average PSD (line) that is a statistical representation of SEM-measured surface topography across all scales. The following section evaluates the reliability of different regions of this measured curve. For clarity, the typical slope of artifacted data (q^{-4}) is shown in red.

E.2.2.2. Evaluating the accuracy of the SEM-measured topography: Comparing against other techniques

The topography measured here using SEM is quantitatively compared against previous topography measurements on the exact same samples: ultrananocrystalline diamond from the wedge-deposition method. In the previous measurements, Gujrati et al. [47] used stylus profilometry, atomic force microscopy, and transmission electron microscopy. First, the SEM-measured topography is evaluated at the small scales, through comparison to the AFM and TEM data. Figure 12 shows the power spectral densities of topography as measured previously using TEM and AFM, as compared to those of the present SEM technique. Note that the prior work includes the removal of the tip-size artifacts for the contact-based techniques [47].

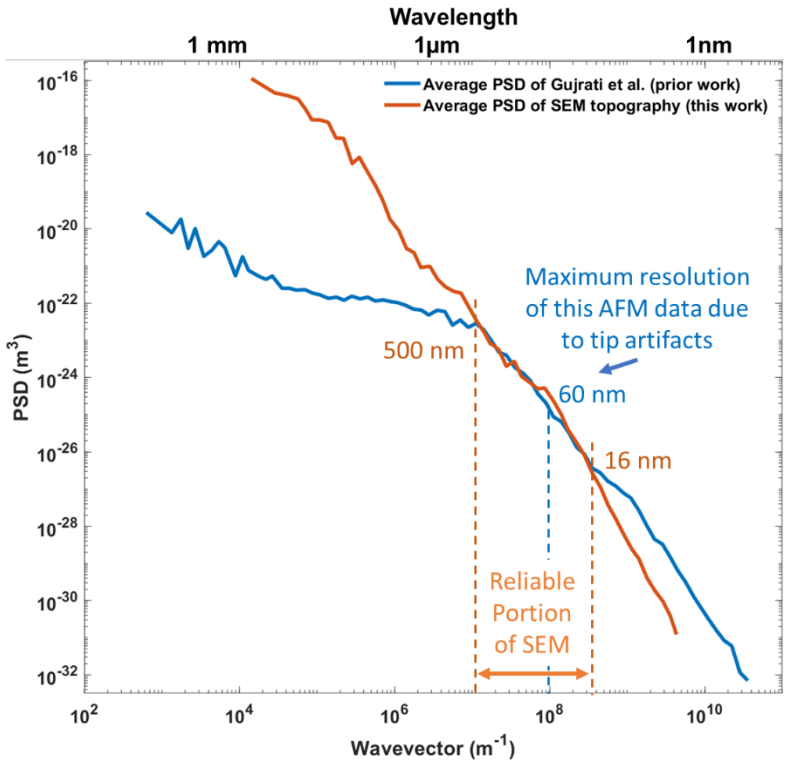

Figure 12: Validating the SEM-measured topography against prior results. (a) The SEM-measured topography from the present work (orange curve) was evaluated by comparison against the previously measured topography [47] based on stylus, AFM, and TEM. The data agrees well over the intermediate wavevectors; however, it deviates from prior measurements at the large and small scales. The sources of deviation are discussed in the main text. The SEM-measured topography is determined to be accurate over a range of 16 nm to 500 nm. In comparison, the established range of AFM from prior work is indicated over a range of 60 nm to 3000 nm.

The SEM-measured topography shows good agreement with the AFM and TEM measurements over the intermediate range of wavevectors (size scales) but appears to deviate at the small-scales. Well-known artifacts [45] often cause the power spectral density to follow q^{-4} behavior at the smallest size scales. However, a typical explanation for this behavior is tip-based artifacts [51] where the scanning tip cannot accurately sample the valleys and instead measures downward kinks or cusps, which results in a signature in the power spectral density. In the present SEM imaging, there is of course no scanning tip, but it is possible that the blurring artifact, which is visible in the higher resolution images in Fig. 10, is causing the same effect. The wedge topography (orange curve) appears to show a sudden deviation to q^{-4}-behavior (Fig. 11) at a wavevector of approximately $3x10^8$ m^{-1}, which corresponds to a length scale of 16 nm. Based on the experimental parameters used in this work, the theoretical resolution (based on Abbe's equation) should be approximately 1.15 nm. However, the present q^{-4} criterion provides an empirical measurement for the initiation of artifacts, and therefore provides an objective measure of the maximum resolution at which the SEM topography can be used. The difference between the theoretical resolution of the SEM and the actual maximum resolution of the topography measurements is likely explained by charging artifacts, which are known to be worse at sharp corners such as a wedge or sectioned surface [52].

The SEM-measured topography showed deviations from the prior stylus-based measurements at the largest wavelengths (small wavevectors). For the ultra-low magnifications (250x and 5000x), below a wavevector of approximately $1x10^7$ m^{-1}, the SEM results show a continuation of their prior upward trend. By contrast, the stylus measurements exhibit the well-known "roll-off" behavior, where the slope abruptly changes to a trend that is closer to horizontal. Here, stylus profilometry is believed to be more accurate and this is commonly observed for surfaces that are nominally flat above a certain size scale. To quantitatively determine the statistical significance of the difference between them, the

likelihood-ratio test was performed (see Methods) between the range of the length scales 1μm to 1 mm (10^3 to 10^6 m^{-1} range of wavevectors). The likelihood ratio test results in the table below showed that the two PSDs in that range were statistically significantly different (95% confidence).

This SEM-measured topography begins to deviate below a wavevector $1x10^7$ m^{-1}; this corresponds to a minimum resolution of accurate SEM topography corresponding to approximately 500 nm. One possible explanation for the deviations from true topography at the largest scales is planarity distortions, as discussed in Ref. [53]; another possible explanation is the 1-to-1 nature of the measurement technique, such that there is a coupling of height resolution to lateral resolution in a way that does not occur in AFM or stylus measurements. In other words, for the SEM, a large lateral measurement size can only be accomplished by also increasing the size of an individual pixel. Overall, this large-scale limitation of the SEM technique must be accounted for; however, many other techniques (e.g. stylus profilometry) exist for measuring topography at size scales larger than 1 μm.

In summary, the SEM-measured topography has been compared against prior results for the same material based on multiple techniques. The power spectral density was used to determine a large-scale and small-scale cutoff where SEM-measured results began deviating from true topography. Using these two empirical cut-offs, the SEM measurement of topography is considered validated over a range of length scales from approximately 500 nm down to approximately 16 nm.

E.2.2.3. Evaluating the consistency of SEM-topography for the four proposed options for sample-preparation method

Here we compare the results from the four different approaches described in the Methods section to understand whether the sample-preparation technique significantly affects the measured results. To investigate this effect, the power spectral density was computed from all four of the different methods: wedge deposition, simple fracture, mechanical polished, and ion polished, as shown in Fig. 13. Qualitatively, the four power spectral densities appear similar, but with random fluctuations, and with an apparent upward deviation of the wedge sample from the remaining samples in the mid-range of size scales. The RMS height and slope for the four different sample preparation techniques are shown in Table 2.

Table 2: RMS height and slope is extracted from the average 1D PSD, using equation 2, for each of the cross-sectional preparation methods for the SEM analysis of UNCD topography**.**

Treatment	h_{rms} **(nm)**	h'_{rms} **(m/m)**
Wedge deposition	14.8±0.4	0.46±0.14
Simple Fracture	14.4±0.2	0.33±0.12
Ion Milled	14.1±0.1	0.37±0.18
Mechanically Polished	14.2±0.3	0.34±0.12

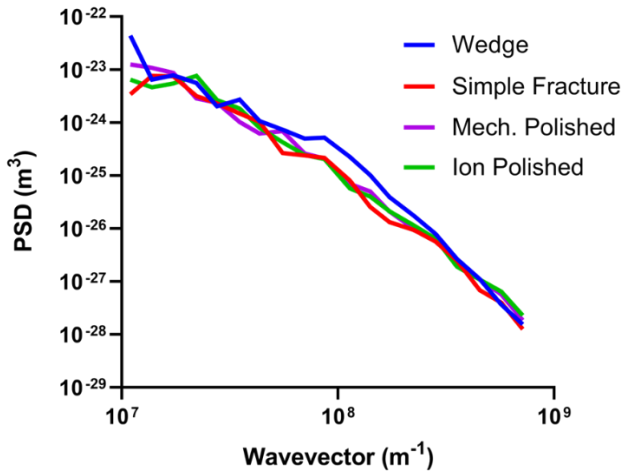

Figure 13: Comparing results across sample-preparation techniques. The averaged power spectral density is computed for the SEM-measured topography of all four sample-preparation methods (legend). Results are only included for the region of wavevectors determined to be reliable (see previous section). The results from the different methods are qualitatively similar; a quantitative analysis is performed below.

Here, the results of the likelihood-ratio test are shown in Table 2. In the segmentation step, the artifacted regions were removed such that comparisons have only been performed over the determined range of SEM accuracy: 16 nm to 500 nm. In the regression-analysis step, ordinary least squares (OLS) was used. Specifically, the self-affine portion of the one-dimensional PSD was described by a power-law equation $C^{1D}(q) = C_0 q^{-1-2H}$, then the log-log plot can be fit to a line according to: $\ln(C^{1D}) = \ln(C_0) + (-1-2H)\ln(q)$.The values of fit parameters C_0 and H for each sample-preparation method are shown in Table 2. Various assumptions of OLS were confirmed for the log-log data, including the assumptions that the independent variable and the residuals of the regression were normally distributed, as well as the assumptions of linearity and homoscedasticity. If the measured data sets had been determined to be statistically significantly different, then post-hoc tests would have been performed to test whether the two surfaces are distinguishable because of different slopes, different offsets, or both. However, these were not evaluated for indistinguishable data sets. The results showed first that the SEM and TEM measurements for the wedge-deposition sample yielded indistinguishable over the non-artifact region (Table 4, top row). This confirms quantitatively the qualitative conclusion that shown in Fig. 11&12. In addition, the subsequent six rows show a pairwise comparison between the results from the four separate sample-preparation methods. The results show that the sample-preparation technique has no discernible effect on the resulting measurement of surface topography.

Table 3: Best-fit parameters C_0 and H for each of the cross-sectional preparation methods for the SEM analysis of UNCD topography.

Treatment	C_0 (m^3)	**H**	$\mathbf{R^2}$
Wedge deposition	10	0.91	0.977
Simple Fracture	6	0.92	0.928
Ion Milled	2	0.80	0.985
Mechanically Polished	4	0.82	0.953

Table 4: The results from the likelihood ratio test comparing the averaged PSDs in the non-artifact region for each pairing of the measured PSDs for UNCD. The likelihood ratio W_{test} is compared against

the critical value W_{crit} required to reject the null hypothesis ($\alpha = 0.05$). To save space, the wedge-deposition sample is abbreviated as just “wedge”.

Comparison (Sample 1: Sample 2)	*Likelihood ratio* W_{test}	*Critical value* W_{crit}	*Statistical determination*
Wedge SEM: Wedge TEM	0.618	5.991	Indistinguishable
Wedge SEM: Simple Fracture SEM	1.376	5.991	Indistinguishable
Wedge SEM: Mech. Polished SEM	1.652	5.991	Indistinguishable
Wedge SEM: Ion Polished SEM	1.527	5.991	Indistinguishable
Simple Fracture SEM: Mech. Polished SEM	0.921	5.991	Indistinguishable
Simple Fracture SEM: Ion Polished SEM	1.185	5.991	Indistinguishable
Ion Polished SEM: Mech. Polished SEM	1.247	5.991	Indistinguishable

E.2.2.4. Achieving multiscale topography characterization by combining topography from SEM and stylus

The conclusion from this analysis is that the sample-preparation method does not have a strong effect on results, and therefore the recommendation is to use whichever method is (a) appropriate for the material and then (b) simplest. For example, the wedge-deposition is the simplest for a material that is deposited onto a substrate, such as measuring the topography of a wear-resistant coating like diamond-like carbon or chromium nitride. The topography in a real-world use-case can be assessed by including some witness samples in the deposition chamber. However, this will not be possible for a bulk sample, or a material that has been modified after deposition, such as a semiconductor substrate that has undergone chemical-mechanical planarization. In that case, since the substrate is brittle, a simple-fracture approach could be used. Finally, in cases of a ductile material, such as measuring the topography of a metal component made with additive-manufacturing, the mechanical-polishing technique will be required. Finally, for the case of a very easily damaged substrate, such soft metals or certain ceramics that do not polish well, the ion-polishing method will be needed. In summary, for a wide variety of materials, SEM-measured topography can be accurately used to capture topography down to approximately 10 nm, with very little additional effort required.

Fig. 14 compares the multiscale topography as collected using two different approaches: first, the previously published multiscale PSD of UNCD [47], which was taken with stylus, AFM, and TEM; and second, a new multiscale PSD that is computed only using the present SEM analysis (only the reliable region of 16 nm to 500 nm) in combination with the stylus measurements. The aforementioned statistical test was applied to the two curves with a segmentation at 1 micron, delineating the self-affine and roll-off regions. The result of the test was that the two PSDs were found to be indistinguishable from one another across the whole reliable region.

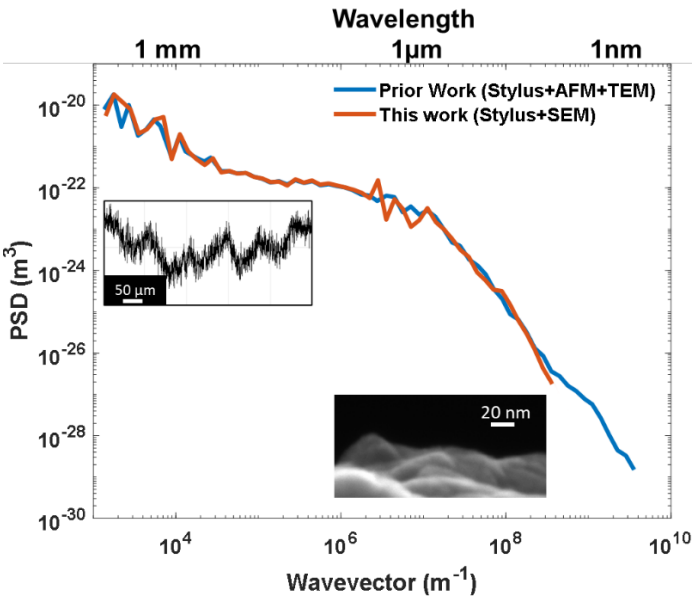

Figure 14: Measuring multiscale topography using only SEM and stylus. Here we compare the previously reported comprehensive topography characterization of UNCD using TEM, AFM, and stylus (blue) against the PSD generated from a combination of only SEM and stylus (orange). The newer SEM-based analysis is far simpler and less time-consuming, while the results are statistically indistinguishable of the range evaluated. The only sacrifice is in high-resolution information below approximately 15 nm; in some conditions of materials system and performance criterion this may matter, but in other conditions this small scale of roughness will not contribute to performance.

There are two critical factors that must be considered during use of the above method (stylus + SEM). First, the SEM-based technique results in a loss of information on the smallest-scale topography, between the range of approximately 4 Å to 16 nm. There are some situations where this loss of measurement resolution could have a significant effect on predicted results (such as the adhesion of soft materials described in Ref. [54]), and other situations where there is a minimum size scale below which the roughness no longer contributes [55]). Thus, care must be taken to understand these effects. Second, as described in the prior investigation [47] the stylus profilometer must be set to report the raw topography, absent any filters that are commonly used in ISO standards (e.g. ISO-21920 [56] or ASME B46.1 [57]). This can be achieved by setting the stylus tool to report the “primary profile” as defined in ISO-21920 [56], (which is also called the “P-profile") rather than the “roughness profile” (R-profile) or the “waviness profile” (W-profile). The above-described method will not apply if some scales of topography are being automatically removed in pre-processing of the data. With these two critical considerations, the above technique appears promising.

There are significant advantages of the stylus + SEM technique. The practical advantages of SEM over TEM are availability of SEMs, ease of use of SEM, and ease of sample preparation. SEM also has some advantages over AFM, including a lack of tip-radius artifacts, as well as the ability to measure overhangs, which become important in metals additive manufacturing (3D printing) and other complex geometries. However, there are distinct disadvantages of this cross-section SEM compared to AFM, including the difficulty of measuring non-conductive samples and the acquisition of 1D (line-scan) topography instead of 2D (area-scan) topography. In summary, the implication of Fig. 14 is that comprehensive topography characterization can be performed with relative ease using only stylus profilometry and side-view SEM imaging.

Overall, this study compared detailed measurements of UNCD using different combinations of techniques. A limitation of this study includes the fact that only a single material was evaluated, such that the findings could fail to generalize to other materials. And with known limitations of SEM, such as with non-conductive materials, it is likely that the findings will not apply universally. Therefore, further investigation is required to fully validate and establish this method. Nevertheless, the findings of this

study are encouraging for establishing the use of cross-sectional SEM in multiscale characterization of multiscale topography.

E.2.3. Conclusions

Because of the well-established need for multiscale characterization of surface topography, the purpose of this paper is to establish a simpler method for characterizing a wide range of multiscale topography. The results of this investigation have three primary conclusions. ***First,*** cross-section (or side-view) scanning electron microscopy was shown to produce equivalent results to transmission electron microscopy over a limited range of scales despite being far simpler to perform than TEM. While SEM could *measure* topography with resolution at or below 1 nm, the results demonstrated artifacts below the scale of 16 nm, which are attributed to charging and edge effects. Therefore this smallest-scale topography should not be trusted. Additionally, SEM also demonstrated flatness artifacts that imposed a maximum size scale of approximately 500 nm, which may be attributed to distortions or the degradation of vertical resolution in large-scale imaging. ***Second,*** four different methods of sample preparation were evaluated and determined to be equivalently accurate within the limits of statistical testing (likelihood-ratio test). These techniques are wedge deposition (for deposited coatings), and three cross-section methods: samples created with simple fracture, and mechanical-polished or ion-polished samples. In general, the best technique to use will vary with the type of material. ***Third,*** it is suggested that a nearly complete multiscale topography can be achieved using *only* stylus profilometry and SEM; two techniques that are commonly available and reasonably quick and straightforward to perform. Care must be taken to limit the range of reliability of the SEM measurements and to turn off all filters in the stylus profilometer. But with these caveats, this may present a straightforward method for characterizing all scales of topography over seven orders of magnitude, ranging from approximately 10 nm to 10 mm.

E.2.4. Data Availability

All of the new data collected for this manuscript has been posted to a public repository called contact.engineering. All raw data, and analysis routines used, can be accessed using the following DOIs:

- SEM-measured topography data for UNCD, created using Method 1: Wedge Deposition:
  - https://contact.engineering/ui/html/surface/?surface=1099
- SEM-measured topography data for UNCD, created using Method 2: Simple Fracture:
  - https://contact.engineering/ui/html/surface/?surface=1634
- SEM-measured topography data for UNCD, created using Method 3: Mechanically Polished:
  - https://contact.engineering/ui/html/surface/?surface=1635
- Sem-measured topography data for UNCD, created using Method 4: Ion Polished:
  - https://contact.engineering/ui/html/surface/?surface=1633

The previously published data for Ref. [47] can be accessed using the following DOI: https://doi.org/10.57703/ce-jdycp.

E.3. Study #3: Validation of a multiscale hysteresis mechanics model in predicting oily shoe-floor friction across surfaces with varying finishes [confidential]

E.3.1. Methods

E.3.1.1.Hysteresis model

The coefficient of friction μ is computed as an integral that takes into account both the wavevector q and the angle the sliding direction and slope direction, ϕ [27],

$$\mu = \frac{1}{2}\int_{q_L}^{q_1} q^3\, C(q)P(q)\left[\int_0^{2\pi} cos\phi \frac{E"(q\bar{v}cos\phi)}{(1-V^2)\sigma_0}\, d\phi\right] dq \qquad \text{Eq. (6)}$$

$$P(q) = \frac{2}{\pi}\int_0^{\infty} \frac{\sin x}{x} exp[-x^2 G(q)]\, dx \quad \text{Eq. (7)}$$

$$G(q) = \frac{1}{8}\int_{q_L}^{q} q^3\, C(q) \left[\int_0^{2\pi} \left|\frac{E(q\bar{v}cos\phi)}{(1-\nu^2)\sigma_0}\right|^2 d\phi\right] dq \quad \text{Eq. (8)}$$

where other variables are defined as follows. The inputs to the model include the power spectral density C(q), the Poisson ratio ν, the sliding velocity $\bar{v}$, and the normal pressure σ_0. While the material modulus is typically specified as E(w), here it is specified as a function of $qvcos\phi$ in this model which is equivalent to $\omega cos\phi$. The inclusion of ϕ allows for 3D topography effects as the material responds differently when moving parallel or perpendicular to a sinusoidal surface. The limits of integration for wavevectors range from q_L to q_1. These correspond to asperities of the largest wavelength (L) to the smallest wavelength (λ_1). $P(q)$ is the ratio of apparent area of contact, $A(\lambda)$, to nominal area of contact, $A(L)$. The apparent area of contact at any given size scale comprises the real area of contact with surface asperities of a certain wavelength, while ignoring all smaller wavelength asperities. The nominal area of contact is the macroscopic area of contact ignoring any asperities that may not be in contact. The inclusion of $P(q)$ allows for the COF prediction to account for the fact that the fractional area of contact will vary depending on the size scale that is being considered. The term P(q) is calculated as a function of a coefficient $G(q)$ integrated across the position in the direction of sliding, x. The term $G(q)$ serves mainly to incorporate variables such as roughness, material properties, speed, and pressure into the area-of-contact calculations.

To predict the COF of a given shoe and floor contact, the term $G(q)$ is calculated at each wavevector using the limits of integration from q_L to the current wavevector, q, determined by the limits of integration from the original μ equation (Eq. 6). This resulting value is then used to calculate $P(q)$. Finally, the actual COF prediction value can be determined by integrating the resulting $P(q)$, PSD, and loss modulus across the full range of wavevector values. [27].

E.3.1.1.1.Verification

Numerical integration techniques were used to solve the model. A trapezoidal integration was used to calculate each integral in the equations for $G(q)$ and μ, Eq. (9).

$$\int_{x_0}^{x_n} f(x)\, dx = \sum_{i=1}^{n-1} \frac{1}{2} * [f(x_{i+1}) + f(x_i)] * [x_{i+1} - x_i] \quad \text{Eq. (9)}$$

The number of points used, n (inversely related to the point density), used for each trapezoidal integration were found using a point-density analysis. Inspired by a mesh-density analysis used in finite element analysis [58], the resulting COF calculations (using inputs discussed in section 2.4) from the model were plotted against the number of points used between the limits of integration. The number of points was proportional to the time to run the code; thus, the optimal point density balanced the accuracy and solution time. This optimal density corresponded to the point at which the percent difference between that COF calculation and the COF of the previous point on the curve was less than 1%. A varying number of points ranging from 10 to 10,000 for q was used to calculate the COF of one shoe and floor combination (Shoe A and Floor 1). Only one shoe-floor combination was used because it was assumed that the point densities would have the same effects on COF calculations between all shoes and floors. This analysis was performed for both trapezoidal integration variables, q and ϕ, although the range of number of points for ϕ was 40 to 100 because the smaller magnitudes of the limits of integration. The optimal densities were found to be 150 points for the q variable and 50 points for the ϕ variable.

The use of the model in this work was verified [59] against simulation results presented by Persson et al. [27]. We replicated the inputs from Persson et al. and compared plots of our simulation results to the published results [27]. The model was considered verified and used in this study after this consistency with prior research was confirmed.

E.3.1.2.Experimental validation

The model was validated by comparing the model COF predictions to experimentally measured COF values. For this process, 3 shoes and 10 floors were used. The shoes (SRMax Atlanta Men's Soft

Toe SRM 3700, Shoe A, Hardness: 52; the DS Work Service 6671, Shoe B, Hardness: 59; Rockport K71224, Shoe C, Hardness: 53) had different outsole materials as well as tread patterns. The floors (Floors 1-10) had varying surface finishes and roughness levels. Each shoe and floor combination was analyzed constituting a total of 30 combinations. The same parameters were used for all model calculations in accordance with experimental testing conditions used within this study and verified values from other literature.

The model parameters $\bar{v}$ and σ_0 were set at 0.5 m/s and 1 MPa respectively, determined by the values used with the slip tester and typical contact pressures relevant to shoe-floor contact [60, 61]. A Poisson's ratio (ν) of 0.499 was used for all calculations, indicating that the material is nearly incompressible [62, 63]. To ensure roughness and material response data was consistent across shoes and flooring, the same limits of integration were used for all shoe and floor simulations. These values were determined by finding the range of wavevectors for each PSD and complex modulus then selecting limits that were available for all shoe-floor combinations. These limits of integration (q_L to q_1) were $6.28*10^2$ m^{-1} and $2.17*10^8$ m^{-1} corresponding to wavelengths of $1.00*10^{-2}$ m (i.e., 1 cm) and $2.9*10^{-8}$ m respectively (i.e., 29 nm), a range where these techniques are valid [64].

E.3.1.2.1.Experimental COF data collection

The experimental COF data was collected using the STEPS slip tester (Figure 15) (XRDS Systems, LLC, Andover, Massachusetts, USA) for each shoe-floor combination. Friction tests used a sliding velocity of 0.5 m/s and an applied normal force of 250 N. A digital angle measurement tool (General Tools, 822 Digital Angle Finder, New York City, New York) was used to ensure the angle between the shoe and floor was 17° +/- 2°. The normal force, shoe-floor angle, and sliding velocity were selected to be relevant to human slipping while walking [60, 61]. The COF was the average ratio of shear force to normal force, measured over the 50 ms of sliding after the normal force level was reached [8]. For each trial of COF data collection, canola oil was applied to the floor as a contaminant. This contaminant was selected for its relevance as a real-world contaminant (especially in the restaurant industry) and that it is expected to isolate hysteresis friction [34, 65-67]. The oil was poured over the contacting region between the shoe and floor until the thickness of the oil in that region did not appear to visually increase with additional fluid. The first three trials that met all force, angle, and velocity requirements were reported. This was repeated on three separate days consisting of nine total COF measurements for each shoe-floor combination. The mean and standard deviation of these measurements were calculated and used for statistical analyses.

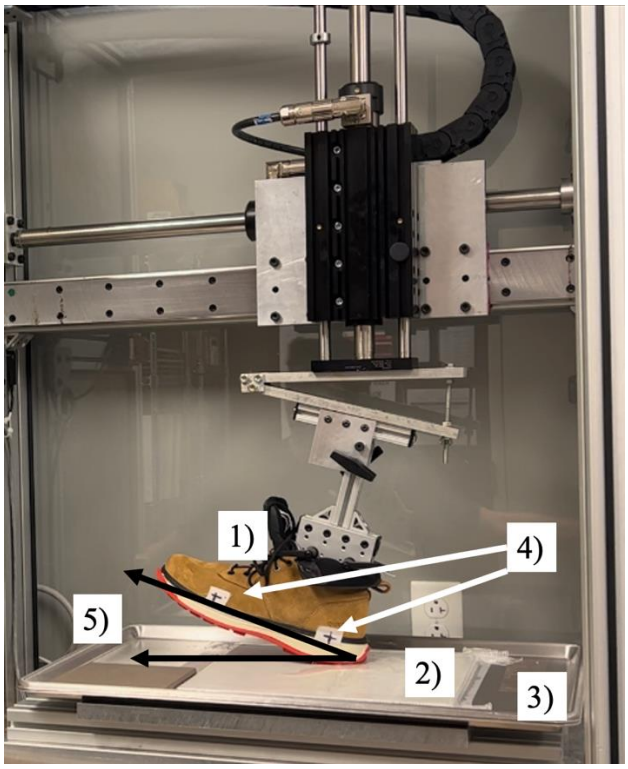

Figure 15: The STEPS slip tester used for experimental data collection of shoe-floor COF with the following components: 1) Shoe, 2) Floor tile, 3) Metal tray for floor attachment, 4) Guiding points to measure angle along shoe, and 5) Lines denoting shoe-floor angle.

E.3.1.2.2.Surface PSD data collection

Surface roughness data was collected for each floor tile using stylus profilometry and SEM. A contact profilometer (DektakXT, Bruker, Billerica, Massachusetts, USA) was used at three different locations and orientations. Profiles were measured using a 4 mm scan length and point space of 0.5 μm. For each floor surface, six line-profile measurements were taken. Next, the surfaces were prepared for SEM measurements by cutting them into 1.5 x 1.5 x 0.5 cm^3 samples. These samples were mounted and then polished so the cross-sections could be examined. A scanning electron microscope (Sigma 500VP, Zeiss, Oberkochen, Germany) was used to collect ten images in a working distance of less than 1 mm at magnifications of x5000, x50,000, and x100,000 [68]. A PSD for each topography measurement was generated by performing a Fourier transform of the autocorrelation of the height varying with position along the surface. The PSD was calculated following the conventions described in Ref. [45] and all PSD calculations were performed using the CONTACT.ENGINEERING platform [46]. The overall PSD of the surface was found as the average of all PSD curves from the various topography measurements [47, 68]. The surface topography used in the Persson model is a 2-dimensional (2D) measurement, however the surfaces in this study were characterized as 1-dimensional (1D) line scans. Therefore, the 2D PSD was estimated using the 1D data under the assumption that the surface topography was isometric (Equation 10). In this equation, C^{iso} is the 2D PSD measurement, C^{1D} is the 1D measurement, q_x is the current wavevector, and q_s is the maximum wavevector [45]. This process was repeated for all floors, generating one PSD for each surface (Figure 16).

$$C^{iso}(q_x) \approx C^{1D}\frac{\pi}{q_x}\left(1-\left(\frac{q_x}{q_s}\right)^2\right)^{-1/2} \quad \text{Eq. (10)}$$

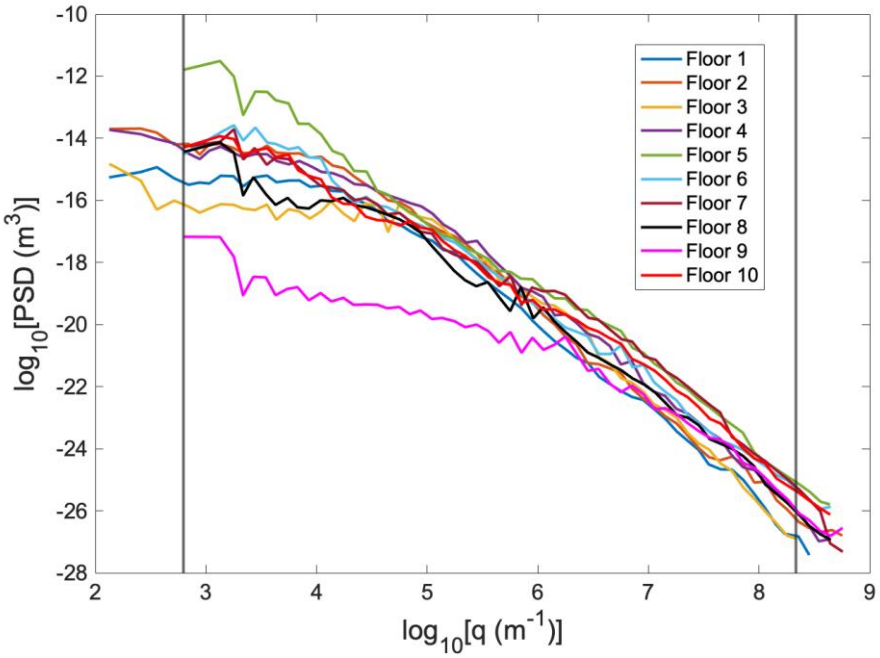

Figure 16: The resulting 1D PSD curves for all floors using stylus profilometry and SEM with vertical lines showing the wavevector limits of integration used as the full range of size scales for all COF calculations.

E.3.1.2.3.Measurements of the dynamic mechanical properties of the shoe material

The complex (storage and loss) moduli were measured for each shoe using dynamic mechanical analysis. All testing for this dataset was performed at a commercial testing facility (C-Therm, Fredericton, New Brunswick, Canada). For each shoe, the outsole was separated, and two 10-mm-diameter disc-shaped samples were taken. After being cut and sanded down to a thickness of 2-3 mm, the samples were glued between metal lugs to be loaded into the testing machine (DMA+150, Metravib, Limonest, France). The temperatures ranged from -50°C to 40°C, increasing at a rate of 2°C/min. At each temperature, the sample was sheared using a displacement of 1 μm (2 μm for Shoe C) over a frequency range of 1-200 Hz. The loss and storage moduli were measured at each incrementing temperature over the frequency range. The complex modulus was found as the combination of these two moduli. The master curve, accounting for moduli measurements at all desired frequencies, was generated using time-temperature superposition at a reference temperature of 20°C leading to frequency response with orders of magnitude ranging from 10^{-2} Hz to 10^{8} Hz (Figure 17).

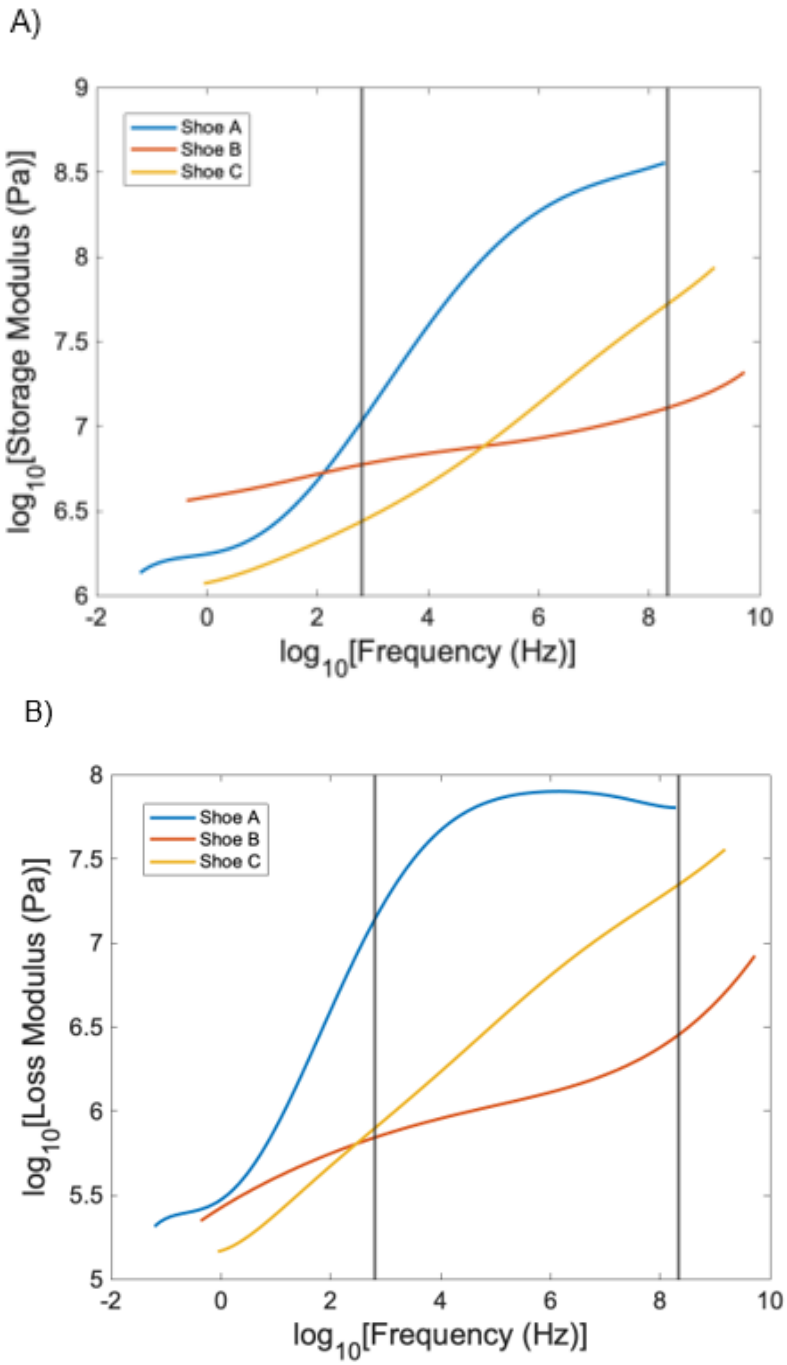

Figure 17: The A) storage, and B) loss moduli for the outsole materials from all shoes versus frequency. Vertical lines show the wavevector limits of integration that were used for COF model calculations (Eq. 2).

E.3.1.2.4.Statistical analyses

Accuracy of the model predictions were assessed with a bivariate correlation analysis. The independent variable was the model predictions, and the dependent variable was the experimental values of COF as measured by the slip tester. The determination coefficient, R^2, was calculated along with the p value ($\alpha = 0.05$) and RMS_{error}. The first correlation analysis used predictions based on the full range of measured topography, from 10 nm to 1 cm (See vertical lines on Figure 17). After this initial bivariate correlation analysis, further examination was performed to determine if better correlation could be found using only a limited range of topography. Model COF results were calculated again using varying upper cutoffs (q_1) between the original limit of integration (10^x m^{-1}) and 10^3 m^{-1}. R^2 was

calculated between each new set of predictions and the experimental results. This process was repeated for lower cutoffs (q_L) between the original limit of integration (10^y m^{-1}) and 10^6 m^{-1}. These analyses were performed to test whether disregarding small or large length-scale features improved model predictions. The COF results corresponding to the cutoff yielding the highest R^2 were used to demonstrate improved COF predictions associated with ignoring certain scales of topography.

E.3.2. Results

E.3.2.1. A raw implementation of the mechanics model: COF predictions using all available scales of topography

The experimentally measured values of COF ranged across an order of magnitude, from 0.052 to 0.54, with a mean of 0.179 and large variability (standard deviation of 0.132). The corresponding predictions of the model, as specified by Eq. 6-8, were significantly higher with a range from 0.272 to 5.524, a mean of 2.050, and a standard deviation of 1.470. While the absolute values were significantly different, an initial bivariate correlation analysis showed a weak yet significant correlation between the experimental and predicted COF values (Figure 18, $R^2 = 0.168$, p = 0.024, RMS_{error} = 0.122).

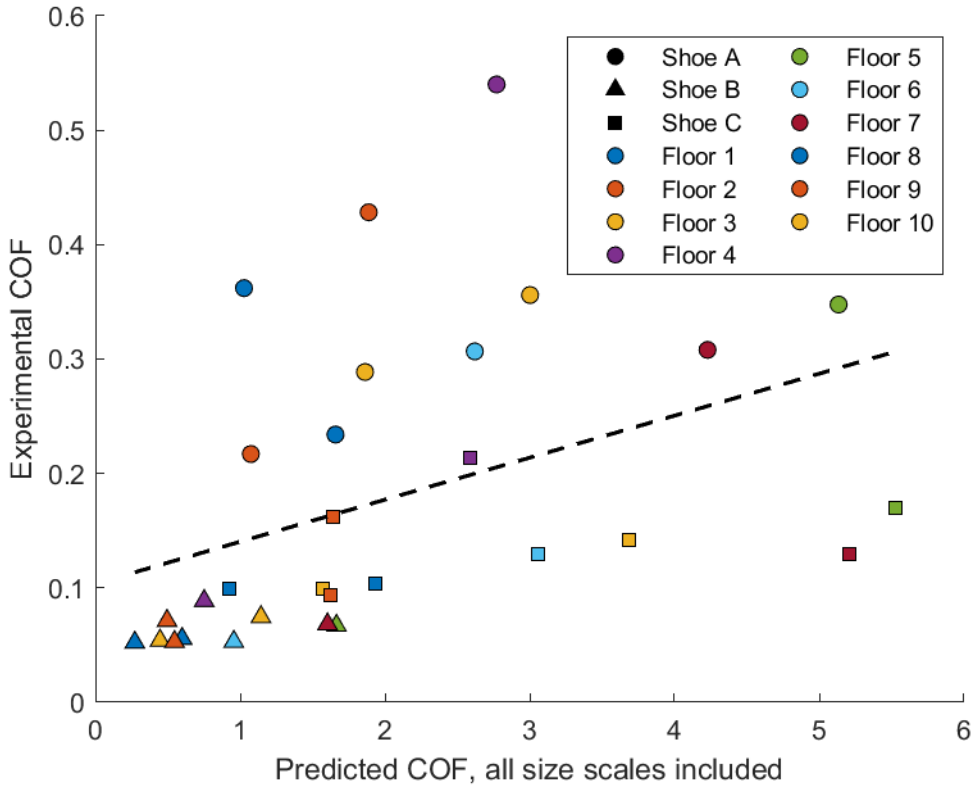

Figure 18: Using the measured topography across all size scales, the multiscale mechanics model significantly overpredicted the true values of oily-conditions COF. The model prediction with measured results across all measurements has an RMS error (RMSE) of 0.122. However, bivariate correlation between model predictions and experimentally measured results shows a weak, positive correlation. The dotted line shows the regression line for this analysis. Different shoes are denoted by marker shapes whereas different floors are denoted by color.

E.3.2.2.A scale-dependent implementation of the mechanics model: COF predictions when a size cutoff is imposed

Because the full-scale implementation of the model showed significant overprediction of COF, then the model was re-implemented under the assumption that only a limited range of size scales of topography contributed to frictional losses. This limited-bandwidth implementation was inspired by prior experimental work indicating that certain size scales contribute more to performance than others [55],

while the exact range of scales that matter will vary depending on conditions. In the full-scale implementation (prior section), these values were defined by the largest and smallest sizes that could be reliably measured. During the limited-bandwidth implementation (this section), COF values were calculated using only a limited range wavevectors (q_{min} to q_{max}), which correspond to a limited range of relevant size scales (λ_{max} to λ_{min}). These outer values were allowed to vary, since it was not clear *a priori* which ranges of scales would be expected to contribute the most. The limited-bandwidth implementation was carried out twice: first with a large-scale cutoff, where q_{max} was kept constant (set by the smallest scale of measurement) and q_{min} was varied across the whole range; and second with a small-scale cutoff, where q_{min} was kept constant (set by the largest scale of measurement) and q_{max} was varied across the whole range. For each value of cutoff during both runs, the R^2 was calculated between experiments and simulations, with results shown in Fig. 19.

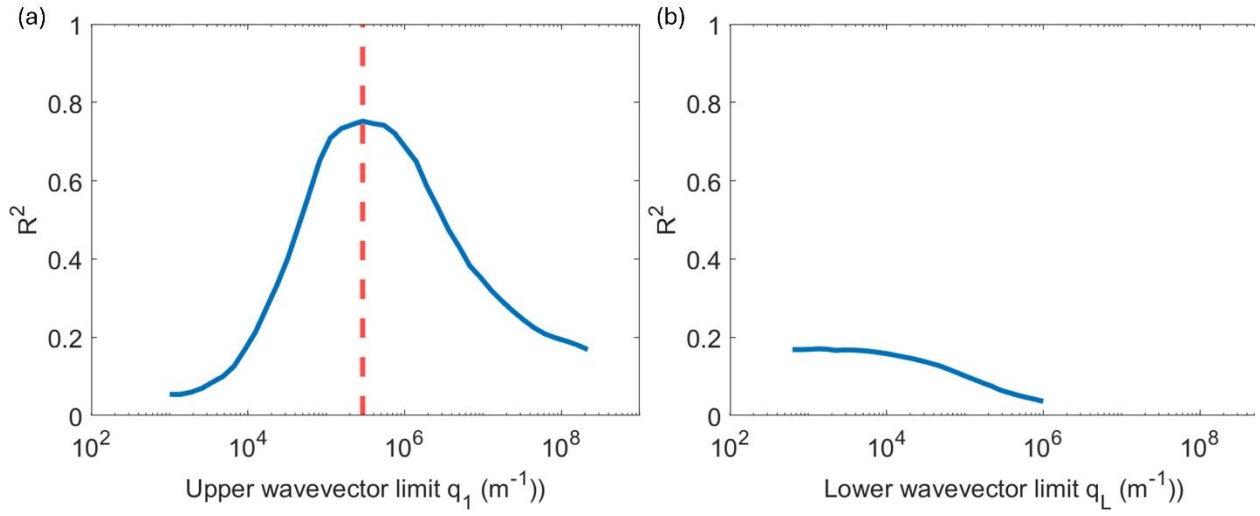

Figure 19: (a)The coefficient of determination is plotted for all cutoff values in the limited-bandwidth implementation of the mechanics model. When a small-scale cutoff is imposed, then q_1 is altered (x-axis). The vertical line shows the R^2 value is maximized, when a small-scale cutoff is imposed at $q_{1(max)}$ = 2.91*10^5 m^{-1}, corresponding to a minimum relevant size scale of about 2 microns. (b) The coefficient of determination plotted against the lower q limit of integration (q_L) used to calculate the corresponding set of COF predictions. Since no significant correlation was found at any lower-wavelength cutoff, then the optimal value is not indicated (as it is in panel (a)).

When modifying the large-scale cutoff, R^2 values were below 0.17 (Fig. 19 (b)) and therefore were considered to be a poor fit to the data regardless of the chosen value of q_{min}. Modifying the small-scale cutoff was far more promising (Fig. 19 (a)). The greatest R^2 value corresponded to an upper q limit of integration of 2.91*10^5 m^{-1}; however, there was a range of cutoff values from approximately 1*10^5 m^{-1} to 1*10^6 m^{-1} where the R^2 was greater than 0.6. The optimal upper wavevector cutoff corresponded to an asperity wavelength of 21.6 μm, with wavevectors greater than the cutoff corresponding to smaller wavelengths. The model calculations with this upper q cutoff of 2.91*10^5 m^{-1} had a mean and standard deviation of 0.415 and 0.401 respectively with a range from 0.001 to 1.555. The absolute values of the predictions were still approximately twice as large as experimental values; however, the bivariate correlation analysis using these COF predictions (Figure 20) corresponded to an R^2 value of 0.752 with $p < .0001$ and an RMS_{error} of 0.066. In summary, the exclusion of small-scale features from the model did improve the correlation between model results and experimentally measured COF, but the exclusion of large-scale features did not improve the correlation.

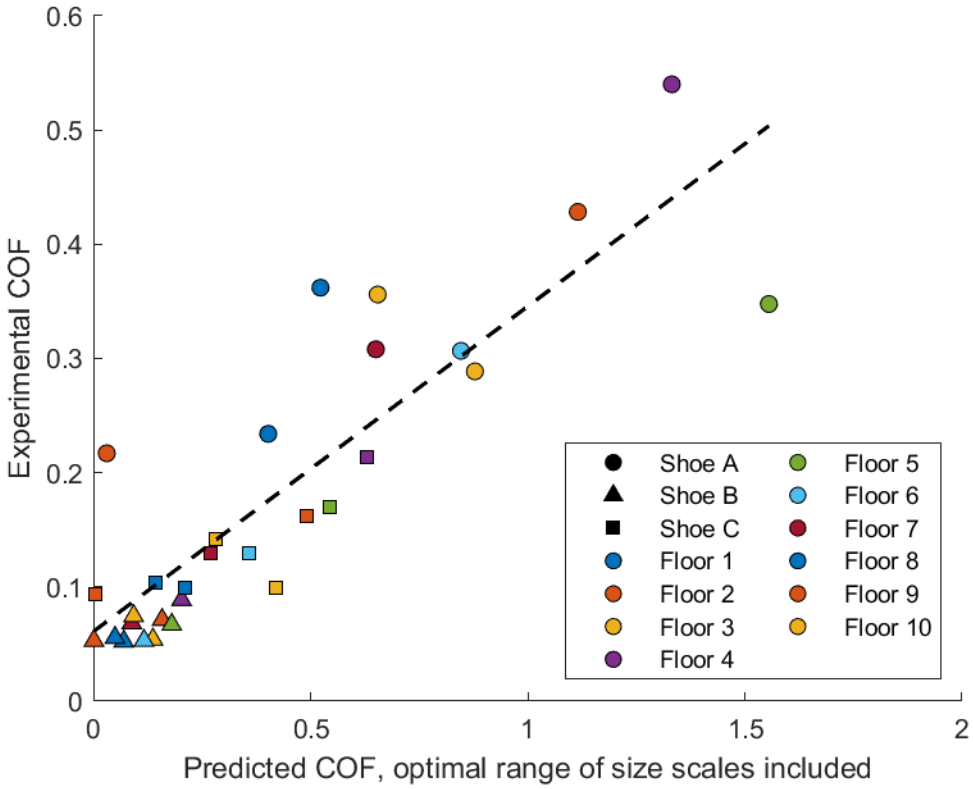

Figure 20: Bivariate correlation between the COF model predictions and the experimentally measured results with an upper q limit of integration of 2.91*10^5 m^{-1} used in the model. The dotted line shows the trendline for the analysis. Different shoes are denoted by marker shapes whereas different floors are denoted by color.

E.3.3. Discussion

The model using the full range of size scales was somewhat predictive of friction (p = 0.024, $RMS_{error} = 0.122$) but predictions improved significantly when excluding small-scale topography beyond a wavevector of 2.91*10^5 m^{-1} ($p < .0001$, $RMS_{error} = 0.066$), corresponding to a size of 21.6 microns. The predictive performance of the model got worse when excluding large-scale topography features. In both the full-scale model and the model with the optimal cutoff, the predicted COF values were higher than those observed experimentally. However, the model predictions were within an order of magnitude of the experimentally measured values when excluding the small-scale features.

The improvement of the model when removing the small-scale features may provide insights into the lubrication mechanism and how it affects the contribution of different topography scales. The model did not consider hydrodynamic effects of the fluid and instead only assumes that the fluid eliminates adhesion friction. Although prior research has indicated that fluid pressures (measured with fluid pressure sensors) are only present when worn shoes or large tread features are combined with high-viscosity fluids, predictions of film thickness indicate that small film thicknesses can form for all shoes [69, 70]. These small film thicknesses may influence small-scale contact but without being measured by fluid pressure sensors (with inlets of ~1 mm) and may not impact the contact of large-scale features [69, 71, 72]. These potential outcomes are consistent with prior researchers who have argued that contaminants effectively reduce roughness of smaller-size-scale asperities (i.e., like a low-wavevector-pass filter) while larger asperities remained unaffected [27, 73]. Another potential mechanism for why small-scale features may not have contributed to friction is the potential for fluid contaminants to become trapped in wells within the apparent contact region and then sealed in by the surface asperities [27, 73]. There may be a scale dependence of the formation of these sealed regions that differently affects topography at different scales. For example, sealed regions of fluid are unlikely to influence floor asperities if the size of the sealed region is smaller than the scale of an asperity.

The model tested in this study offers similar predictive ability to other shoe-floor friction models but, unlike statistical models based on roughness parameters, is far more likely to provide validity across different circumstances. Prior research from our group developed a multiscale finite element model [74] and statistical model [34, 75] (based on tread surface area, hardness, and heel shape) that led to an RMS error of 0.11 (not reported in the study but calculated based on the data) and 0.05, respectively. These two models were primarily focused on geometric features of footwear and each only included 2 flooring samples. The RMS error observed for the present study with small-scale features excluded was 0.07, which was in line with these prior studies. Furthermore, the present model is designed to capture the effects of shoe material properties and multiscale floor topography. The present study demonstrated a good ability to differentiate across three shoe materials and across a larger sample of flooring. Another advantage of the present model over the finite element models is that it is computationally more efficient and does not require the same level of expertise as finite element modeling. While coding the model reported by Persson requires expertise in numerical integration techniques, the implementation of this model (once the code has been developed) does not require specialized expertise. Finite element modeling, on the other hand, requires extensive expertise to implement, including meshing, boundary conditions, material selection, and contact formulation. Thus, the present model (when excluding small-scale features) offers similar predictive ability but requires less expertise than finite element modeling and may be better positioned to capture material and floor topography effects on friction.

This study informs three potential use cases for the utilized viscoelastic hysteresis model. First, it may be useful in predicting the impact of shoe material on shoe friction performance in oily or other slippery conditions where hysteresis friction dominates. In particular, the model may be effective at screening a library of materials with known DMA results against a range of flooring. This opportunity is especially interesting as the library of floor topography characterization grows (for example, through the CONTACT.ENGINEERING web application and FAIR data repository [46]). Alternatively, the model may be useful in determining how changes to flooring (e.g., through roughening a particular scale) would influence friction. A library of DMA data is emerging for different shoe materials including in the current study as well as other recent studies [76]. Lastly, it may eventually be possible for safety professionals to apply the model to select combinations of footwear and flooring that optimize friction performance in slippery environments. Such a process would require broad access to the model, widely available spectral properties of flooring, and material data of footwear.

There were limitations with this study, both in experimental setup and characterizing the model. Shoe geometries, specifically outsole tread patterns, impact friction yet these effects were not included in the model [77, 78]. Furthermore, variation in material moduli measurements across frequencies was not included as only one set of tests was performed for each material. This means that errors in COF predictions from variable shoe material measurements could not be included, and only variation in calculations from the topography input could be accounted for in our estimates of uncertainty. The model best predicted oily friction when small-scale features were excluded. This effect was explained by potential hydrodynamic or sealing effects yet future experimental analyses would be needed to confirm the mechanism behind this finding. Finally, extending this study to a wider range of footwear is needed to get a more robust estimate of the model's validity across footwear.

In conclusion, this study showed that the viscoelastic hysteresis model presented by Persson [27] was able to significantly predict oily shoe-floor friction when small-scale floor surface asperities were excluded. The contaminant may have "filtered" these scales either due to hydrodynamic effects or fluid sealing effects. Compared to finite element analysis or statistical models currently used to predict shoe-floor friction, this model has similar accuracy but is expected to better capture shoe material and floor topography effects and can be performed faster and with less expertise than finite element analysis. Footwear, flooring, and safety professionals may benefit from using this model to create safer products and workplaces.

E.4. Study #4: Validation of a multiscale hysteresis mechanics model to predict oily shoe-floor friction while isolating the effect of varying shoe materials [confidential]

E.4.1. Methods

E.4.1.1.Hysteresis model

The model calculates the COF between a shoe and floor using three equations (Equations 11, 12, and 13). The inputs for these equations are the PSD data from the floor surface, $C(q)$, and the time-dependent material responses including the complex modulus, $E()$, and the loss modulus, $E"()$. The overall equation for the COF, μ, (Equation 11) integrates the various model inputs across wavevector, q, and surface orientation, ϕ. The range of wavevectors used for integration are determined by the available size scales from data collection of both the surface PSD and shoe material moduli. The lower wavevector limit of integration, q_L, corresponds to the largest size-scale asperities with wavelength L. The upper wavevector limit of integration, q_1, corresponds to the smallest size-scale asperities of wavelength λ_1. Model parameters, determined by accepted values within literature or experimental testing settings, include Poisson's ratio, ν, normal pressure, σ_0, and sliding velocity, v. The next equation used in the COF calculation is $P(q)$ (Equation 12). Using many of the same inputs, this equation is integrated across position along the floor surface in the direction of sliding, x. $P(q)$ is the ratio of apparent to nominal area of contact and thus allows for the effect of area of contact on COF to be included in the model. The apparent area of contact is the real area of contact of asperities at a certain size-scale wavelength while ignoring area of contact effects of all smaller size-scale wavelengths. The nominal area of contact is the macroscopic area of contact, ignoring the effects any asperities that are not in contact. This equation is also a function of $G(q)$ (Equation 13). Similar to the COF equation, the $G(q)$ equation is an integral across wavevector and surface orientation, allowing model inputs and parameters to be included in the area of contact term calculation [27].

$$\mu = \frac{1}{2}\int_{q_L}^{q_1} q^3\, C(q)P(q)\left[\int_0^{2\pi} cos\phi\, \frac{E"(qvcos\phi)}{(1-\nu^2)\sigma_0}\, d\phi\right] dq \qquad \text{Eq. (11)}$$

$$P(q) = \frac{2}{\pi}\int_0^{\infty} \frac{\sin x}{x}\, exp[-x^2 G(q)]\, dx \qquad \text{Eq. (12)}$$

$$G(q) = \frac{1}{8}\int_{q_L}^{q} q^3\, C(q)\left[\int_0^{2\pi} \left|\frac{E(qvcos\phi)}{(1-\nu^2)\sigma_0}\right|^2 d\phi\right] dq \qquad \text{Eq. (13)}$$

E.4.1.2.Experimental validation

In order to validate the model, 10 floors and 8 shoes were used. The floors (Floors 1-10) had varying surface finishes and roughness levels. The shoes (Shoes A-H) had the same tread patterns but different outsole materials. The COF for each shoe-floor combination (80 combinations) were measured experimentally then compared to model calculations using measured inputs from each shoe and floor along with various model parameters. A normal pressure of 1 MPa and a sliding velocity of 0.5 m/s were used for experimental testing and model calculations as accepted values found within literature [60, 61]. The final model parameter, Poisson's ratio, was set to 0.499; a value commonly used for shoe rubber meaning that the material is nearly incompressible [62, 63]. The wavevector limits of integration (q_L to q_1) spanned from $6.28*10^2$ m^{-1} to $2.17*10^8$ m^{-1}, a range where use of the various techniques are valid [64]. These limits were set by the available range of size scales for input data of both shoe material moduli and surface PSD's. Finally, as trapezoidal integration was used (Equation 14), the number of points used, n, within the wavevector and surface orientation integrals were 150 points and 50 points respectively.

$$\int_{x_0}^{x_n} f(x)\, dx = \sum_{i=1}^{n-1} \frac{1}{2} * [f(x_{i+1}) + f(x_i)] * [x_{i+1} - x_i] \qquad \text{Eq. (14)}$$

E.4.1.2.1.Experimental COF data collection

The STEPS slip tester (Figure 21) (XRDS Systems, LLC, Andover, Massachusetts, USA) was used for experimental data collection with each shoe and floor combination. The slip tester calculated COF by dividing the average shear force by normal force over the first 50 ms of contact after the desired normal force was applied [8]. A sliding velocity of 0.5 m/s and a normal force of 250 N were used for testing. The shoe-floor angle used was 17° +/- 2°, confirmed before each test with a digital angle measurement tool (General Tools, 822 Digital Angle Finder, New York City, New York). These parameters were determined using values found within literature regarding human walking without slipping [60, 61]. All experimental testing used canola oil as a contaminant due to its prevalence within real-world workplaces and its ability to isolate hysteresis friction by interfering with adhesion [34, 65-67]. This contaminant was reapplied between each trial until the thickness of the oil on the floor did not appear to increase. On three separate days, three trials with the necessary angle, force, and velocity values were collected and reported. Of these nine trials, the mean and standard deviations were calculated and used for statistical analyses. This process was repeated for each shoe-floor combination.

A)

B)

Figure 21: The A) STEPS slip tester used to collect experimental COF data between each shoe and floor and B) three of the eight shoes used showing the identical tread patterns.

E.4.1.2.2.Surface PSD data collection

The roughness data for each floor was collected using stylus profilometry and SEM. First, a contact profilometer (DektakXT, Bruker, Billerica, Massachusetts, USA) was used to measure larger roughness size scales. Three profiles were measured using the profilometer with a scan length of 4 mm and point space of 0.5 μm at different positions and orientations along the surface. Next, 1.5 x 1.5 x 0.5 cm^3 samples of each floor surface were collected and measured using a scanning electron microscope (Sigma 500VP, Zeiss, Oberkochen, Germany). For each sample, ten images were collected in a working distance of less than 4 mm at magnifications of x250, x5000, and x100,000 [68]. A PSD was generated for each surface measurement using a Fourier transform of the autocorrelation of height versus position along the surface. The PSD data from each measurement was averaged to obtain one PSD curve [47, 68]. This process was repeated for each floor yielding one PSD curve for each surface (Figure 22). The roughness information obtained with these methods was in 1 dimension (1D), however the model used a PSD in 2 dimensions (2D). The 2D PSD for each was found using the assumption that the surface topography was isometric (Equation 15), where C^{iso} is the 2D PSD, C^{1D} is the 1D PSD, q_x is a given wavevector, and q_s is the maximum wavevector [45].

$$C^{iso}(q_x) \approx C^{1D}\frac{\pi}{q_x}\left(1-\left(\frac{q_x}{q_s}\right)^2\right)^{-1/2} \qquad \text{Eq. (15)}$$

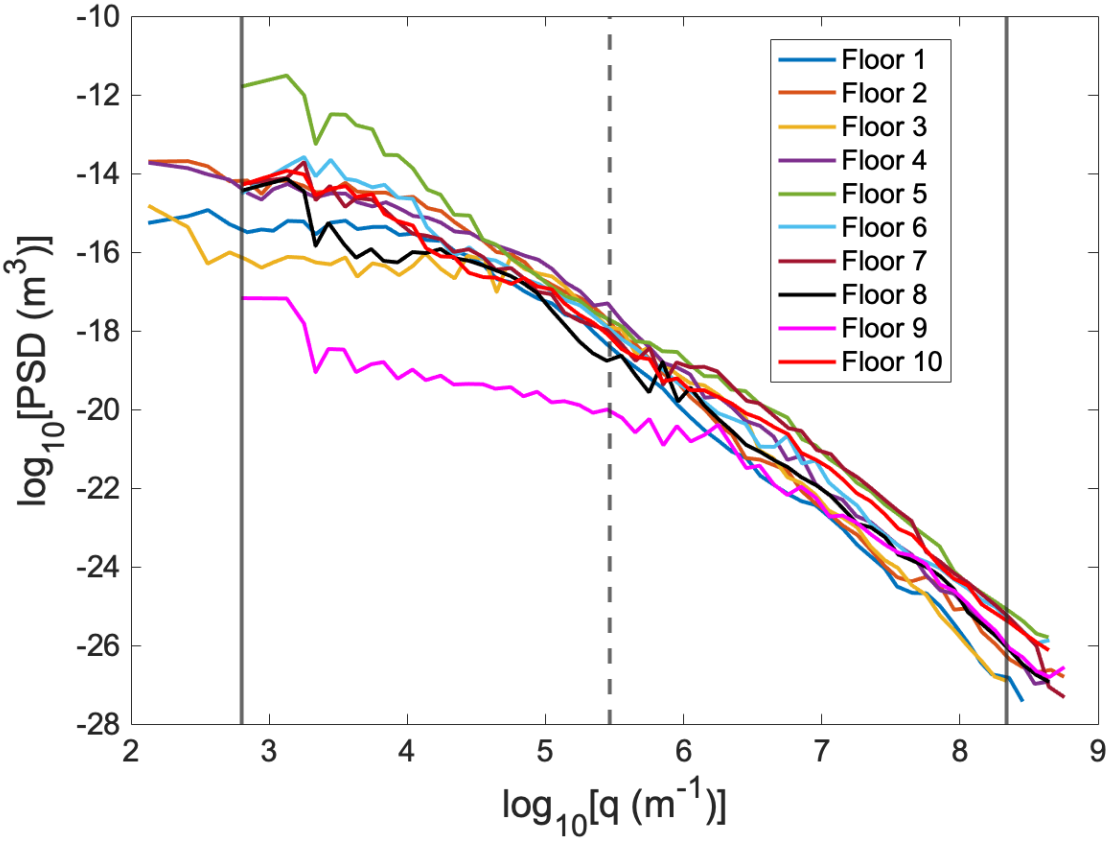

Figure 22: The PSD curves for each floor using stylus profilometry and SEM where the solid vertical lines indicate the full range of size scales used in COF predictions. The dashed vertical line represents a previously determine optimal q_1 value of 2.905*10^5 m^{-1} to optimize the determination coefficient (see Study #3).

E.4.1.2.3.Shoe material moduli data collection

DMA was performed for all shoe materials by another group (Decathlon, Villeneuve-d'Ascq, Lille, France) using the DMA 150+ (Metravib, Limonest, France). Shoe outsole samples with a 10 mm diameter and 1.8 mm thickness were collected. Samples were tested at temperatures ranging from -60° C to 30° C. This temperature increased by 1° C per minute until a 5° C increment was reached. At each 5° increment, the temperature was kept steady for 8 minutes before a 0.5% deformation was applied at frequencies ranging from 1 to 100 Hz. Time-temperature superposition was then used with a reference temperature of 20° C to create the master curve for the given material. This master curve used the temperature changes to shift the material responses to account for the full range of frequencies. This DMA procedure measured the shear modulus (G) of each material, thus the relationship between the shear modulus, complex modulus, and Poisson's ratio (Equation 16) was used to transform the data to the material parameter used in the model (Young's modulus).

$$E = G * [2(1 + \nu)] \quad \text{Eq. (16)}$$

A)

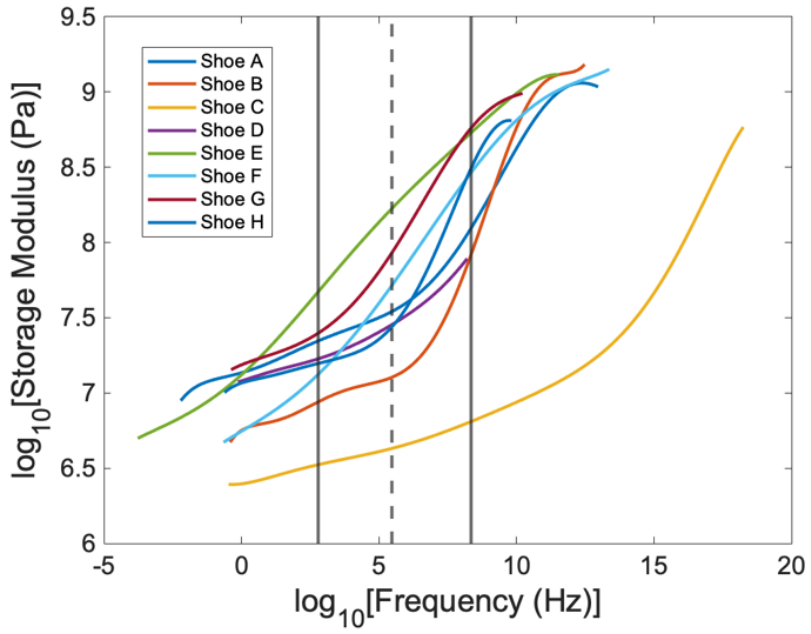

B)

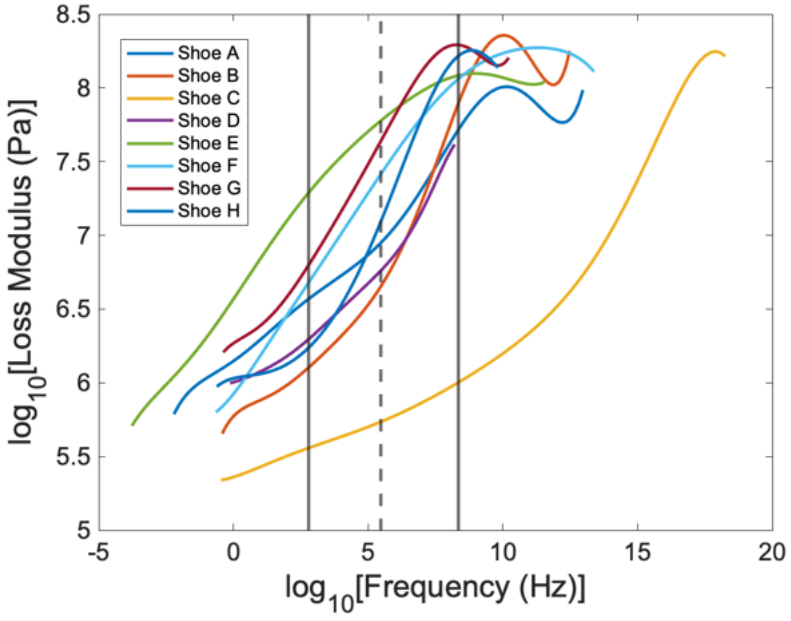

Figure 23: The A) storage and B) loss moduli for all shoe outsole materials where the solid vertical lines indicate the full range of size scales used in COF predictions. The dashed vertical line represents the optimal q_1 value of 2.905*10^5 m^{-1} to optimize the determination coefficient from a previous study (See Study #3).

E.4.1.2.4.Statistical analyses

In order to validate the model, a bivariate correlation analysis was performed between the model predictions (independent variable) and experimental results (dependent variable) for each shoe and floor combination. The determination coefficient, R^2, p value ($\alpha = 0.05$) and RMS_{error}, were calculated for each correlation analysis. The first bivariate correlation was performed between the experimental results and the predictions using the initial range of wavevector size scales (full range). Next, the effects of varying the wavevector limits of integration and thus the included asperity size scales on the predictiveness of the model were tested. Model predictions were calculated using a constant lower q cuttoff (q_L) and varying upper q cuttoffs (q_1) ranging from the original limit of integration and 1*10^3 m^{-1}. For each cutoff value used, R^2 was calculated between the original experimental results and the predictions of the q_1 value used. The same method was used again, however with a constant q_1 value and varying q_L values ranging from the original limit of integration and 1*10^6 m^{-1}. The results with the highest R^2 value were reported to indicate improvement of model predictions when removing certain size scales. The same cutoff analyses were performed in a prior study from this research group with the same floors but different shoes (3 shoes, different tread patterns) (Study #3, Section E.3.). Thus, the regression equation from the correlation analysis with the predictions using the optimal q_1 value of 2.905*10^5 m^{-1} was validated. This prospective validation for the regression equation was performed by using the same upper wavevector cutoff value to make predictions with the shoes and floors from this study. These results were input into the equation and then compared to the experimental results in a final correlation analysis.

E.4.2. Results

The mean and standard deviation of the experimentally measured COF results using the slip tester were 0.108 and 0.068 respectively, with values ranging from 0.024 to 0.317. When using the full range of available size scales, the COF predictions had a mean of 2.451 and standard deviation of 1.762 with results ranging from 0.220 to 7.562. The initial bivariate correlation analysis using these results yielded an insignificant correlation between the experimental and predicted COF values (Figure 24, $R^2 = 0.045$, p = 0.060, RMS$_{error}$ = 0.069).

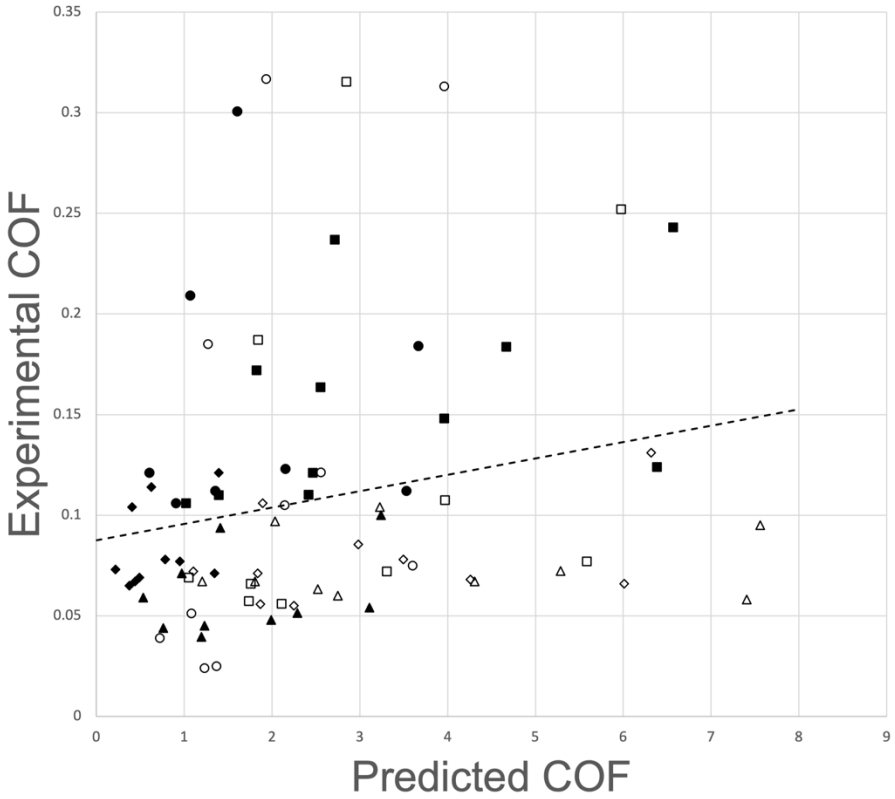

Figure 24: Bivariate correlation analysis between the model predictions using the full range wavevector size scales and experimentally measured results. The dashed line shows the regression line for this analysis. Different shoes are denoted by marker types, both solid and hollow.

New COF predictions were calculated using varying q_1 values. The R^2 between these new sets of predictions and the experimental values were plotted against the cutoff value used (Figure 25). The q_1 value corresponding to the greatest R^2 value was 6.011*10^4 m^{-1}, equivalent to a wavelength of 1.045*10^{-4} m. This was within a range of cutoff values of approximately 1*10^4 m^{-1} to 1*10^6 m^{-1} where the R^2 value was greater than 0.25. The predictions using this q_1 value had a mean of 0.104 and standard deviation of 0.096 with results ranging from 1.79*10^{-5} to 0.487. The bivariate correlation with this set of predictions (Figure 26) resulted in an R^2 value of 0.341 with $p < 0.001$ and an RMS_{error} of 0.055. The same correlation analyses performed with varying q_L values showed that the greatest R^2 value came from using the original lower limit of integration (Figure 27). The predictions using the q_1 value regression equation from a previous study had a mean of 0.135 and standard deviation of 0.055 with results ranging from 0.061 to 0.283. The correlation with this set of predictions (Figure 28) resulted in an RMS_{error} of 0.058.

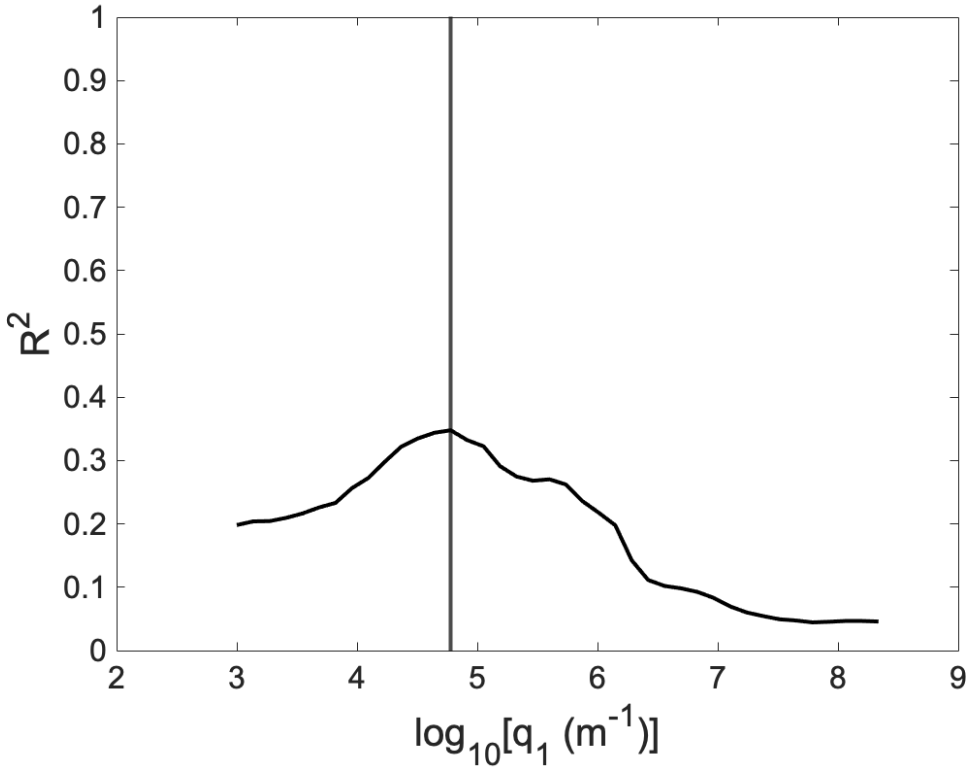

Figure 25: A plot of the determination coefficient versus the upper q limit of integration (q_1) used for all COF calculations. The vertical line shows the cutoff corresponding to the greatest R^2 value.

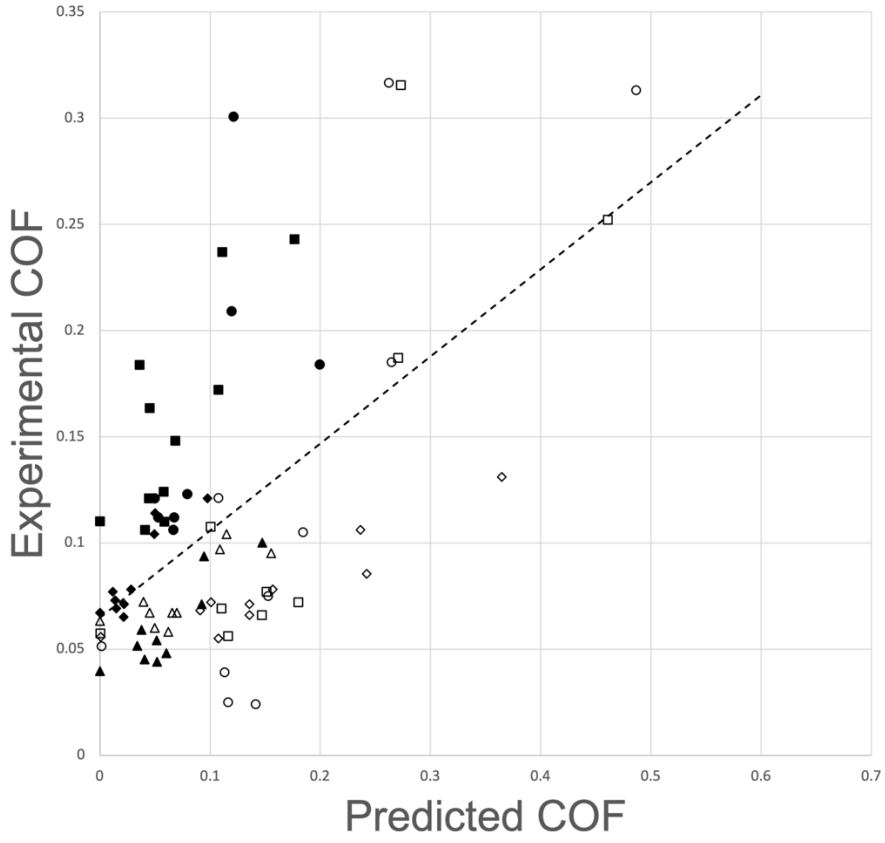

Figure 26: Bivariate correlation analysis between the model predictions using an upper q limit of integration of 6.011*10^4 m^{-1} and experimentally measured results. The dashed line shows the regression line for this analysis. Different shoes are denoted by marker types, both solid and hollow.

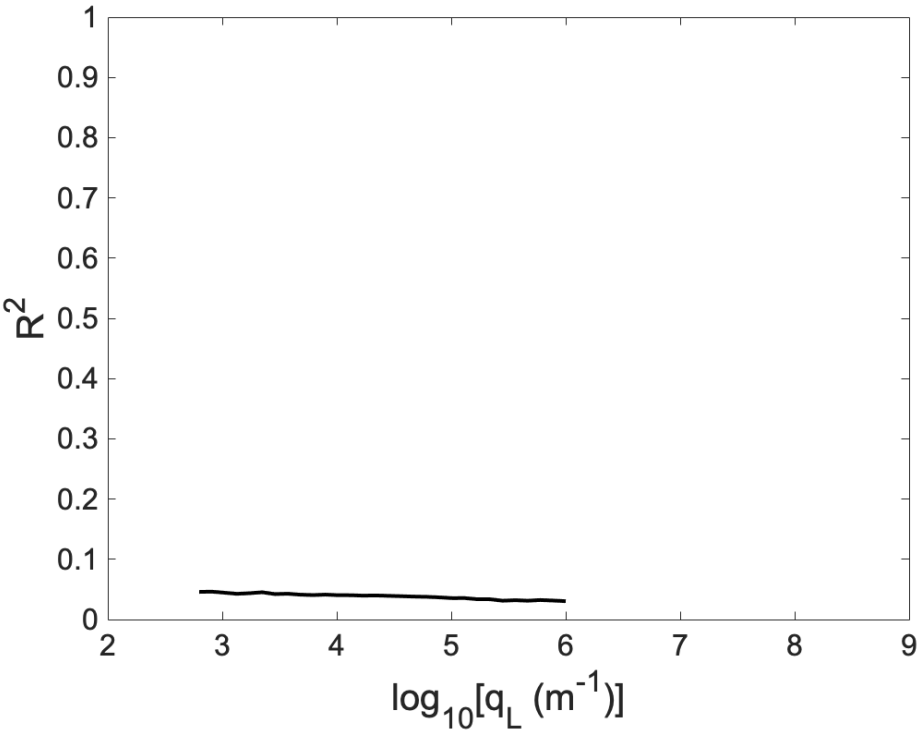

Figure 27: A plot of the determination coefficient versus the lower q limit of integration (q_L) used for all COF calculations.

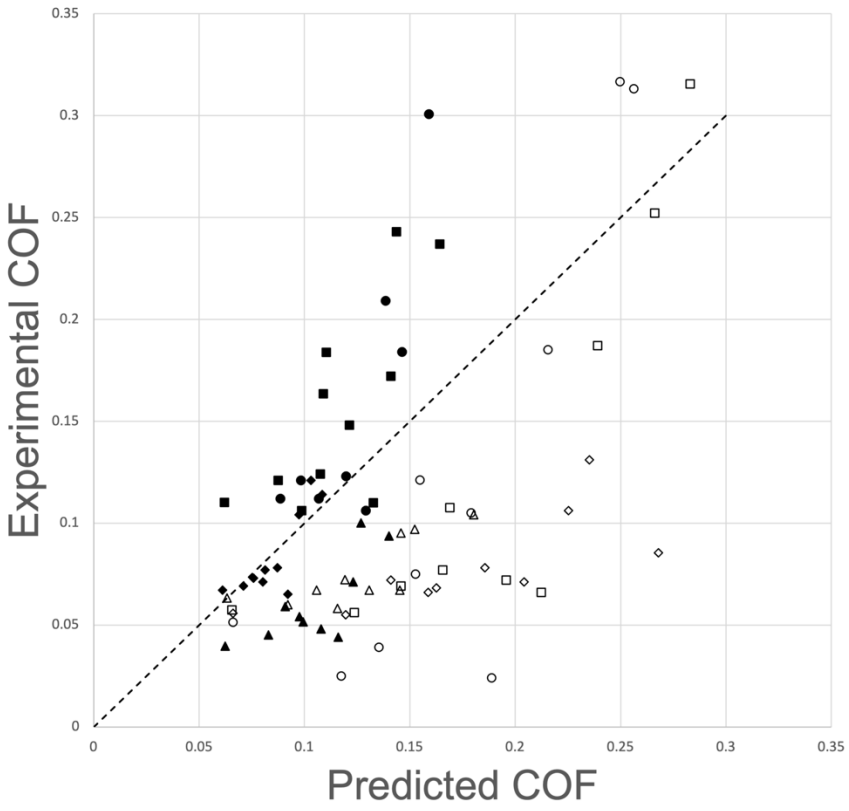

Figure 28: Bivariate correlation analysis between the COF model predictions using the regression line from the bivariate correlation corresponding to an upper q cutoff (q_1) of 2.905*10^5 m^{-1} found from a previous study (Study #3, Section E.3) and the experimentally measured results. The dashed line shows a trendline with a slope of 1 for reference. Different shoes are denoted by marker types, both solid and hollow.

E.4.3. Discussion

The model was not significantly predictive of friction when using the full range of size scales available (p = 0.060, $RMS_{error} = 0.069$). The predictive ability became significant (p < 0.001, $RMS_{error} = 0.055$) when excluding small-scale topography, with an optimal upper wavevector cutoff of 6.011*10^4 m^{-1}. Excluding larger scale features did not improve the model's ability to predict friction. These COF model calculations were greater than the experimental results but were within an order of magnitude when small-scale topography was excluded. Additionally, the prospective validation using the regression equation from the previous study (Study #3, Section E.3.) yielded results with the same order of magnitude as the experimental results ($RMS_{error} = 0.055$) The specially made shoes improved the model validation process. Shoe geometries and tread patterns impact friction [77, 78] but are not included within the model. Therefore, the use of these shoes allowed the effects of just the materials properties on friction to be isolated.

Other models predicting shoe-floor friction exist with varying methods and predictive abilities. Previous work from this research group developed a multiscale finite element model [74] and a statistical model [34, 75]. Although not reported, the RMS_{error} for each model was 0.11 and 0.05 respectively, calculated based on available data in each study. The RMS_{error} within this study was 0.06 when ignoring smaller size-scale asperities. This is close to the results from these other models while also offering some advantages. Finite element models require an in-depth understanding of the software as well as access to a license to use it. Experiments can also be time intensive, especially when using a multiscale approach. The integration techniques used to code the model examined in this study allow predictions to be made much faster. Also, this model can be used significantly more easily than a finite element analysis model. With the developed code, only the inputs and parameters would need to be updated before obtaining a COF prediction. Therefore, the model used in this research offers predictive ability on par with others while providing faster predictions and being easier to implement.

This work offers three potential use cases for the viscoelastic hysteresis model presented. The first is to use the model to predict how floors with different roughness impact friction when contaminants are present. With access to PSD data for a range of floors, the different curves only need to be input into the model to identify which is predicted to offer increased friction. The second is to predict how shoe materials affect friction. For many companies working with materials, DMA data is readily available. This model can parse through these different inputs to compare how the varying materials affect friction. Then, the ideal material based on those predictions can be selected. The final use case is for safety professionals. If DMA and PSD data were accessible for shoes and floors respectively, the different options for a workplace could be input into the model. Then, the shoe-floor combination yielding the greatest COF prediction could be used.

Different limitations were present while completing this study. The first was the inability to perform multiple DMA tests on each material. As only one set of data was available, effects of variability in the testing process on COF predictions could not be examined. Also, although some explanations exist regarding how contaminants contribute to the improved predictions once removing smaller topography size scales, only one contaminant was tested. With increased testing, how specific characteristics of contaminants effect friction could be identified. The optimal upper wavevector limit of integration could also be examined to find how it may change depending on the contaminant used.

In conclusion, the present viscoelastic hysteresis model developed by Persson [27] was validated in its use to predict oily shoe-floor friction when ignoring small-scale surface asperities. The wide range of shoe materials examined, and the identical geometries allowed for a better characterization of how material properties affect model predictions. Furthermore, this model was able to make predictions with similar accuracy to other but is faster and easier to use than finite element

models. These results can inform shoe and floor designers or safety professionals to increase friction and make safer workplaces.

E.5. Study #5: Which asperity scales matter for true contact area? A multi-scale and statistical investigation [79]

E.5.1. Analysis of Surface-Topography Data

This work uses as raw input the composite power spectral density *PSD* from Gujrati *et al.* [47] in its analysis of surface parameters and rough-surface contact. The power spectral density is a mathematical tool that separates contributions from different length scales, and is equal to the square of the Fourier transform of the measured surface heights [45]. It can be computed for individual measurements, but also presents a useful method for combining many measurements across different scales. The composite spectrum, shown in Fig. 29, is the log-space average of all individual measurements from stylus profilometry, atomic force microscopy, and transmission electron microscopy. All raw data associated with the original surface can be accessed at Ref. [80]**.**

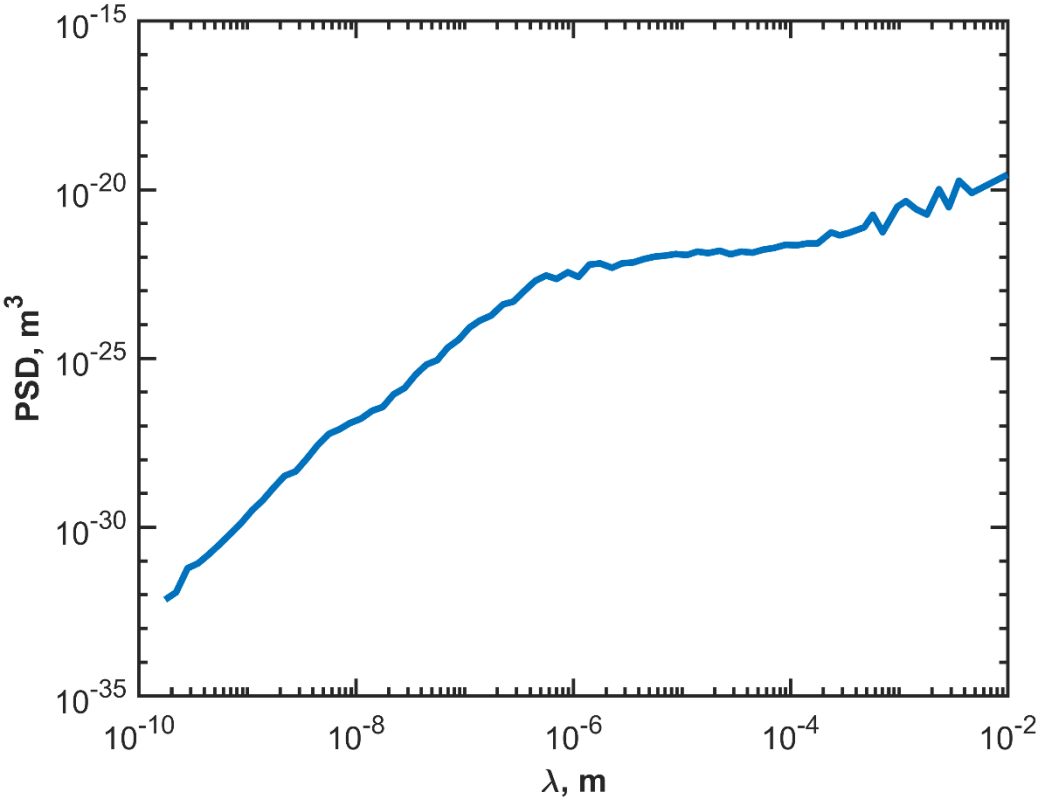

Fig. 29: The composite power spectrum of a surface obtained by multiple measurements from different instruments.

In several previous studies [81, 82], it has been shown that many surface roughness and statistical parameters vary with scale. This was one of the driving factors giving rise to the usage of fractals for describing surfaces [83]. In the paper by Kogut and Jackson [81], the trends of the spectral moments were only examined over two orders of magnitude of length scale from a generated fractal surface. The statistical variance m_0 changed least with the inclusion of smaller scales, but m_2 and m_4 both changed by many orders of magnitude. Later, Green provided closed-form solutions to the spectral moments of fractal surfaces following the Weierstrass-Mandelbrot formulation [84]. Brown *et al.* reviewed the methods to characterize multiscale surfaces [85]. According to Parseval's law, surface descriptors should be able to be calculated equivalently in real- or frequency-space, although Kalin *et al.* [86] showed that the spectral-based parameters of rough surfaces often differ from those acquired directly

from the surface by deterministic counting of the asperities. They attribute the differences to varying definitions of asperity-peaks between deterministic and statistical analysis.

For the present modelling approach, scale-dependent moments were calculated, and then used to compute key roughness descriptors using the method of McCool [87]. First, spectral moments from the composite spectrum were computed according to Gujrati *et al.* [47]:

$$m_k = \int_{\lambda_c}^{\lambda_u} (2\pi)^{k+1} (\lambda)^{-(2+k)} \, PSD \cdot d\lambda \qquad \text{Eq. (18)}$$

The wavevector ω is often used in previous literature [47] and is related to the wavelength λ by $\omega = 2\pi / \lambda$. Equation 18 is numerically integrated to obtain the needed spectral moments (m_0, m_2 and m_4) over the range of scales available, i.e. between λ_u and λ_c, the upper and lower limit of the wavelengths of the composite spectrum. Ideally, λ_u is ∞ and λ_c is 0, but this is not obtainable for experimental surface data. λ_c is also referred to as the cut-off wavelength and represents the smallest scale of roughness considered.

The results of this integration agree well with the real-space surface parameters measured directly in Gujrati *et al.* [47]. By interrupting the integration given in Eq. 18 at different ranges of scale, or in other words by varying λ_c, one can evaluate the influence of smaller and smaller surface features as compared to what was available in prior studies that used conventional topography measurements. The results of this analysis are shown in Fig. 30. These scale-dependent spectral moments are similar to the scale-dependent roughness parameters discussed in Sanner *et al*. [88] and for other surfaces in a previous work [81]. The results show that the moments can change by many orders of magnitude with the inclusion of increasing details of roughness (especially m_2 and m_4).

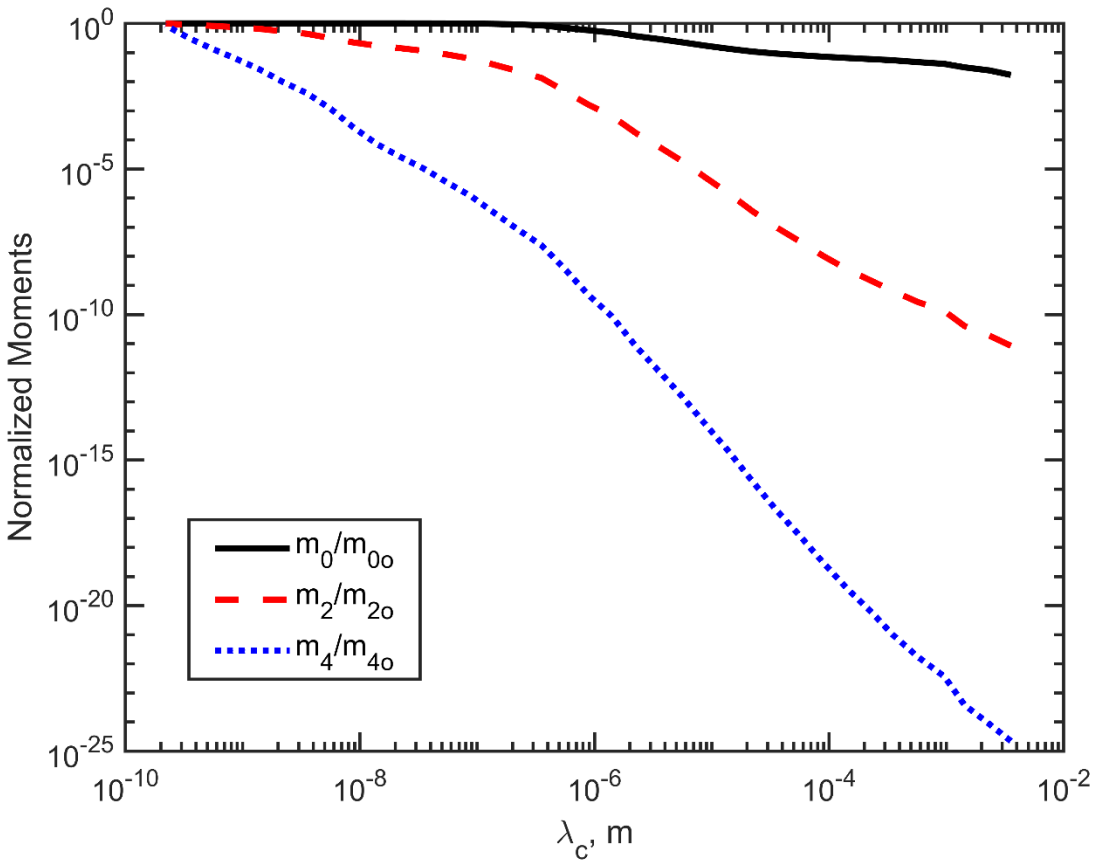

Figure 30: The normalized spectral moment obtained from the composite spectrum as increasingly smaller scales of roughness are included (indicated by wavelength).

The aforementioned spectral moments are related to real-space parameters to be used as inputs to the statistical model using the approach of McCool [89]. In the current work, the statistical model will consider both spherical and sinusoidal shaped asperities, and therefore we will start with the original parameters of the spherical asperity-based statistical models. The expression of m_0 is the same as the square of the RMS roughness, R_q, i.e., $m_0=R_q^2$. The moment m_2 is related to the RMS slope, $\bar{g}$, of aline contour such that (note that for a surface a factor of $\sqrt{2}$ must be included)

$$\bar{g} = \sqrt{m_2} \qquad \text{Eq. (19)}$$

Finally, the moment m_4 is related to the RMS curvature of the surface. However, to find the RMS radius of curvature at the tips of the asperities on the surface, the following equation from McCool [90] is employed. This will be used later when employing the statistical contact model to evaluate the effect of roughness on contact area.

$$R = 0.375\sqrt{\frac{\pi}{m_4}} \qquad \text{Eq. (20)}$$

In addition, the areal asperity density is computed as:

$$\eta = \frac{m_4}{6\pi\sqrt{3}m_2} \qquad \text{Eq. (21)}$$

The elastic modulus, E, and the Poisson's ratio, ν, of the UNCD material is taken to be 463 GPa and 0.20, respectively, from Ref. [91]. Following the same work, the strength of the UNCD is 1.8 GPa. The composite modulus E^* between the surfaces is then calculated by assuming that the opposing surface is rigid.

Another method to evaluate the surfaces is to compute the *amplitude spectrum* of the surface Δ_i, which yields the amplitudes of the sine waves in the Fourier spectrum. Specifically, the amplitude of the composite PSD at each wavelength was extracted by taking the square root and dividing by wavelength. Note that a scaling factor of 1.5 was included [92] because a Hanning window was used to produce the PSD. Thus, the function to calculate amplitude from the PSD is

$$\Delta_i = \sqrt{\frac{PSD_i}{1.5\lambda_i}} \qquad \text{Eq. (22)}$$

where i denotes the index in the power-spectrum array. This transformation results in the amplitude spectrum shown in Fig. 31.

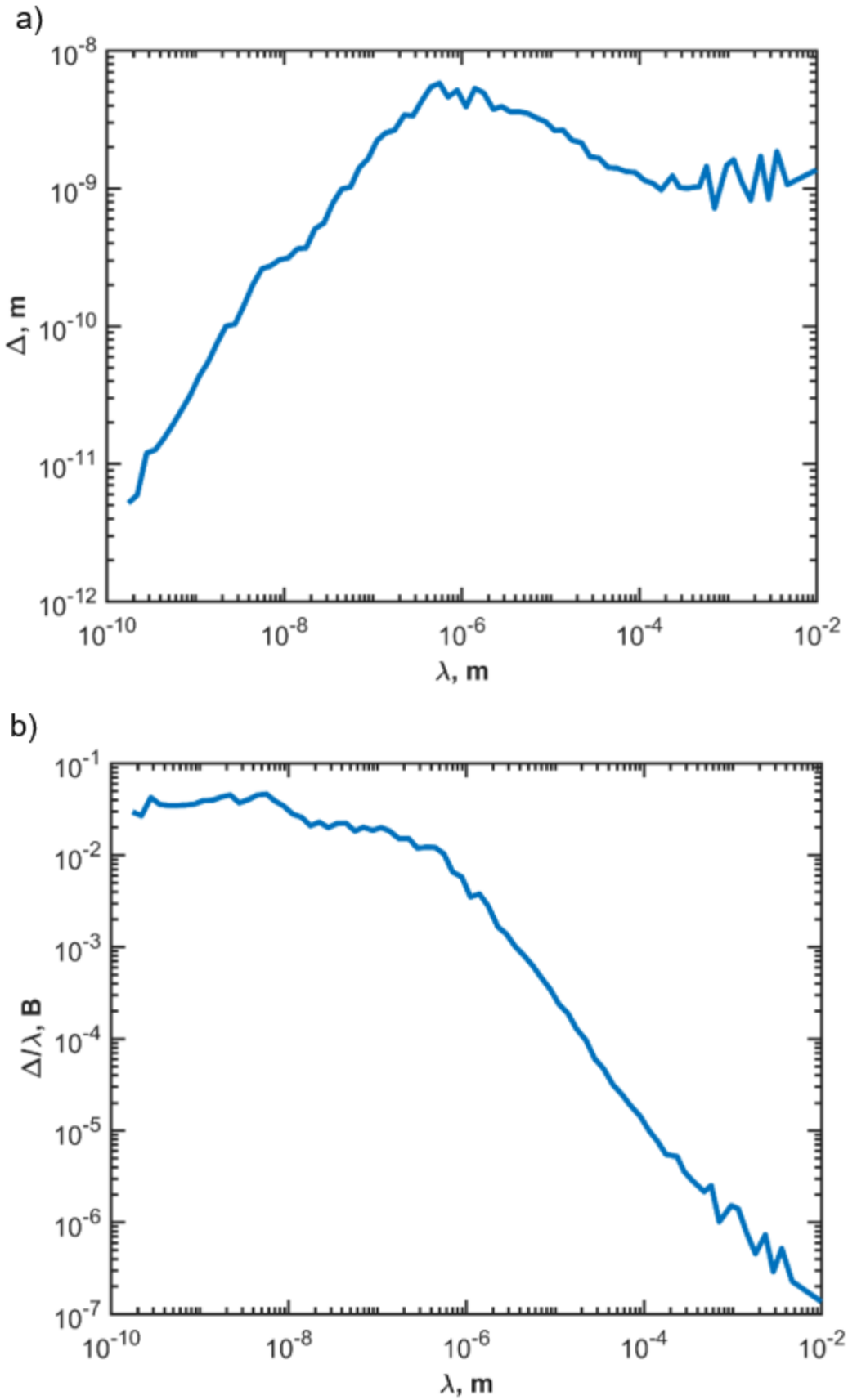

Fig. 31: Amplitude spectrum computed from the composite PSD (a), and the wavelength-normalized spectrum of the surface, also called the aspect-ratio spectrum (b).

In an investigation analyzing the multiscale nature of rough-surface contact using a stacked, or Archard framework, an alternative spectrum was used: the *aspect-ratio spectrum*, which is computed by normalizing the amplitude by wavelength [93]. The resulting values indicate the aspect ratio of the asperities at each wavelength, thus indicating how pointy or blunt the asperities are at each scale. As shown for elastic and elastic-plastic solutions of wavy surface contact, the pressure required to flatten the asperities is proportional to this ratio, Δ_i/λ_i, to which the variable *B* has been assigned [93, 94] . The aspect-ratio spectrum using this method is shown in Fig. 31b.

If *B* were constant across all scales, this would indicate that a surface's asperities (the peaks on a rough surface) have the same aspect ratio or shape across all scales. This structure would indicate a self-similar fractal surface. Alternatively, the plotted *B* will have a sloped line for self-affine surfaces. In the resulting curve shown in Fig. 31b, the curve is nearly linear over many scales, but bends and becomes horizontal (nearly constant) at smaller wavelengths. Therefore, it appears that the spectrum of the surface is nearly *self-affine* across most size scales, but is nearly *self-similar* at the very smallest wavelengths (below approximately 10 nm).

E.5.2. Results and Discussion

E.5.2.1.Elastic and elastic-plastic models of contact for a real-world multi-scale surface

The amplitude spectrum depicted in Fig. 31 is used as input to the multiscale model as originally described by Archard [95] and later refined by Ciavarella and Demelio [96] for fractal elastic contact and by Jackson and Streator [97] for general elastic-plastic rough surface contact. The latest iteration of the model uses sinusoid-shaped contact models to render the asperities characterized by the waves of the spectrum [98, 99]. The usefulness of this method is that it considers the multiscale nature of surfaces but does not assume that they are purely fractal.

The stacked multiscale models do make several assumptions that result in limitations. The version of the stacked models used in this work assume that all of the asperities at a given scale have uniform amplitudes and wavelengths. Therefore the statistical variation at these scales is not considered. In addition, the model uses an elastic-perfectly plastic wavy contact model that neglects strain hardening. Adhesion is also neglected, but in many cases may not be important. The stacked model assumes that the scales of asperities are stacked in mechanical series, with smaller scale asperities higher in the stack. The scale is defined by the wavelength of the asperities. This would neglect that a small scale wavelength of asperities might actually be taller than other scales and bypass the hierarchal stacking. However the model does capture some important mechanisms, including the coupling and coalescing between adjacent asperities, and that in many cases smaller scale asperities would be superimposed upon larger asperities.

The results of the multiscale model using the full amplitude spectrum are shown in Fig. 32. Although the model predicts different contact areas for different loads, and with and without plastic deformation included, interestingly the contact area appears to converge at the same wavelength of approximately 5.65 nm. This scale or wavelength is also close to the range predicted by Thimons et al. [100]. This wavelength actually corresponds to a peak in the *B* value shown in the flattened region of Fig. 31b. This wavelength turns out to also be the maximum value of *B* (0.0463) for this surface. That this maximum value of *B* corresponds to the real contact area agrees in concept with a previous simplified version of the model [93, 101] that theorizes that the real area of contact is approximately equal to force divided by the pressure to flatten the most resistant peaks. In this case the most resistant peaks would be the wavelengths with the highest value of *B*. Although the scale of the most resistant peaks could shift with scale-dependent strength (See Sect. 5.2.2). In addition, Fig. 32 shows that the real contact pressures predicted by the elastic-plastic models are approximately eight times higher than the hardness (conventionally three times the yield strength). This is consistent with earlier investigations where contact pressure exceeded the hardness [102, 103]. This occurs from asperities coalescing and resulting in hydrostatic stress rather than deviatoric stress.

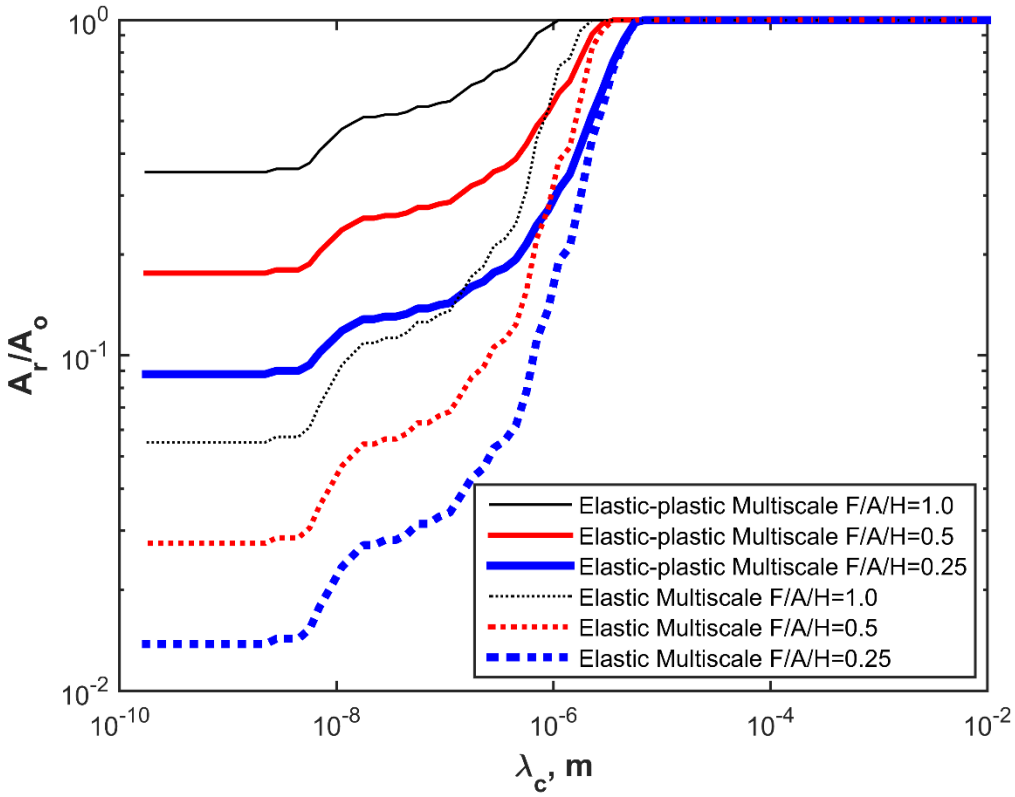

Fig. 32**:** Real contact area predicted by the stacked multiscale type model as smaller wavelength scales are included.

In addition to the multi-scale model, four different versions of statistical rough surface contact models were also used to make predictions of the real area of contact (see Table 5). All of the statistical models assume a Gaussian height distribution. The previously described spectral moments and statistical parameters are employed (Eqs. 18-22). The first elastic statistical model employs the elastic Hertz contact solution for the asperities (i.e. the Greenwood and Williamson model [33]). Elastic-plastic spherical asperity contact was also used in the statistical model for comparison (see [104] for details). In the elastic-plastic spherical asperity model the ratio between the fully plastic pressure (i.e. hardness) and yield strength decreases as the contact area increases. In addition, some of the taller asperities can be heavily loaded and flattened. In those cases the contact area of a single asperity was limited by the projected area of the spherical asperity (πR^2).

Table 5: List of Considered Statistical Rough Surface Contact Models

Asperity Model	Abbreviation	References
Elastic Hertz Statistical Model	Elastic Hertz Stat.	[33]
Elastic-plastic Spherical Statistical Model	EP Sphere Stat.	[104]
Elastic Sinusoidal Statistical Model	Elastic Sine Stat.	[98, 105]
Elastic-plastic Sinusoidal Statistical Model	EP Sine. Stat.	[98, 106]

As an alternative, elastic and elastic-plastic sinusoidal asperity models [105] were also used within the statistical framework (details are in [98]). There are multiple methods of converting the statistical surface parameters to amplitude, Δ, and wavelength , λ, in the statistical models; the present technique

was proven effective in prior work [98]. In this method the wavelength of the asperities is obtained based on the areal asperity density, or

$$\lambda = \sqrt{\frac{2}{\eta}} \qquad \text{Eq. (23)}$$

Next, the amplitude is predicted based on the asperity curvature as

$$\Delta = \frac{1}{R}\left(\frac{\lambda}{2\pi}\right)^2 \qquad \text{Eq. (24)}$$

Other details of the elastic-plastic sinusoidal asperity model are found in [98, 106].

The statistical model, although probably the most widely used rough surface contact model, is also built upon assumptions and has limitations. The statistical model used in this work assumes that all asperities possess the same average radius of curvature, *R*, even though they have different heights that are based on a Gaussian distribution. This of course neglects that asperities can vary in curvature, can be elliptical, and not follow the Gaussian distribution. In contrast to statistical models more closely related to the original GW model, the current model does consider some lateral interaction between asperities and substrate deformation by employing elastic and elastic-plastic sinusoidal asperity models as previously noted. One might observe that the stacked and statistical model assumptions differ and complement each other.

The resulting predictions of the elastic and elastic-plastic spherical statistical models are shown in Fig. 33. Note that it is plotted differently than the multiscale model because the statistical models are formulated to predict contact area and force as functions of mean surface separation, whereas the stacked multiscale model makes predictions of contact area directly from the force. As expected, the elastic statistical contact models predict much lower contact areas than the elastic-plastic version of the models. The elastic models appear to be exceptionally dependent on the cut-off wavelength (*i.e.*, λ_c, the smallest considered wavelength of the spectrum). The contact area varies by approximately one order of magnitude when the cutoff wavelength (λ_c) is varied by two orders of magnitude. However, the elastic-plastic models do not appear to vary as much with cutoff wavelength (λ_c). This agrees with the multiscale model findings that at a wavelength on the order of 10 nm the predicted contact area levels off, which is approximately 10 times λ_u (the smallest measured wavelength). Following this trend, the prediction of the elastic-plastic statistical model for $100\lambda_u$ appears to start to deviate slightly from the predictions considering smaller scales.

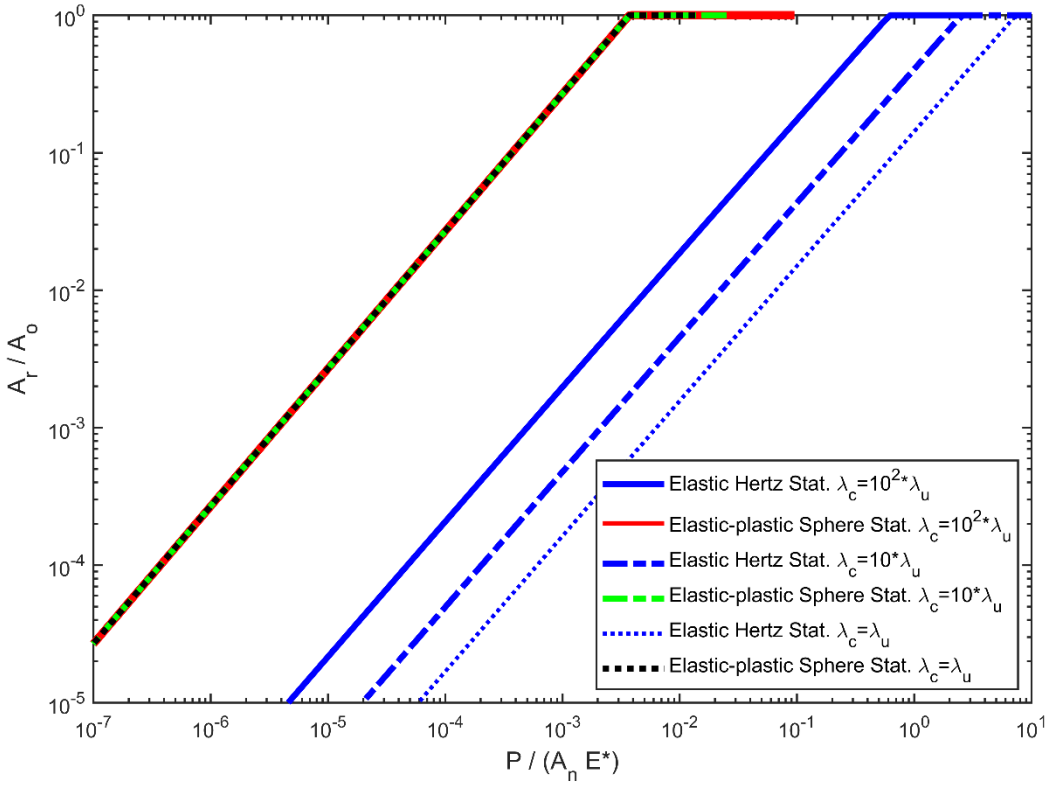

Fig. 33**:** Real contact area predicted by statistical models as different ranges of wavelength scales are included. The elastic-plastic sphere-based statistical models all fall on nearly the same curve (yellow, green and black).

Since the scales of considered spectrum clearly influence the predictions of the multiscale model, a similar evaluation of the statistical models is desirable. Therefore the real contact area from the statistical model was calculated at constant loads as a function of cutoff wavelength. To accomplish this the results for the specific loads must be searched for numerically, since, in the statistical model, the contact area and force equations are functions of the surface separation, as opposed to the multiscale model which are functions of load.

The resulting predictions of the elastic and elastic-plastic spherical and sinusoid asperity statistical model are shown in Fig. 34. From Fig. 34, only the elastic-plastic spherical based statistical models makes predictions that are in qualitative agreement with the multiscale models. The slope of the elastic Hertz-based statistical model does start to flatten with smaller scales, but it never becomes horizontal. The elastic sinusoidal-based statistical model is not shown in Fig. 34a, but Fig. 34b shows the isolated results of both the sinusoidal-based statistical models. All versions of the statistical models suggest that with the inclusion of smaller scales of asperities, that the contact area decreases. Both the elastic-plastic spherical and sinusoidal asperity-based statistical models predict a marked increase in contact area compared to the elastic models starting at a cutoff wavelengths (λ_c) below 1-10 μm. The elastic sphere and sinusoidal statistical models do not have a convergence scale or wavelength at which the contact area no longer decreases. This is probably due to the fundamental differences in the statistical and multiscale methodologies, and the spherical and sinusoidal asperity behaviors, which will be discussed in greater detail in Section 5.2.3. Nonetheless, the elastic-plastic spherical statistical models do predict that the contact area converges or stops decreasing with scale at a cutoff wavelength (λ_c) of approximately 100 nm, which is similar to that predicted by the multiscale models. However, even the contact area predicted by the elastic-plastic spherical-based statistical does decrease in the last decade of included scales. This decrease in contact area at the smallest scales does not appear to decrease lower than when the contact area dipped at approximately 1 μm. As with the multiscale models, the wavelength of convergence of the elastic-plastic sphere-based statistical model appears to be independent of load, at least within the range of loads considered.

a)

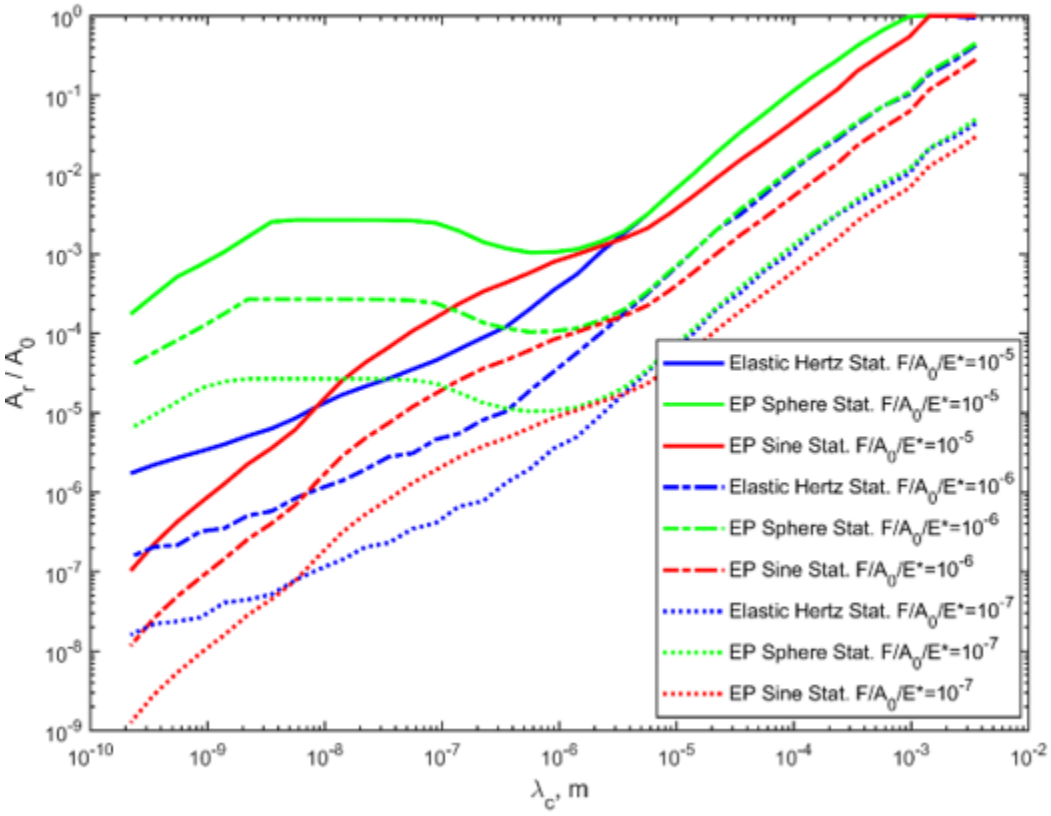

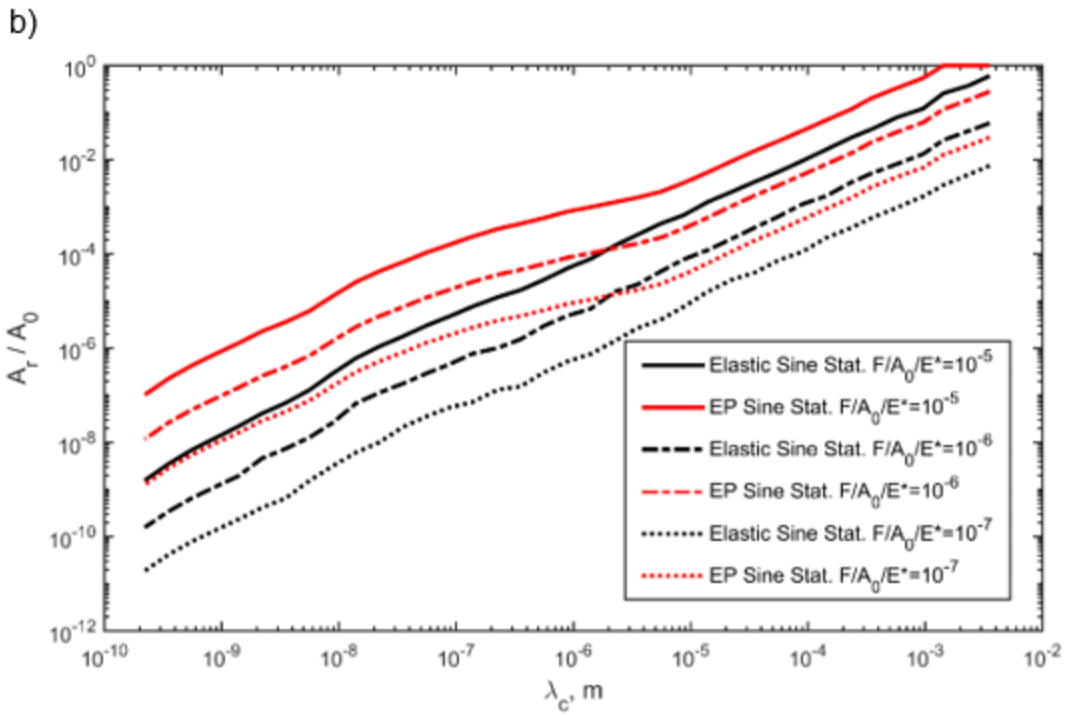

Fig. 34: Real contact area predicted by statistical models for constant loads as a function of the cutoff wavelength based on (a) elastic Hertz, elastic-plastic spherical and elastic-plastic sinusoidal asperities and (b) elastic sinusoidal asperities.

The multiscale stacked model and the statistical model are formulated from different mechanical and mathematical frameworks. The multiscale model assumes that the scales of asperities are stacked on each other, but there is no variation in their height within one scale. In contrast, the statistical models assume that all of the asperities are on the same scale (via the radius of curvature) but have different heights following the Gaussian distribution. Despite these differences, they both make similar qualitative predictions about the influence of smaller scales of asperities on contact area. They both predict that the contact area reduces with smaller scales. The stacked multiscale models and elastic plastic spherical statistical model also all predict that a scale of saturation or convergence is reached.

E.5.2.2.The Effect of Including a Scale-Dependent Strength

As mentioned, the strength of many materials often increases at smaller scales. Since rough-surface contact occurs on different scales simultaneously (ranging from the smallest to largest asperities), and at different loads on different scales of asperities, then the asperity contact areas will cover many orders of magnitude in size. In this work the strain-gradient model was used to approximately include the dependence of strength on size scale. This is similar to several previous studies, such as where Jackson [107] included scale effects in a statistical model, and other similar models that followed using a stacked multiscale framework [108]. The present advantage over prior work is the consideration of strain-gradient plasticity over the broad window of surface topography included here. Fleck *et al.* developed the strain-gradient plasticity theory as a way to consider these scale-dependent effects [109]. Using this theory, Nix and Gao [110] predicted the hardness of a contact to be approximated by:

$$S_y = S_o \sqrt{1 + \frac{h^*}{h_p}} \qquad \text{Eq. (25)}$$

where S_o is the macroscopic yield strength, S_y is the corrected scale-dependent yield strength, h^* is a length scale for the effect, and h_p is the depth of plastic deformation caused by the indentation.

Equation (25) is then used as part of the multiscale surface contact model to consider these scale-dependent effects. The main difficulty in using this model is finding the values of h^*. Usually h^* is on the order of micrometers for polycrystalline materials.

First, note that the upper limit of yield strength is often considered to be approximately a tenth of the elastic modulus, *E* [111]. In this case that would be approximately 40-45 GPa, which is in the upper end of what is predicted in the study on the properties of UNCD by Mo *et al.* [112] for indentations of a few nanometers. The hardness has been reported to be 88 GPa in another paper which results in strength of approximately 29 GPa at indentations depths of 10-40 nm using a Vickers indenter [113].

For modeling purposes and to approximately demonstrate the influence of scale-dependent strength in this work, a value for h^* of 5 micrometers is assumed. Then Eq. (25) is used both in the previously described multiscale and statistical models. In the multiscale model, the yield strength is calculated from the deformation of the previous scale using equations relating contact pressure to average surface separation at that scale [114]. The value of h_p is then given by:

$$h_p = \Delta - g \qquad \text{Eq. (26)}$$

where from [114]

$$\frac{g}{\Delta} = \left(1 - \left(\frac{\bar{p}}{p^*_{ep}}\right)^{A_1 \frac{\bar{p}}{p^*_{ep}} + A_2}\right)^{5/2} \qquad \text{Eq. (27)}$$

Where

$$A_1 = -0.1 \ln\left(\frac{\Delta}{\Delta_c}\right) \qquad \text{Eq. (28)}$$

$$A_2 = \frac{1}{15}\left(\frac{\Delta}{\Delta_c} - 1\right)^{0.44} + 0.99^{0.44\left(\frac{\Delta}{\Delta_c} - 1\right)} - \frac{1}{2} \qquad \text{Eq. (29)}$$

In the statistical model, h_p is calculated based on the asperity-level interference before the area and force are calculated. Specifically, $h_p = h\text{-}d$.

The resulting contact area predicted by the multiscale model including the strain-gradient strength (Eq. 25) are shown in Fig. 35 as a function of the cutoff wavelength λ_c (the smallest wavelength included in the model). Note that the nominal pressures in the legend are normalized by the bulk or macro-scale hardness, *H*, that does not include strain-gradient plasticity. As expected, including the strain-gradient model results in the models predicting lower contact areas, because the effective yield strength is higher. The final contact areas predicted by the strain-gradient elastic-plastic models appear to approach the purely elastic models when all the asperity scales are included, although there are minor differences at intermediate scales. Essentially, for the UNCD surface and properties used in this work, the strain-gradient strength causes the multiscale model to become elastic on the final asperity scales in contact. Also, the contact area appears to converge and not decrease with additional scales at a wavelength between 1 and 10 nm. This suggests that the asperities at scales smaller than this are effectively flattened out. As smaller scales are included the contact area decreases, which also increases the contact pressure. This pressure eventually overcomes all asperities at smaller scales, even despite the increasing hardness at these scales.

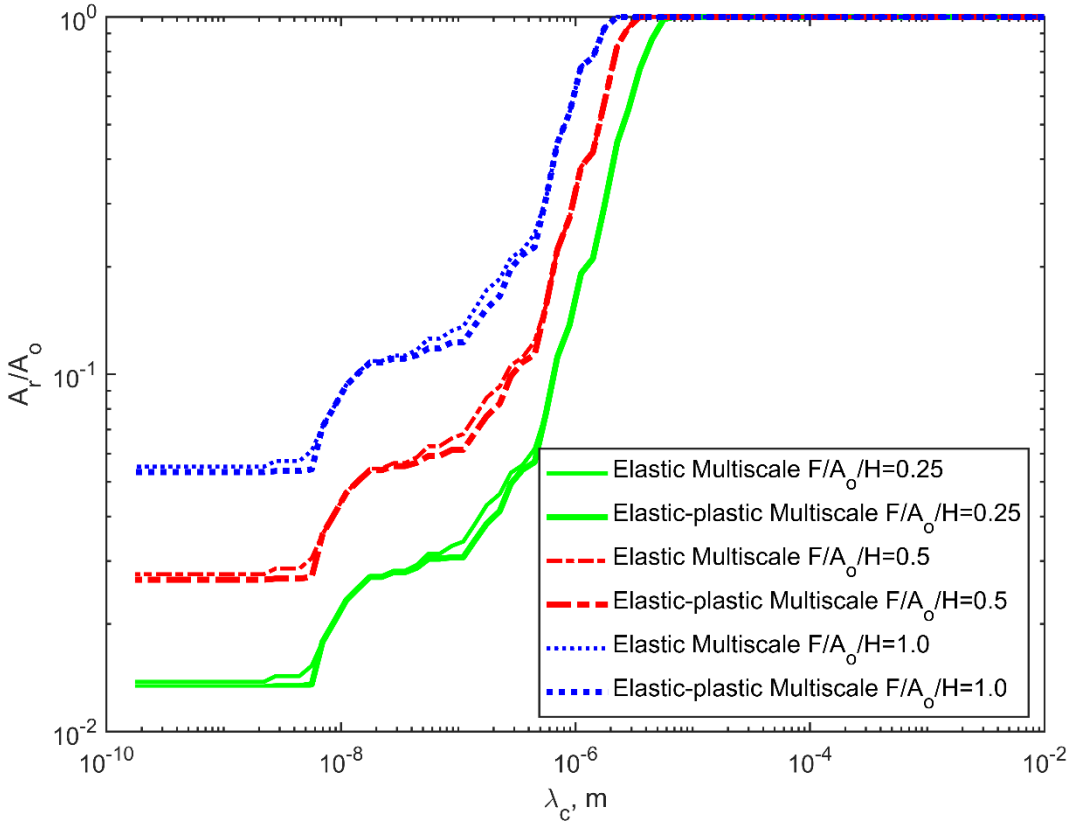

Fig. 35: Scale-dependent real contact area predicted by the stacked multiscale model with a strain-gradient strength. Of course the elastic calculations are unaffected by the strength and so are identical to the curves shown in Fig. 32, but they are shown again here for reference.

Finally, the results of the spherical asperity-based statistical model including the strain-gradient strength are plotted in Fig. 36 and the sinusoidal asperity-based results are shown in Fig. 37. The statistical models with strain-gradient plasticity were again recalculated at constant loads while varying the cutoff wavelength (λ_c). As with the multiscale models, the contact area predicted when including the scale-dependent strength generally decreases the contact area because the strength is increased. However, in contrast to the multiscale model presented in Fig. 35, the predictions of the elastic-plastic spherical and sinusoidal asperity-based statistical models still differ from the purely elastic models' predictions. The results also suggest that the elastic models depend more on smaller-scale roughness features than when plasticity is included. The smaller spherical asperities get plastically flattened out, even despite their increasing scale-dependent strength. However, at the smallest wavelengths of less than a nanometer, the contact area predicted by the elastic-plastic spherical-based statistical models begin to decrease again. For the elastic-plastic spherical asperity-based statistical model results, the contact area appears to approach a converged prediction at a cutoff wavelength of approximately 0.1 μm, which is earlier than but approximate agreement with the multiscale models, and also in approximate agreement with a previous investigation focused on the effect of roughness scale on adhesion [100]. Despite the differences in the underlying assumptions of the multiscale and statistical models, they yield similar trends. Note that this scale of convergence may also depend on the material properties of the surfaces, and the roughness structure outside of these scales.

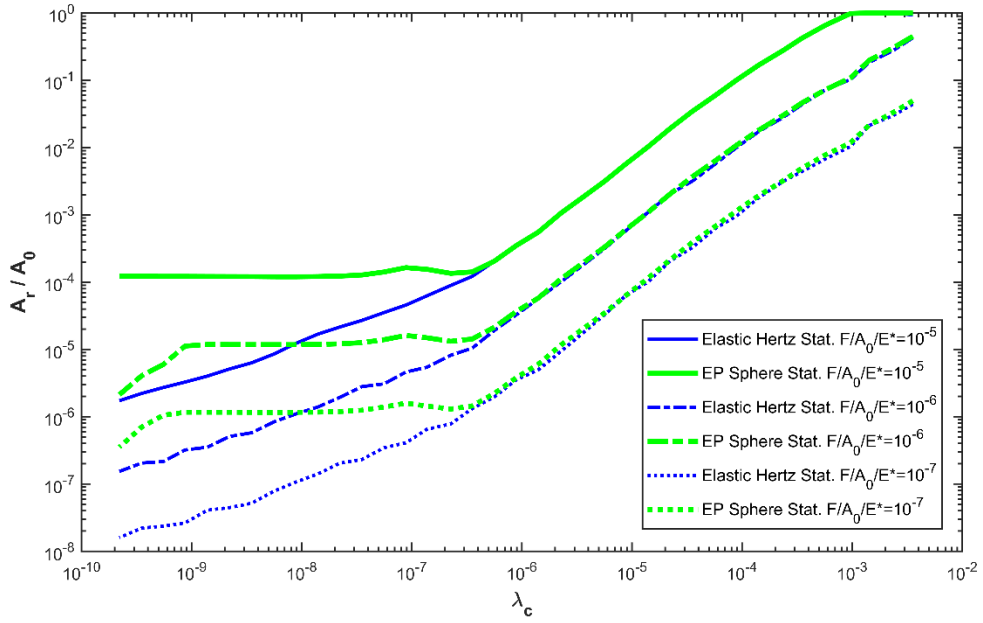

Fig. 36: Scale-dependent real contact area predicted by spherical asperity-based statistical models with the strain-gradient strength included. Once again, elastic calculations are unaffected and are shown here for reference.

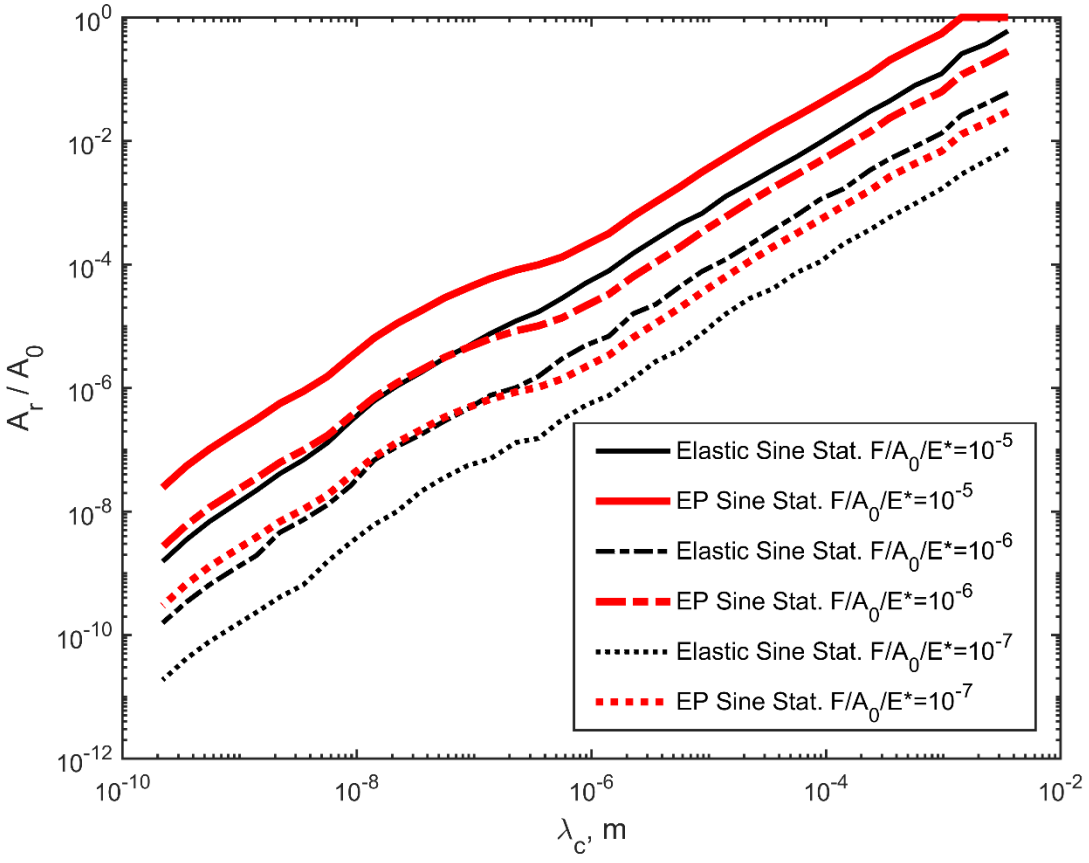

Fig. 37: Real area of contact predicted by strain-gradient sinusoid-based statistical models at constant loads as a function of the cutoff wavelength.

E.5.2.3.Considering all results together

It is interesting to compare the elastic and elastic-plastic curves in Figs. 36 and 37 and the overall results of all versions of the models. All of the models predict an order of magnitude change in contact area with an order of magnitude change in load, which suggests that they predict an approximately linear relationship between contact area and load, as the original statistical and stacked multiscale models did. As the cutoff wavelength (λ_c) decreases, the real contact area begins to generally decrease for all the models; but at different rates that change with the inclusion of smaller scales and in some cases actually increase, but only momentarily. These differences in the statistical model results arise because of the wavy surface asperities used in the statistical models are effectively stiffer than the elastic Hertz and elastic-plastic spherical asperity models. In addition, the elastic-plastic sinusoidal asperity models include the effect of a substrate below them, but the elastic-plastic spherical models do not, which a recent work suggests could be influential [115].

The stacked multiscale and spherical asperity based statistical elastic-plastic models predict that, below a certain scale, the roughness no longer influences the real area of contact. In those cases, the contact pressure is sufficient that smaller wavelengths are eventually flattened and do not further affect the contact area. This also holds when scale-dependent strength is considered, but this case comes into closer quantitative agreement with the elastic model, because the strength increases for the smaller asperities. The statistical models are mostly in agreement with the multiscale model trends, except that the elastic Hertz and the sinusoid asperity based statistical models does not converge (level off) as smaller scales of asperities are included.

The results show that most of the statistical models do not converge as cut-off wavelength decreases, except for the elastic-plastic spherical statistical model. This could partly be due to the decoupling of asperities by the statistical model, but even wavy asperities which do include some coupling still do not converge with the inclusion of additional scales. Another possible reason is that the fully plastic pressure (i.e. hardness) decreases with deformation for the sphere contact geometry, where in contrast it increases for sinusoid geometries. The reason for this is that periodic sinusoidal asperities coalesce at higher loads and the stress approaches a hydrostatic state. According to distortion energy yield theory, hydrostatic stress does not cause plastic deformation. This results in the elastic-plastic sinusoid asperities being more resilient than the spherical ones and therefore less likely to flatten with the inclusion of smaller scales.

Most importantly, the statistical model uses a different mathematical framework that does not consider how smaller-scale asperities might be under higher loads, as the multiscale model does. In reality, smaller asperities or roughness features are usually superimposed upon larger features. This is similar to the concept of self-similarity in fractal roughness. In the multiscale model the pressure increases with the stacking of each smaller scale of asperities and results in a higher likelihood of being flattened. Since the statistical models do not consider this, their results should be given less weight in determining the trends that apply to real-world surfaces. More complex statistical models that include variation of curvature might correct this[116].

Other than the cases of sinusoidal and elastic spherical statistical models, the predictions suggest that most materials will have a certain scale of features below which the roughness will no longer reduce the area of contact. Of course this may vary depending on the particular geometrical structure of the surfaces and the material properties. As suggested in Ref. [93], this might depend on the overall slope of the surface spectrum, which relates to the self-affinity or self-similarity of the spectrum. In general, if surfaces are more self-affine and fractal-like in nature, than the asperities will have taller and thinner aspect ratios with smaller scales, and thus be more resistant to flattening. For the nearly complete surface spectrum considered in this work, the surface appeared self-affine at large scales, but then become more self-similar at smaller scales (see Fig. 31 where the asperity aspect ratio B approaches a constant value at small wavelengths). This enables the ability of the increasing contact pressure to overcome the smaller asperities and flatten them. Note that real surfaces are not exactly fractal and the behavior may deviate from that predicted by pure fractal-based modeling. Adhesion is

also neglected in this work, though depending on the surface energies, could be important in some cases. Despite not including adhesion, the predictions of a critical scale of roughness are consistent with what has been observed experimentally in an adhesive contact [100].

E.5.3. Conclusions

In this investigation, multiscale stacked and statistical models of rough-surface contact were implemented by using the nearly complete spectrum of a rough surface. As expected, all the models predict that contact area will decrease as smaller scales of asperities are included. The elastic Hertz asperity-based and sinusoidal asperity-based statistical models predicted that contact area continues to decrease as smaller and smaller scales; however, all other models (elastic-plastic spherical asperity-based statistical, elastic multiscale, elastic-plastic multiscale) predicted that the contact area flattened out, or converged, at a particular wavelength. Even when scale-dependent strength is considered, this convergence still occurred, though there was a shift in the relevant size scale. It is probable that the critical size at which convergence occurs will vary based on the particular geometrical and material structure of a surface. The physical implication of this result is that, in some cases, roughness need only be considered down to a certain critical size, below which it will have no effect on contact area. Since the statistical models do not consider the scaled hierarchal nature of surfaces, they may be less able to make this prediction accurately. Additionally, all of the models predict that, while plasticity does allow the contact area to converge and reduce the pressure in comparison to the elastic case, the hardness does not limit the contact pressure.

E.6. Study #6: Why soft contacts are stickier when breaking than when making them [117]

E.6.1. INTRODUCTION

Insects, pick-and-place manufacturing, engineered adhesives, and soft robots employ soft materials to stick to surfaces even in the presence of roughness. These materials stick to each other because of attractive van-der-Waals or capillary interactions at small scales [118]. The strength of these interactions is commonly described by the intrinsic work of adhesion w_{int}, the energy that is gained by these interactions per surface area of intimate contact. This work of adhesion is most typically measured from the pull-off force $F_{pulloff} = -3\pi w_{int} R/2$ of a soft spherical probe (see Fig. 35A) with radius R which makes a circular contact with radius a (see Fig. 35B) [119]. For hard solids, the measured *apparent* work of adhesion is smaller than the *intrinsic* value w_{int} because roughness limits the area of intimate contact to the highest protrusions [120, 121]. In contrast, soft solids are sticky because they can deform to come into contact over a large portion of the rough topography. The overall strength of the adhesive joint is then determined by the balance of the energy gained by making contact and the elastic energy spent in conforming to the surface. Following Persson and Tosatti [122], energy conservation implies that surface roughness reduces the apparent work of adhesion to

$$w_{PT} = w_{int} - e_{el} \qquad \text{Eq. (30)}$$

where e_{el} is the elastic energy per unit contact area required to conform to the roughness (Fig. 35C). As shown in Fig. 35D, experiments typically follow different paths during approach and retraction, leading to different apparent values for work of adhesion for making and breaking contact, w_{appr} and w_{retr}. This *adhesion hysteresis* [54, 123] contradicts Persson and Tosatti's balance of energy, which gives the same value w_{PT} for approach and retraction. The common explanation for this hysteresis is either contact aging or viscoelasticity [118, 124].

In this article, we show that adhesion hysteresis emerges even for perfectly elastic contacts and in the absence of contact aging and viscoelasticity because of surface roughness. We present a crack-perturbation model [125-127] and experimental observations that reveal discrete jumps of the contact perimeter. These stick-slip instabilities are triggered by local differences in fracture energy between roughness peaks and valleys. Pinning of the contact perimeter [128-130] retards both its advancement

when coming into contact and its retraction when pulling away. Our model quantitatively reproduces the hysteresis observed in

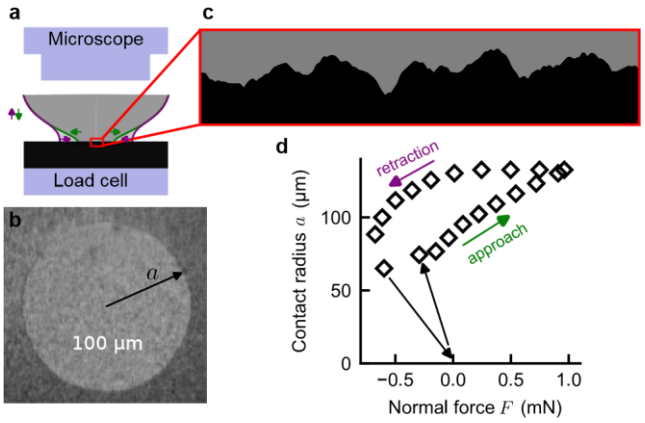

Figure 35: Phenomenology of adhesive contact. **(A)** Many contacts can be described as spheres making contact with a flat surface. For soft materials, microscopic interactions are strong enough that the solids deform substantially near the contact edge. **(B)** The contact forms a circle for contacting spheres, and its radius *a* can be measured from *in situ* optical images of the contact area. **(C)** Most natural and technical surfaces are rough so that the solid needs to elastically deform to come into conforming contact. **(D)** The contact radius is larger and the normal force is more adhesive (negative) during retraction than during approach, as is shown schematically in panel A, with darker gray representing the contact size during approach and lighter gray representing the contact size at the same rigid-body penetration during retraction. The pull-off force is the most negative force on these curves.

experiments and allows us to derive analytical predictions for its magnitude, accounting for realistic rough geometries across orders of magnitude in length scale [47, 131].

For soft spherical probes, we can describe the circular contact perimeter as a crack. The crack front is in equilibrium when Griffith's criterion is fulfilled [132]: The energy per unit area required locally for opening the crack, the fracture energy w_{loc}, is equal to the energy released from the elastic deformation, $G\delta A = w_{loc}\delta A$, where δA is the contact area swept out by the moving crack front. A more common way of writing this equation is

$$G = w_{loc} \qquad \text{Eq. (31)}$$

where both the elastic energy release rate G and the fracture energy w_{loc}, should be interpreted as forces per unit crack length. Johnson, Kendall and Roberts (JKR) [119] derived the expression for the energy release rate G for a smooth spherical indenter, $G = G_{JKR}(b,a)$. Equation (31) then allows the evaluation of not just the pull-off force, but of all functional dependencies between rigid-body displacement b, contact radius a and normal force F during contact.

For smooth spheres, the fracture energy is the intrinsic work of adhesion, $w_{loc} = w_{int}$, which for chemically homogeneous contacts does not vary with position. We will show below that surface roughness can be transformed into a field $w_{loc}(x,y)$, which describes the fluctuation of the effective fracture energy in the equivalent smooth contact. Since the process of opening and closing adhesive contacts is locally reversible, the fracture energy w_{loc} can be interpreted as an effective local work of adhesion. Equation (31) must then hold independently for each point on the contact perimeter. We start our analysis by *assuming* that $w_{loc}(x,y)$ varies with position, and by showing that this is sufficient to yield a hysteresis in the adhesive contact cycle.

E.6.2. RESULTS

E.6.2.1.Axisymmetric chemical heterogeneity

We first demonstrate the physical origin of the adhesion hysteresis using a simplified surface that has concentric rings of high and low adhesion energy, similar to the models by Guduru [133], Kesari and Lew [134, 135] and Popov [136]. Rather than being random, $w_{loc}(a)$ varies in concentric rings of wavelength d as a function of distance a from the apex of the contacting sphere (Fig. 36A). Figure 36B shows $w_{loc}(a)$ alongside $G_{JKR}(b,a)$ for a fixed displacement b. Because of the spatial variations of w_{loc}, there are multiple solutions to Eq. (31) indicated by the labels A and B. Moving into contact from the solution denoted by A leads to an instability where the solution A disappears, at which the contact radius jumps to the next ring of $w_{loc}(a)$. This samples the lower values of w_{loc} shown by the green line in Fig. 36B. Conversely, moving out of contact progresses along a different path that samples the higher values of $w_{loc}(a)$, shown by the red line. The combination of fluctuations in w_{loc} and the elastic restoring force G_{JKR} acts like a ratchet resisting the growing and shrinking of the contact area and leads to a stickslip motion of the contact line. The line is pinned by the first strong-enough obstacle it encounters, so that it is pinned at low contact radius when the contact area grows and at high radius when it shrinks.

In the limit of roughness with small wavelength, $d \to 0$, G_{JKR} does not decrease substantially before the contact line arrests at the next peak (see Fig. 36C). In this limit, the contact line samples the minimum values w_{appr} of w_{loc} during approach and the maximum values w_{retr} during retraction. The functional relationship between b, a and F then becomes identical to the JKR solution for smooth bodies, but with an apparent work of adhesion that is decreased during approach (w_{appr}) and increased during retraction (w_{retr}, see Fig. 36D). In this limit, the hysteresis $w_{retr} - w_{appr}$ becomes equal to the peak-to-peak amplitude of $w_{loc}(a)$ [134].

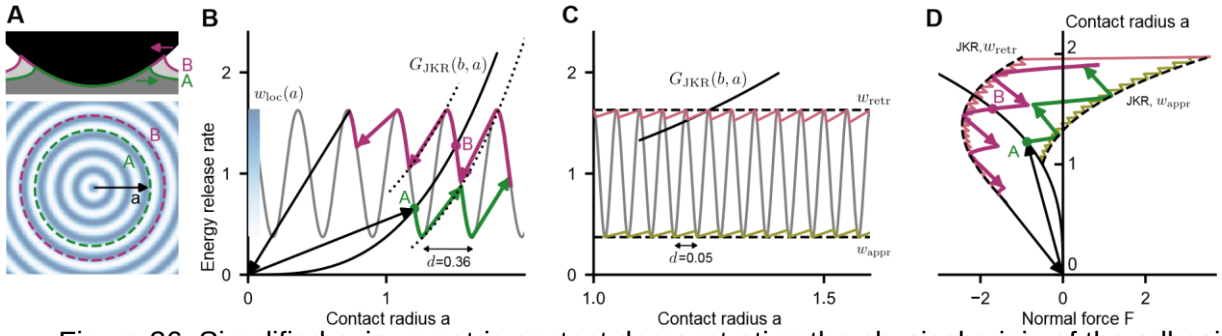

Figure 36: Simplified axisymmetric contact demonstrating the physical origin of the adhesion hysteresis. The indenter is a perfect sphere with axisymmetric heterogeneity in local adhesion $w_{loc}(a)$. **(A)** Cross-section of the contact at rigid-body penetration $b = 0$ (top) and top view of the axisymmetric work-of-adhesion heterogeneity $w_{loc}(a)$ (bottom). The blue color indicates regions of high adhesion. **(B)** Elastic energy release rates in an approach-retraction cycle for a sinusoidal work of adhesion $w_{loc}(a)$ with wavelength $d = 0.36$ (gray line). The black line shows the elastic energy release rate $G_{JKR}(b,a)$ as a function of contact radius for fixed rigid-body penetration $b = 0$. Fluctuations of $w_{loc}(a)$ lead to several metastable states A, B at fixed b. Arrows indicate elastic instabilities where the contact radius jumps between metastable states. **(C)** Energy release rates in an approach-retraction cycle for a work-of-adhesion heterogeneity with smaller wavelength $d = 0.05$. For short wavelengths, the works of adhesion sampled during approach (light green curve) and retraction (light red curve) stay close to the constant values w_{appr} and w_{retr}. **(D)** The contact radius and the normal force during an approach-retraction cycle for wavelength $d = 0.36$ (darker colors) and $d = 0.05$ (lighter colors). The dashed lines are the prediction by the JKR theory using w_{retr} and w_{appr} for the work of adhesion. The solid black line corresponds to increasing energy release rates at fixed rigid-body penetration $b = 0$. Energy release rates are displayed in units of the average work of adhesion and lengths and forces have been nondimensionalized following the conventions of Refs. [137, 138].

E.6.2.2.Random chemical heterogeneity

The next step in complexity is moving from a simplified axisymmetric surface to a surface with random variation of the fracture energy $w_{loc}(x,y)$, where the contact line is no longer perfectly circular (see Fig. 37A). The energy release rate G at a given point now depends on the whole shape of the contact $a(s)$, where s is the length of the corresponding path along the contact circle. Based on the crack-perturbation theory by Gao and Rice [125, 126, 139], we recently derived the approximate expression [125, 127]

$$G(s) = G_{JKR}(a(s)) + c(-\Delta_s)^{1/2}a(s) \qquad \text{Eq. (32)}$$

for the energy-release rate. Equation (32) has a simple interpretation: The adhesive contact line, $a(s)$, behaves like an elastic line. The fractional Laplacian $(-\Delta_s)^{1/2}$ of the contact shape $a(s)$ (see also Eq. (S35)) yields a nonzero restoring force when the contact perimeter is no longer circular. This fractional Laplacian can be interpreted as a generalized curvature, and the prefactor c as the bending stiffness of the line. In the limit of a stiff line, $c \to \infty$, the contact remains circular while in the opposite limit, $c \to 0$, each point s along the contact perimeter can move independently because the restoring force disappears.

We derived Eq. (32) to show that near equilibrium, where $G(s) = w_{int}$, the bending stiffness c of the elastic contact line is equal to w_{int}. Note that counter-intuitively, the bending stiffness does not depend on the elastic modulus of the bulk but only on the intrinsic work of adhesion. Equations (31) and (32) describe the perimeter of the contact as an elastic line pinned by the random field $w_{loc}(x,y)$, and thereby establish an analogy between adhesion and other depinning phenomena [128-130, 140].

Numerical solution of Eqs. (31) and (32) on a random field $w_{loc}(x,y)$ with lateral correlation of length d yields force-area curves similar to those of our axisymmetric model (Fig. 37B,C). The key difference is that the contact line now advances and recedes in jumps (Fig. 37A) that are localized over a characteristic length ℓ, the Larkin length [128-130, 140, 141]. Between these jumps, the contact line is pinned. At the same rigid-body penetration, pinning occurs at lower contact radii during approach than during retraction, leading to a hysteresis in apparent adhesion described by two JKR curves with constant apparent work of adhesion w_{appr} and w_{retr} (Fig. 37C), similar to the curves obtained from our 1D axisymmetric model (Fig. 36D).

The magnitude of hysteresis, $w_{retr} - w_{appr} \propto w_{rms}^2$, where $w_{rms}^2 = \langle (w_{loc} - \langle w_{loc} \rangle)^2 \rangle$ is the variance of the random field w_{loc}. To understand this expression, we first discuss the virtual limit $c \to 0$ where the line is floppy and deviations from circularity are not penalized. Floppy lines ($c < w_{rms}$) can freely distort and meander along valleys during approach (green line in Fig. 37D) and peaks during retraction (purple line). Because of this biased sampling of the work of adhesion along the

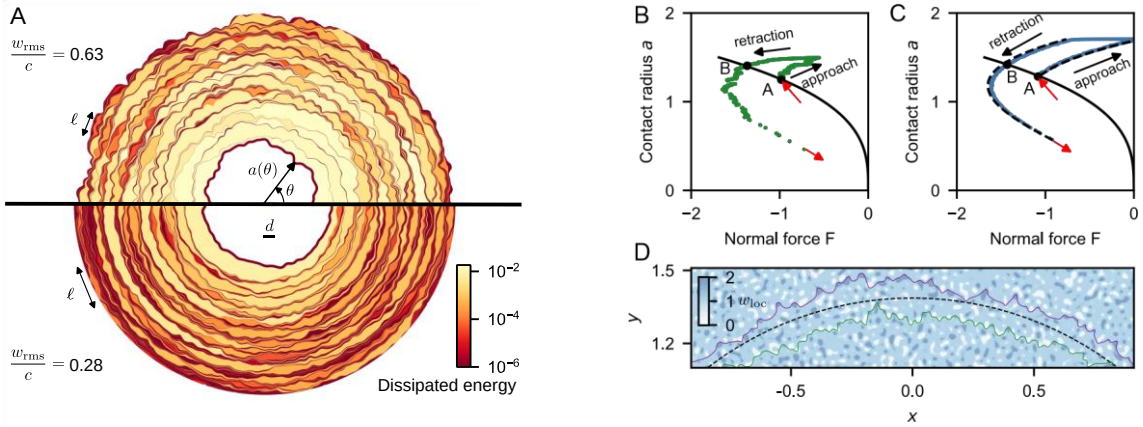

Figure 37: Simulation of crack-front pinning by two-dimensional random heterogeneity. **(A)** Evolution of the contact line during retraction in a crack-front simulation on a 2D random work-of-adhesion field. Each colored patch corresponds to an elastic instability during which the perimeter jumps between two pinned configurations (dark lines), and the color scale represents the energy

dissipated during each instability. The Larkin length ℓ corresponds to the smallest extent of these jumps along the perimeter, and increases for weaker heterogeneity or for a stiffer line. **(B)** Contact radius as a function of the normal force in the simulation shown in the top of panel (A). The elastic instabilities lead to sudden jumps in the contact area and in the normal force. The solid black line corresponds to increasing energy release rates at fixed rigid-body penetration b = 0, and the points A and B show that the contact radius is higher during retraction than during approach. The red arrows show the jump-in and jump-out of contact instabilities. **(C)** Contact radius as a function of the normal force in a simulation on a random chemical heterogeneity with smaller feature size $w_{rms}/c \approx 0.45$. The dashed lines are JKR curves with work of adhesion w_{appr} and w_{retr} predicted by our theory Eq. (6). **(D)** Contact lines at rigid-body penetration $b = 0$ on the random work-of-adhesion heterogeneity shown by the blue colormap. Floppy lines are pinned at higher contact radii during retraction (purple line) than during retraction (green line) because they meander predominantly between regions of low adhesion (white patches) during approach, and between regions of high adhesion (dark blue patches) during retraction. In the limit of a rigid line, the perimeter is perfectly circular (dashed line), randomly sampling as many regions of low and high adhesion.

line, the contact radius is larger during retraction than during approach. In this individual-pinning limit [130, 142, 143], each angle θ along the contact perimeter independently yields our 1D model and we obtain $w_{retr} - w_{appr} \propto w_{rms}$. In the opposite limit, $c \to \infty$ the line is stiff and the contact remains circular (dashed line), randomly sampling as many regions of low and high adhesion. The fluctuations average out along the perimeter so that there is no hysteresis, $w_{retr} - w_{appr} = 0$. The contact radius is then obtained from the JKR expression evaluated for the spatially-averaged work of adhesion, $\langle w_{loc} \rangle$.

Our simulations (and experiments as shown below) are in an intermediate regime, characterized by local jumps over length ℓ or $N = \ell/d$ pinning sites. The line is effectively rigid over the Larkin length ℓ and hence samples a coarse-grained work-of-adhesion field $w^{(\ell)}$ with $w_{rms}^{(\ell)} = w_{rms}/\sqrt{N}$, because the fluctuations average out stochastically over the rigid sections. From the line elasticity, Eq. (32), we obtain that an excursion of the contact line by distance δa over this length leads to a restoring force $\delta G \propto c\delta a/\ell$, which must balance $w_{rms}^{(\ell)}$. We note that $\delta a \approx d$, which is the distance to the closest local stable configuration [128, 129]. The equilibrium condition $\delta G = \omega_{rms}^{(\ell)}$ then yields

$$N \propto (c/w_{rms})^2 \qquad \text{Eq. (33)}$$

where we used $\ell = Nd$. This means, the magnitude of the hysteresis must scale as

$$w_{retr} - w_{appr} \propto w_{rms}^{(\ell)} \propto w_{rms}^2/c \qquad \text{Eq. (34)}$$

exactly as observed in our simulations. Identical results were obtained previously for cracks in heterogeneous media [130, 144].

E.6.2.3.Topographic roughness

The final step in describing the adhesion hysteresis on real surfaces is to relate the random height variations $h(x,y)$, which describe the rough topography, to spatial variations in the fracture energy $w_{loc}(x,y)$. For this we need to consider excursions of the contact line normal to the surface in additional to the lateral excursions that are described by the contact radius $a(\theta)$ (see Fig. 38). First note that the solid is always dilated near the crack tip. In order to conform to a valley, the elastic solid needs to stretch even more, requiring elastic energy. Using the same arguments that lead to Eq. (30), this additional elastic energy manifests as an effectively decreased *local* work of adhesion w_{loc}. Conversely, conforming to a peak decreases the overall strain near the crack tip and releases elastic energy, leading to an increased equivalent work of adhesion. While this intuitive picture approximately describes the relationship between heights and local adhesion, the quantitative value of the local adhesion w_{loc} depends nonlocally on the topographic field $h(x,y)$ via an integral transformation.

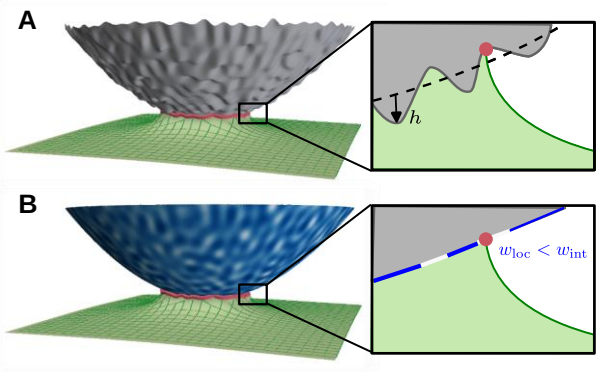

Figure 38: Mapping topographic roughness to equivalent chemical heterogeneity. The contact of a rough sphere (A) is equivalent to the contact of a sphere with a work-of-adhesion heterogeneity w_{loc} (B). The solid is stretched at the crack tip and surface roughness perturbs this elastic deformation. The associated perturbation of the elastic energy can equivalently be described by fluctuations of the work of adhesion.

E.6.2.4.Comparison to experiments

We contacted a rough nanodiamond film with a PDMS hemispherical lens while optically tracing the contact perimeter (see Materials and Methods). The nanodiamond film was characterized from atomic to macroscopic length scales using a variety of techniques, as described in Refs. [47, 131]. The resulting power-spectral density (PSD) [45] comprehensively describes the topography of the film and is shown in Fig. 39A. This experiment is compared to a simulation carried out on a roughness field with an identical PSD, leaving w_{int} as the only free parameter. We determine w_{int} by fitting the approach curves of the simulation and of the experiment. This yields $w_{\mathrm{int}} = 63$ mJ m^{-2}, within the range expected for van-der-Waals interaction.

Our experiments show the same instabilities as the simulations. The trace of the contact line in Fig. 39B shows the jerky motion of the line for both, with comparable amplitudes of deviations from the ideal contact circle. Videos of the contact area in the indentation experiment show stick-slip motion of the contact line, similar to our simulations and to observations by Lyashenko et al. [145] on contact with rubber membranes. The fundamental hysteresis mechanism in our model, elastic instabilities and stick-slip motion of the contact line, is clearly present in the experiment.

Measurements of the mean contact radius as a function of normal force also agree with our simulation results (Fig. 39C). While the simulation was adjusted to follow the experimental data during approach, the match is almost perfect by adjusting only a single parameter, w_{int}. The functional form of the experiment during approach is hence JKR-like with an apparent

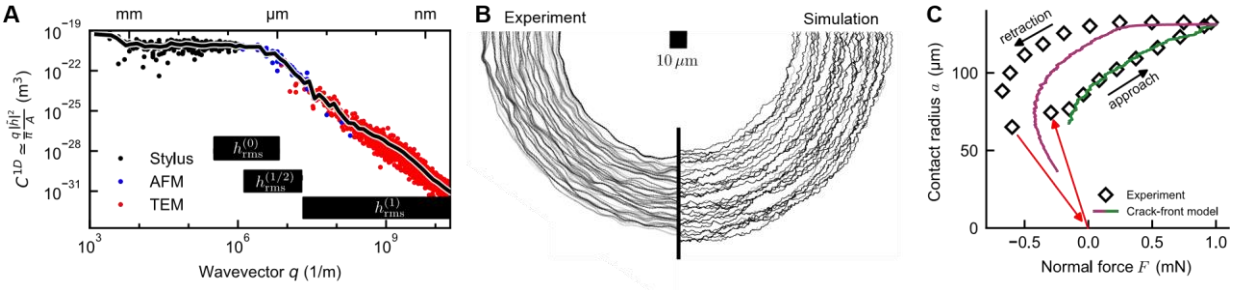

Figure 39: Crack-front pinning explains adhesion hysteresis on real-world surfaces with multiscale roughness. **(A)** Power spectral density (PSD) of a nanocrystalline diamond (NCD) film extracted from more than 60 measurements of Ref. [131], combining stylus profilometry, atomic force microscopy (AFM), and transmission electron microscopy (TEM). Black bars indicate the range of scales that dominates $h_{rms}^{(\alpha)}$ (Eq. (37)). Position of the perimeter in the contact between a rubber sphere and a rough surface during approach. The perimeters on the left side are extracted from the

experiment on NCD shown in Fig. 35, and the right side shows equilibrium positions of the perimeter in a crack perturbation simulation on random roughness similar to NCD. The contact perimeter is pinned where the black lines are close to each other, while regions with low density of lines indicates where the contact perimeter accelerates during an instability. The simulation predicts instabilities of various sizes, reaching a lateral extent up to several tens of μm. In the experiment, only the largest instabilities and the largest features of the contact line are visible because of the limited resolution of the camera and because we removed image noise using a spatially averaging filter. The positions of the perimeter are shown from jump into contact until the force reaches 0.64 mN. **(C)** Contact radius and normal force during approach and retraction of the experiment (diamonds) and simulation (continuous line) shown in panel (B). We extracted the intrinsic work of adhesion $w_{\text{int}} = 63$ mJ/m^2 used in the simulation by fitting the work of approach.

$w_{\text{appr}} \simeq 29$ mJ/m^2. During retraction, we observe the same phenomenology: From the point of largest normal force, the sphere retracts first at a constant contact radius before starting to follow a JKR-like curve with an increased work of adhesion $w_{\text{retr}} \simeq 106$ mJ/m^2. While the simulations retract at slightly different forces, corresponding to $\simeq 71$ mJ/m^2, the order of magnitude of the hysteresis is correctly predicted from our simple elastic model.

E.6.3. DISCUSSION

The matching order of magnitude between our model and the experiment shows that elastic instabilities are an important contribution to the adhesion hysteresis of the real contact. The larger hysteresis in the experiment may originate from other dissipation mechanisms. Indeed, when repeating the experiment in the absence of surface roughness on hydrophobically functionalized surfaces, a hysteresis of $w_{\text{appr}} - w_{\text{retr}} \approx 21$ mJ/m^2 remains. This value corresponds to half of the difference between the measured and the predicted hysteresis. Because these experiments are carried out on smooth contacts, this remaining hysteresis must come from material-specific dissipation processes, most likely viscoelasticity.

We expect the viscoelastic contribution to the hysteresis in the rough contact to be at most as large as on the smooth surface. Viscoelastic energy dissipation increases the apparent work of adhesion at high crack speeds [146, 147]. While the average crack velocities are similar in both experiments, in the rough contact, the local velocity deviates substantially from the average. It either vanishes when the crack front is pinned or is orders of magnitude higher than the average during an instability. When it is pinned, the crack front is immobile and the viscoelastic effects are lower than in the smooth reference experiment. During an instability, the crack accelerates, until dissipation mechanisms such as viscoelasticity become active. However, the total energy dissipated during the instability is predetermined by the energy difference between the quasi-static pinned configurations just before and just after the instability, see Fig. 37A. Any viscoelastic contribution to the adhesive force is determined by the pinned configurations of the crack, where viscoelastic effects are at most as large as in the smooth contact.

Besides material-specific dissipation, quantitative differences could come from approximation or intrinsic assumptions of our model, such as the assumption of fully conforming contact. Contacts conform if the energy needed to fully conform to the surface roughness is much lower than the gain in surface energy, $e_{\text{el}} \ll w_{\text{int}}$ [120, 148]. For $e_{\text{el}} \lesssim w_{\text{int}}$ such as in our experiments, deep valleys may not enter into contact and leave penny-shaped microcracks within the perimeter of the contact. These microcracks likely increase the adhesion hysteresis and the pull-off force because movement of the additional contact lines in the interior of these microcracks will also be subject to pinning by the topographic roughness. However, many experiments report a decrease of pull-off force with increasing roughness, as for example reported in the classic adhesion experiment by Fuller and Tabor [149]. These experiments may be in this limit $e_{\text{el}} > w_{\text{int}}$, where only partial contact is established within the contact circle [121, 148, 150-152]. Unlike the theory presented here for conforming contacts and our understanding of non-adhesive contact [120], there is presently no unifying theory that quantitatively describes adhesion in partial contact. Large-scale simulations with boundary element methods are needed to better understand this intermediate regime [121, 151-155].

We now show that simple analytic estimates can be obtained from our crack-front model. The equivalent work-of-adhesion field has the property that its mean corresponds to the Persson-Tosatti expression, Eq. (30). Furthermore, it has local fluctuations with amplitude $w_{rms} = \sqrt{2w_{int}e_{el}}$ which determine the adhesion hysteresis, see Eq. (34). This equation means that the main parameter determining the hysteresis is e_{el}. We carried out crack-front simulations on self-affine randomly rough topographies (Fig. 37C) to confirm that the apparent work of adhesion during approach and retraction is indeed given by

$$w_{\substack{retr \\ appr}} = w_{int} - e_{el} \pm k e_{el} \qquad \text{Eq. (35)}$$

and to determine the numerical constant $k \simeq 3$. We parametrically varied the roughness to confirm that the main parameter determining adhesion hysteresis is e_{el}. This expression allows us to connect the adhesion hysteresis to statistical parameters of the rough topography. The elastic energy for fully conformal contact can be written as

$$e_{el} = \frac{E'}{4}\left[h_{rms}^{(1/2)}\right]^2 \qquad \text{Eq. (36)}$$

where E' is the elastic contact modulus [156] and $h_{rms}^{(1/2)}$ is a geometric descriptor of the rough topography. In terms of the two-dimensional PSD [45] C^{iso}, we define

$$\left(h_{rms}^{(\alpha)}\right)^2 = \frac{1}{4\pi^2}\int d^2q |\vec{q}|^{2\alpha} C^{iso}(|\vec{q}|) \qquad \text{Eq. (37)}$$

where $\vec{q}$ is the wavevector. This expression contains the root-mean-square (rms) amplitude of the topography, $h_{rms}^{(0)}$, the rms gradient of the topography, $h_{rms}^{(1)}$, as well as arbitrary derivatives of order α. The elastic energy is given by the roughness parameter $h_{rms}^{(1/2)}$, which is intermediate between rms heights and rms gradients.

For most natural and engineered surfaces, $h_{rms}^{(1/2)}$ depends on the large scales, like the rms height, because their Hurst exponent $H > 0.5$ [122, 157-159]. Our model is then consistent with the increase in pull-off force with h_{rms} reported in Refs. [134, 160]. We note that most measurements report insufficient details on surface roughness to allow definite conclusions on the applicability of a certain contact model. The range of length scales that dominate $h_{rms}^{(1/2)}$ in our own experiments is at the transition between power-law scaling and the flat rolloff at 2 μm, a length scale that is accessible with an atomic-force microscope. We illustrate the respective scales that contribute to $h_{rms}^{(\alpha)}$ in Fig. 39A.

The work performed on a soft indenter during the approach-retraction cycle is dissipated in elastic instabilities triggered by surface roughness. The dissipated energy is the difference in energy between the pinned configurations just before and just after the instability. This pinning of the contact line explains why adhesion is always stronger when breaking a soft contact than when making it, even in the absence of material-specific dissipation. Roughness peaks increase local adhesion, which pins the contact line and increases the pull-off force. By describing rough adhesion as the pinning of an elastic line, we were able to derive parameter-free, quantitative expressions for the hysteresis in terms of a simple statistical roughness parameter. This analysis paves the way to better understanding the role of surface roughness in adhesion, and provides guidance for which scales of roughness to control in order to tune adhesion.

E.6.4. MATERIALS AND METHODS

E.6.4.1.Crack-perturbation simulations

We use a crack-perturbation model [125-127] to compute the energy release rate at the perimeter of the contact and solve for equilibrium with the local (equivalent) fracture energy w_{loc} using the algorithm by Rosso and Krauth [161].

E.6.4.2.Rough substrate

We contacted the PDMS lens against a nanocrystalline diamond (NCD) film of known roughness. The diamond film was deposited on a silicon wafer by chemical vapor deposition and subsequently hydrogen terminated to avoid polar interactions and hydrogen bond formation between the PDMS lens and the rough substrate. The roughness of the film was determined by combining measurements from the millimeter to atomic scales using stylus profilometer, atomic force microscopy (AFM), and transmission electron microscopy (TEM). The full experimental dataset along with the averaged PSD shown in Fig. 39B are available online [162]. Details on the film growth and the multiscale topography characterization are provided in Refs. [47, 131].

Evaluating Eq. (37) requires the 2D or isotropic power-spectral density of the surface topography, while only the 1D PSD is known. Following Refs. [45, 54], we converted the 1D PSD C^{1D} to the isotropic 2D PSD using the approximation $C^{\mathrm{iso}}(q) \simeq \pi C^{1D}(q)/q$.

E.6.4.3.Synthesis of PDMS hemispheres

We synthesized PDMS hemispheres of 0.7 MPa Young's modulus by hydrosilylation addition reaction. Vinyl-terminated PDMS V-41 (weight-averaged Molar mass M_w = 62,700 g/mol) as monomer, tetrakis-dimethylsiloxysilane as tetra-functional cross-linker and platinum carbonyl cyclo-vinyl methyl siloxane as catalyst were procured from Gelest Inc. Monomer and cross-linker were first mixed in a molar ratio of 4.4 in an aluminum pan. The catalyst was added as 0.1 weight percent of the total mixture, and finally the batch was degassed in a vacuum chamber for 5 minutes. Hemispherical lenses were cast on fluorinated glass dishes using a needle and a syringe, and cured at 60° C for three days. Since the PDMS mixture has a higher surface energy than the fluorinated surface, the drops maintain a contact angle on the surface, giving a shape of a hemispherical lens. After the curing reaction, the lenses were transferred to cellulose extraction thimble for Soxhlet extraction where toluene refluxes at 130° C for 48 h. PDMS lenses were again transferred to a fluorinated dish and dried in air for 12 h. Finally, the lenses were vacuum dried at 60° C for 16 h and then used for experiments. Before using the lens in the experiment, the radius of curvature R = 1.25mm was measured by fitting a 3-point circle to a profile image obtained using an optical microscope (Olympus).

E.6.4.4.Indentation experiment

We measured the force and area during approach and retraction of a PDMS hemisphere against a rough diamond film using the setup of Dalvi et al. [54]. The lens and the substrate were approached at a constant rate of 60 nm/s until a repulsive force of 1mN and then retracted with the same rate. The PDMS hemisphere is transparent, allowing simultaneous measurement of the force and of the contact area, Fig. 35B. Fig. 39C shows values for the force and contact radius at intervals of ≈ 30s. To remove the influence of roughness, we also carried out reference experiments on a flat silicon wafer covered with hydrophobic octadecyltrichlorosilane (OTS). The Young's modulus E = 0.7 MPa of the PDMS sphere was obtained by fitting the JKR theory to these experiments (see also Ref. [54]).

E.6.4.5.Extraction of contact line from video

We extracted the perimeter from each time frame of the video of the contact area. The contact area appears as a bright region in the video, and we defined the contact perimeter as a contour line of fixed level of gray. At the length scale of a few pixels, the position of the line is affected by noise on the image. To reduce the effect of noise on the position of the line, we subtracted the image of the contact

area at maximum penetration and subsequently applied a spatial Gaussian filter of variance 2 pixels. The lines shown in Fig. 39B therefore only reflect the position of the perimeter on coarse scales.

E.7. References for Scientific Report

1. Randolph, A.B., et al., *The need for better metrics for floor-tile topography: Conventional metrics correlate only modestly with shoe-floor friction.* Tribology International, 2024. **193**: p. 109366.
2. Beschorner, K.E., E. Ibata-Arens, and T.D.B. Jacobs. *Using Dynamic Mechanical Analysis to Evaluate Shoe Floor Friction Performance*. 2022; Available from: https://ctherm.com/resources/newsroom/dma/shoe_friction/.
3. Beschorner, K.E., et al., *Validating the ability of a portable shoe-floor friction testing device, NextSTEPS, to predict human slips.* Applied ergonomics, 2023. **106**: p. 103854.
4. Meehan, E.E., N. Vidic, and K.E. Beschorner, *In contrast to slip-resistant shoes, fluid drainage capacity explains friction performance across shoes that are not slip-resistant.* Applied ergonomics, 2022. **100**: p. 103663.
5. Beschorner, K.E. and A.B. Randolph, *Friction performance of resilient flooring under contaminant conditions relevant to healthcare settings.* Applied ergonomics, 2023. **108**: p. 103960.
6. Iraqi, A., et al., *Coefficient of friction testing parameters influence the prediction of human slips.* Applied Ergonomics, 2018. **70**: p. 118-126.
7. Albert, D.L., B. Moyer, and K.E. Beschorner, *Three-dimensional shoe kinematics during unexpected slips: Implications for shoe-floor friction testing.* IIE: Transactions on Occupational Ergonomics and Human Factors, 2017. **5**(1): p. 1-11.
8. Beschorner, K.E., et al., *Influence of averaging time-interval on shoe-floor-contaminant available coefficient of friction measurements.* Applied ergonomics, 2020. **82**: p. 102959.
9. Moghaddam, S.R.M., M.S. Redfern, and K.E. Beschorner, *A Microscopic Finite Element Model of Shoe–Floor Hysteresis and Adhesion Friction.* Tribology Letters, 2015. **59**(3): p. 1-10.
10. Strobel, C.M., et al., *Analysis of the contribution of adhesion and hysteresis to shoe–floor lubricated friction in the boundary lubrication regime.* Tribology Letters, 2012. **47**(3): p. 341-347.
11. Cowap, M., et al., *Contributions of adhesion and hysteresis to coefficient of friction between shoe and floor surfaces: effects of floor roughness and sliding speed.* Tribology-Materials, Surfaces & Interfaces, 2015. **9**(2): p. 77-84.
12. Jones, T.G., A. Iraqi, and K.E. Beschorner, *Performance testing of work shoes labeled as slip resistant.* Applied ergonomics, 2018. **68**: p. 304-312.
13. Moore, C.T., et al., *Analysis of shoe friction during sliding against floor material: role of fluid contaminant.* Journal of Tribology, 2012. **134**(4): p. 041104.
14. Hemler, S., D. Charbonneau, and K. Beschorner, *Predicting hydrodynamic conditions under worn shoes using the tapered-wedge solution of Reynolds equation.* Tribology International, 2020: p. 106161.
15. Hemler, S., et al., *Changes in Under-Shoe Traction and Fluid Drainage for Progressively Worn Shoe Tread.* Applied ergonomics, 2019. **80**(October 2019): p. 35-42.
16. Walter, P.J., et al., *Effect of tread design and hardness on interfacial fluid force and friction in artificially worn shoes.* Footwear Science, 2021. **13**(3): p. 245-254.
17. Moghaddam, S.R., et al., *Predictive Multiscale Computational Model of Shoe-Floor Coefficient of Friction.* Journal of Biomechanics, 2018. **66**: p. 145-152.
18. Wilkinson, M.D., et al., *The FAIR Guiding Principles for scientific data management and stewardship.* Scientific data, 2016. **3**(1): p. 1-9.
19. ASME, *B46.1 - 2019: Surface Texture (Surface Roughness, Waviness, and Lay)*. 2020, ASME: New York, NY.
20. Chang, W.-R., et al., *The effect of surface waviness on friction between Neolite and quarry tiles.* Ergonomics, 2004. **47**(8): p. 890-906.
21. Randolph, A.B., et al., *Data Set for Manuscript: The need for better metrics for floor-tile topography: Conventional metrics correlate only modestly with shoe-floor friction*. 2023.

22. Chang, W.-R., et al., *The role of surface roughness in the measurement of slipperiness.* Ergonomics, 2001. **44**(13): p. 1200-1216.
23. Chang, W.-R., et al., *Linear regression models of floor surface parameters on friction between Neolite and quarry tiles.* Applied ergonomics, 2010. **41**(1): p. 27-33.
24. Ezzat, F., W. Ali, and A. Hasouna, *Friction Coefficient of Rubber Sliding Against Polymeric Indoor Flooring Materials of Different Surface Roughness.* Journal of the Egyptian Society of Tribology, 2008. **4**(4): p. 37-45.
25. Verma, S.K., et al., *A prospective study of floor surface, shoes, floor cleaning and slipping in US limited-service restaurant workers.* Occupational and environmental medicine, 2011. **68**(4): p. 279-285.
26. Heinrich, G., M. Klüppel, and T.A. Vilgis, *Evaluation of self-affine surfaces and their implication for frictional dynamics as illustrated with a Rouse material.* Computational and Theoretical Polymer Science, 2000. **10**(1-2): p. 53-61.
27. Persson, B.N., *Theory of rubber friction and contact mechanics.* The Journal of Chemical Physics, 2001. **115**(8): p. 3840-3861.
28. Beschorner, K.E., et al., *Fluid Pressures at the Shoe-Floor-Contaminant Interface During Slips: Effects of Tread & Implications on Slip Severity.* Journal of Biomechanics, 2014. **47**(2): p. 458-463.
29. Singh, G. and K.E. Beschorner, *A Method for Measuring Fluid Pressures in the Shoe-Floor-Fluid Interface: Application to Shoe Tread Evaluation.* IIE Transactions on Occupational Ergonomics and Human Factors, 2014. **2**(2): p. 53-59.
30. Ding, R., et al., *Going beyond traditional roughness metrics for floor tiles: Measuring topography down to the nanoscale.* Tribology Letters, 2021. **69**(3): p. 1-12.
31. Chang, W.R., et al., *The role of friction in the measurement of slipperiness, Part 1: friction mechanisms and definition of test conditions.* Ergonomics, 2001. **44**(13): p. 1217-32.
32. Sundaram, V., et al., *Worn Region Size of Shoe Soles Impacts Human Slips: Testing a Mechanistic Model.* Journal of biomechanics, 2020: p. 109797.
33. Greenwood, J.A. and J.P. Williamson, *Contact of nominally flat surfaces.* Proceedings of the royal society of London. Series A. Mathematical and physical sciences, 1966. **295**(1442): p. 300-319.
34. Iraqi, A., et al., *Prediction of coefficient of friction based on footwear outsole features.* Applied ergonomics, 2020. **82**: p. 102963.
35. Tari, G., et al., *Classification of hard floor coverings according to their contribution to reduce the risk of pedestrian slipping.* 2009.
36. Nishi, T., et al., *Influence of unforced dewetting and enforced wetting on real contact formation and friction behavior between rubber hemisphere and glass plate during contacting and sliding processes.* Tribology International, 2020. **141**: p. 105921.
37. Shibata, K., et al., *Effect of groove width and depth and urethane coating on slip resistance of vinyl flooring sheet in glycerol solution.* Tribology International, 2019. **135**: p. 89-95.
38. Mate, C.M., *Tribology on the small scale: a bottom up approach to friction, lubrication, and wear*. 2008: Oxford University Press.
39. Maksuta, D., et al., *Dependence of adhesive friction on surface roughness and elastic modulus.* Soft Matter, 2022. **18**(31): p. 5843-5849.
40. Khanal, S.R., et al., *Characterization of small-scale surface topography using transmission electron microscopy.* Surface Topography: Metrology and Properties, 2018. **6**(4): p. 045004.
41. Zeng, H., et al., *Boron-doped ultrananocrystalline diamond synthesized with an H-rich/Ar-lean gas system.* Carbon, 2015. **84**: p. 103-117.
42. Vander Voort, G.F., *Metallography, principles and practice*. 1999: ASM international.
43. Jacobs, T.D., et al., *The effect of atomic-scale roughness on the adhesion of nanoscale asperities: A combined simulation and experimental investigation.* Tribology Letters, 2013. **50**: p. 81-93.
44. Krolczyk, G., et al., *Surface morphology analysis of duplex stainless steel (DSS) in clean production using the power spectral density.* Measurement, 2016. **94**: p. 464-470.

45. Jacobs, T.D., T. Junge, and L. Pastewka, *Quantitative characterization of surface topography using spectral analysis.* Surface Topography: Metrology and Properties, 2017. **5**(1): p. 013001.
46. Röttger, M.C., et al., *Contact. engineering—Create, analyze and publish digital surface twins from topography measurements across many scales.* Surface Topography: Metrology and Properties, 2022. **10**(3): p. 035032.
47. Gujrati, A., et al., *Combining TEM, AFM, and profilometry for quantitative topography characterization across all scales.* ACS applied materials & interfaces, 2018. **10**(34): p. 29169-29178.
48. Chrostowski, R. and F. Mangolini, *On the nature and propagation of errors in roughness parameters obtained from spectral analysis of atomic force microscopy topographic images.* Journal of Vacuum Science & Technology A, 2022. **40**(5).
49. Chrostowski, R., et al., *Monte-Carlo evaluation of bias and variance in Hurst exponents computed from power spectral analysis of atomic force microscopy topographic images.* Applied Surface Science, 2022. **581**: p. 152092.
50. Russ, J.C. and J.C. Russ, *Hurst and Fourier analysis.* Fractal Surfaces, 1994: p. 83-114.
51. Church, E.L. and P.Z. Takacs. *Instrumental effects in surface finish measurement*. in *Surface measurement and characterization*. 1989. SPIE.
52. Reimer, L., *Scanning electron microscopy: physics of image formation and microanalysis.* Measurement Science and Technology, 2000. **11**(12): p. 1826-1826.
53. Nolze, G., *Image distortions in SEM and their influences on EBSD measurements.* Ultramicroscopy, 2007. **107**(2-3): p. 172-183.
54. Dalvi, S., et al., *Linking energy loss in soft adhesion to surface roughness.* Proceedings of the National Academy of Sciences, 2019. **116**(51): p. 25484-25490.
55. Thimons, L.A., et al., *Hard-material adhesion: Which scales of roughness matter?* Experimental Mechanics, 2021. **61**(7): p. 1109-1120.
56. ISO, *ISO 21920-2 Geometrical Product Specifications (GPS) — Surface texture: Profile method — Terms, definitions, and surface texture parameters*. 2021, International Organization for Standardization.
57. ASME, *ASME B46.1: Surface Texture (Surface Roughness, Waviness, and Lay)*. 2019, American Society of Mechanical Engineers.
58. Liu, Y. and G. Glass, *Effects of mesh density on finite element analysis*. 2013, SAE Technical Paper.
59. Ing, H., *Prediction of Oily Shoe-Floor Friction Using a Multiscale Hysteresis Mechanics Model*. 2024, University of Pittsburgh, Pittsburgh, PA. p. 92.
60. Albert, D., B. Moyer, and K.E. Beschorner, *Three-dimensional shoe kinematics during unexpected slips: implications for shoe–floor friction testing.* IISE Transactions on Occupational Ergonomics and Human Factors, 2017. **5**(1): p. 1-11.
61. Iraqi, A., et al., *Kinematics and kinetics of the shoe during human slips.* Journal of biomechanics, 2018. **74**: p. 57-63.
62. Centeno Gil, O.J., *Finite Element Modeling of Rubber Bushing for Crash Simulation-Experimental Tests and Validation.* 2009.
63. Suh, J.B., *Stress analysis of rubber blocks under vertical loading and shear loading*. 2007, University of Akron.
64. Chadha, V., et al., *Evaluating scanning electron microscopy for the measurement of small-scale topography.* Surface Topography: Metrology and Properties, 2024.
65. Cowap, M.J., et al., *Contributions of adhesion and hysteresis to coefficient of friction between shoe and floor surfaces: effects of floor roughness and sliding speed.* Tribology-Materials, Surfaces & Interfaces, 2015. **9**(2): p. 77-84.
66. Moghaddam, S.R.M., M.S. Redfern, and K.E. Beschorner, *A microscopic finite element model of shoe–floor hysteresis and adhesion friction.* Tribology letters, 2015. **59**: p. 1-10.
67. Strobel, C.M., et al., *Analysis of the contribution of adhesion and hysteresis to shoe–floor lubricated friction in the boundary lubrication regime.* Tribology Letters, 2012. **47**: p. 341-347.
68. Ding, R., et al., *Going beyond traditional roughness metrics for floor tiles: Measuring topography down to the nanoscale.* Tribology Letters, 2021. **69**(3): p. 92.

69. Hemler, S.L., D.N. Charbonneau, and K.E. Beschorner, *Predicting hydrodynamic conditions under worn shoes using the tapered-wedge solution of Reynolds equation.* Tribology international, 2020. **145**: p. 106161.
70. Moore, C. and K. Beschorner, *Effect of Shoe Roughness on Shoe-Floor Lubrication.* Research and Practice for Fall Injury Control in the Workplace: p. 105.
71. Beschorner, K.E., et al., *Effects of slip testing parameters on measured coefficient of friction.* Applied ergonomics, 2007. **38**(6): p. 773-780.
72. Chang, W.-R., et al., *The role of friction in the measurement of slipperiness, Part 1: Friction mechanisms and definition of test conditions.* Ergonomics, 2001. **44**(13): p. 1217-1232.
73. Persson, B.N., et al., *On the nature of surface roughness with application to contact mechanics, sealing, rubber friction and adhesion.* Journal of physics: Condensed matter, 2004. **17**(1): p. R1.
74. Moghaddam, S.R.M., et al., *Predictive multiscale computational model of shoe-floor coefficient of friction original article.* Journal of biomechanics, 2017.
75. Beschorner, K.E., et al., *Prospective validity assessment of a friction prediction model based on tread outsole features of slip-resistant shoes.* Applied Ergonomics, 2024. **114**: p. 104110.
76. Jakobsen, L., et al., *Dynamic and static friction measurements of elastomer footwear blocks on ice surface.* Tribology International, 2023. **178**: p. 108064.
77. Li, K.W. and C.J. Chen, *The effect of shoe soling tread groove width on the coefficient of friction with different sole materials, floors, and contaminants.* Applied ergonomics, 2004. **35**(6): p. 499-507.
78. Li, K.W., H.H. Wu, and Y.-C. Lin, *The effect of shoe sole tread groove depth on the friction coefficient with different tread groove widths, floors and contaminants.* Applied ergonomics, 2006. **37**(6): p. 743-748.
79. Jackson, R. and T. Jacobs, *Which asperity scales matter for true contact area? A multi-scale and statistical investigation.* Mechanics of Materials, 2023. **184**: p. 104746.
80. Gujrati, A., et al. *Ultrananocrystalline diamond (UNCD) (Version 2).* https://doi.org/10.57703/ce-5cz7a. 2022; Available from: https://contact.engineering.
81. Kogut, L. and R.L. Jackson, *A Comparison of Contact Modeling Utilizing Statistical and Fractal Approaches.* Journal of Tribology, 2005. **128**(1): p. 213-217.
82. Sayles, R.S. and T.R. Thomas, *Surface topography as a nonstationary random process.* Nature, 1978. **271**(5644): p. 431-434.
83. Majumdar, A. and C.L. Tien, *Fractal characterization and simulation of rough surfaces.* Wear, 1990. **136**(2): p. 313-327.
84. Green, I., *Exact Spectral Moments and Differentiability of the Weierstrass-Mandelbrot Fractal Function.* Journal of Tribology, 2019. **142**(4).
85. Christopher, A.B., et al., *Multiscale analyses and characterizations of surface topographies.* CIRP Annals, 2018. **67**(2): p. 839-862.
86. Kalin, M., et al., *Comparing surface topography parameters of rough surfaces obtained with spectral moments and deterministic methods.* Tribology international, 2016. **93**: p. 137-141.
87. McCool, J.I., *Comparison of models for the contact of rough surfaces.* Wear, 1986. **107**(1): p. 37-60.
88. Sanner, A., et al., *Scale-dependent roughness parameters for topography analysis.* Applied Surface Science Advances, 2022. **7**: p. 100190.
89. McCool, J., *Finite difference spectral moment estimation for profiles the effect of sample spacing and quantization error.* Precision Engineering, 1982. **4**(4): p. 181-184.
90. McCool, J.I., *Relating profile instrument measurements to the functional performance of rough surfaces.* 1987.
91. Mohr, M., et al., *Young's modulus, fracture strength, and Poisson's ratio of nanocrystalline diamond films.* Journal of Applied Physics, 2014. **116**(12): p. 124308.
92. Randall, R.B., *State of the art in monitoring rotating machinery-part 1.* Sound and vibration, 2004. **38**(3): p. 14-21.
93. Jackson, R.L., *An Analytical Solution to an Archard-Type Fractal Rough Surface Contact Model.* Tribology Transactions, 2010. **53**(4): p. 543-553.

94. Wilson, W.E., S.V. Angadi, and R.L. Jackson, *Surface Separation and Contact Resistance Considering Sinusoidal Elastic-Plastic Multi-Scale Rough Surface Contact.* Wear, 2010. **268**(1-2): p. 190-201.
95. Archard, J., *Elastic deformation and the laws of friction.* Proceedings of the royal society of London. Series A. Mathematical and physical sciences, 1957. **243**(1233): p. 190-205.
96. Ciavarella, M. and G. Demelio, *Elastic multiscale contact of rough surfaces: Archard's model revisited and comparisons with modern fractal models.* Journal of Applied Mechanics, 2001. **68**(3): p. 496-498.
97. Jackson, R.L. and J.L. Streator, *A multi-scale model for contact between rough surfaces.* Wear, 2006. **261**(11-12): p. 1337-1347.
98. Chu, N.R., et al., *Evaluating Elastic-Plastic Wavy and Spherical Asperity-Based Statistical and Multi-Scale Rough Surface Contact Models with Deterministic Results.* Materials, 2021. **14**(14): p. 3864.
99. An, B., et al., *Deterministic elastic-plastic modelling of rough surface contact including spectral interpolation and comparison to theoretical models.* Tribology International, 2019. **135**: p. 246-258.
100. Thimons, L.A., et al., *Hard-material Adhesion: Which Scales of Roughness Matter?* Experimental Mechanics, 2021. **61**(7): p. 1109-1120.
101. Jackson, R.L., et al. *A simplified model of multiscale electrical contact resistance and comparison to existing closed form models*. in *2009 Proceedings of the 55th IEEE Holm Conference on Electrical Contacts*. 2009. IEEE.
102. Krithivasan, V. and R.L. Jackson, *An analysis of three-dimensional elasto-plastic sinusoidal contact.* Tribology Letters, 2007. **27**(1): p. 31-43.
103. Manners, W., *Plastic deformation of a sinusoidal surface.* Wear, 2008. **264**(1-2): p. 60-68.
104. Jackson, R.L. and I. Green, *A statistical model of elasto-plastic asperity contact between rough surfaces.* Tribology International, 2006. **39**(9): p. 906-914.
105. Johnson, K., J. Greenwood, and J. Higginson, *The contact of elastic regular wavy surfaces.* International journal of mechanical sciences, 1985. **27**(6): p. 383-396.
106. Ghaednia, H., et al., *A Review of Elastic–Plastic Contact Mechanics.* Applied Mechanics Reviews, 2017. **69**(6).
107. Jackson, R.L., *The effect of scale-dependent hardness on elasto-plastic asperity contact between rough surfaces.* Tribology Transactions, 2006. **49**(2): p. 135-150.
108. Jackson, R.L., E.R. Crandall, and M.J. Bozack, *Rough surface electrical contact resistance considering scale dependent properties and quantum effects.* Journal of Applied Physics, 2015. **117**(19): p. 195101.
109. Fleck, N.A., Muller, G. M., Ashby, M. F., Hutchinson, J. W., *Strain Gradient Plasticity: Theory and Experiment.* Acta Metall. Mater., 1994. **42**(2): p. pp. 475-487.
110. Nix, W.D., Gao, H., *Indentation size effects in crystalline materials: a law for strain gradient plasticity.* J. Mech. Phys. Solids, 1998. **46**: p. pp. 411-425.
111. Ashby, M.F., H. Shercliff, and D. Cebon, *Materials: engineering, science, processing and design*. 2018: Butterworth-Heinemann.
112. Mo, Y., D. Stone, and I. Szlufarska, *Strength of ultrananocrystalline diamond controlled by friction of buried interfaces.* Journal of Physics D: Applied Physics, 2012. **45**(6): p. 069501.
113. Krauss, A.R., et al., *Ultrananocrystalline diamond thin films for MEMS and moving mechanical assembly devices.* Diamond and Related Materials, 2001. **10**(11): p. 1952-1961.
114. Rostami, A. and R.L. Jackson, *Predictions of the average surface separation and stiffness between contacting elastic and elastic–plastic sinusoidal surfaces.* Proceedings of the Institution of Mechanical Engineers, Part J: Journal of Engineering Tribology, 2013. **227**(12): p. 1376-1385.
115. Liu, S., et al., *Contacting Micro Asperity of a Deformable Surface.* Journal of Tribology, 2023: p. 1-31.
116. Bush, A.W., R.D. Gibson, and T.R. Thomas, *The elastic contact of a rough surface.* Wear, 1975. **35**(1): p. 87-111.

117. Sanner, A., et al., *Why soft contacts are stickier when breaking than when making them.* Science Advances, 2024. **10**(10): p. eadl1277.
118. Israelachvili, J.N., *Intermolecular and Surface Forces* 1991, London: Academic Press.
119. Johnson, K.L., K. Kendall, and A.D. Roberts, *Surface energy and the contact of elastic solids.* Proceedings of the Royal Society of London. A. Mathematical and Physical Sciences, 1971. **324**(1558): p. 301-313.
120. Persson, B.N.J., et al., *On the nature of surface roughness with application to contact mechanics, sealing, rubber friction and adhesion.* Journal of Physics: Condensed Matter, 2005. **17**(1): p. R1.
121. Pastewka, L. and M.O. Robbins, *Contact between rough surfaces and a criterion for macroscopic adhesion.* Proceedings of the National Academy of Sciences, 2014. **111**(9): p. 3298-3303.
122. Persson, B.N.J. and E. Tosatti, *The effect of surface roughness on the adhesion of elastic solids.* The Journal of Chemical Physics, 2001. **115**(12): p. 5597-5610.
123. Chaudhury, M.K. and G.M. Whitesides, *Direct measurement of interfacial interactions between semispherical lenses and flat sheets of poly (dimethylsiloxane) and their chemical derivatives.* Langmuir, 1991. **7**(5): p. 1013-1025.
124. Chen, Y., C. Helm, and J. Israelachvili, *Molecular mechanisms associated with adhesion and contact angle hysteresis of monolayer surfaces.* The journal of physical chemistry, 1991. **95**(26): p. 10736-10747.
125. Gao, H. and J.R. Rice, *Nearly circular connections of elastic half spaces.* 1987.
126. Rice, J.R., *Weight function theory for three-dimensional elastic crack analysis*. 1989: ASTM International.
127. Sanner, A. and L. Pastewka, *Crack-front model for adhesion of soft elastic spheres with chemical heterogeneity.* Journal of the Mechanics and Physics of Solids, 2022. **160**: p. 104781.
128. Larkin, A. and Y.N. Ovchinnikov, *Pinning in type II superconductors.* Journal of Low Temperature Physics, 1979. **34**: p. 409-428.
129. Robbins, M.O. and J.-F. Joanny, *Contact angle hysteresis on random surfaces.* Europhysics letters, 1987. **3**(6): p. 729.
130. Démery, V., A. Rosso, and L. Ponson, *From microstructural features to effective toughness in disordered brittle solids.* Europhysics Letters, 2014. **105**(3): p. 34003.
131. Gujrati, A., et al., *Comprehensive topography characterization of polycrystalline diamond coatings.* Surface Topography: Metrology and Properties, 2021. **9**(1): p. 014003.
132. Griffith, A.A., *VI. The phenomena of rupture and flow in solids.* Philosophical transactions of the royal society of london. Series A, containing papers of a mathematical or physical character, 1921. **221**(582-593): p. 163-198.
133. Guduru, P., *Detachment of a rigid solid from an elastic wavy surface: theory.* Journal of the Mechanics and Physics of Solids, 2007. **55**(3): p. 445-472.
134. Kesari, H., et al., *Role of surface roughness in hysteresis during adhesive elastic contact.* Philosophical Magazine & Philosophical Magazine Letters, 2010. **90**(12): p. 891-902.
135. Kesari, H. and A.J. Lew, *Effective macroscopic adhesive contact behavior induced by small surface roughness.* Journal of the Mechanics and Physics of Solids, 2011. **59**(12): p. 2488-2510.
136. Popov, V.L., *Adhesion hysteresis due to chemical heterogeneity.* Multiscale biomechanics and tribology of inorganic and organic systems: In memory of professor Sergey Psakhie, 2021: p. 473-483.
137. Barthel, E., *Adhesive elastic contacts: JKR and more.* Journal of Physics D: Applied Physics, 2008. **41**(16): p. 163001.
138. Maugis, D., *Contact, adhesion and rupture of elastic solids*. Vol. 130. 2013: Springer Science & Business Media.
139. Rice, J., *First-order variation in elastic fields due to variation in location of a planar crack front.* 1985.
140. Monti, J.M. and M.O. Robbins, *Sliding friction of amorphous asperities on crystalline substrates: Scaling with contact radius and substrate thickness.* ACS nano, 2020. **14**(12): p. 16997-17003.

141. Imry, Y. and S.-k. Ma, *Random-field instability of the ordered state of continuous symmetry.* Physical Review Letters, 1975. **35**(21): p. 1399.
142. Joanny, J. and P.-G. De Gennes, *A model for contact angle hysteresis.* The journal of chemical physics, 1984. **81**(1): p. 552-562.
143. Patinet, S., D. Vandembroucq, and S. Roux, *Quantitative prediction of effective toughness at random heterogeneous interfaces.* Physical Review Letters, 2013. **110**(16): p. 165507.
144. Démery, V., V. Lecomte, and A. Rosso, *The effect of disorder geometry on the critical force in disordered elastic systems.* Journal of Statistical Mechanics: Theory and Experiment, 2014. **2014**(3): p. P03009.
145. Lyashenko, I.A. and R. Pohrt, *Adhesion between rigid indenter and soft rubber layer: Influence of roughness.* Frontiers in Mechanical Engineering, 2020. **6**: p. 49.
146. Persson, B. and E. Brener, *Crack propagation in viscoelastic solids.* Physical Review E—Statistical, Nonlinear, and Soft Matter Physics, 2005. **71**(3): p. 036123.
147. Müser, M.H. and B.N. Persson, *Crack and pull-off dynamics of adhesive, viscoelastic solids.* Europhysics Letters, 2022. **137**(3): p. 36004.
148. Persson, B., *Adhesion between elastic bodies with randomly rough surfaces.* Physical review letters, 2002. **89**(24): p. 245502.
149. Fuller, K. and D. Tabor, *The effect of surface roughness on the adhesion of elastic solids.* Proceedings of the Royal Society of London. A. Mathematical and Physical Sciences, 1975. **345**(1642): p. 327-342.
150. Mulakaluri, N. and B. Persson, *Adhesion between elastic solids with randomly rough surfaces: Comparison of analytical theory with molecular-dynamics simulations.* Europhysics Letters, 2011. **96**(6): p. 66003.
151. Pastewka, L. and M.O. Robbins, *Contact area of rough spheres: Large scale simulations and simple scaling laws.* Applied Physics Letters, 2016. **108**(22).
152. Wang, A. and M.H. Müser, *Is there more than one stickiness criterion?* Friction, 2023. **11**(6): p. 1027-1039.
153. Medina, S. and D. Dini, *A numerical model for the deterministic analysis of adhesive rough contacts down to the nano-scale.* International Journal of Solids and Structures, 2014. **51**(14): p. 2620-2632.
154. Popov, V.L., R. Pohrt, and Q. Li, *Strength of adhesive contacts: Influence of contact geometry and material gradients.* Friction, 2017. **5**: p. 308-325.
155. Popov, V.L., et al., *Adhesion and friction in hard and soft contacts: Theory and experiment.* Friction, 2021. **9**: p. 1688-1706.
156. Johnson, K.L., *Contact mechanics*. 1987: Cambridge university press.
157. Mandelbrot, B.B., D.E. Passoja, and A.J. Paullay, *Fractal character of fracture surfaces of metals.* Nature, 1984. **308**(5961): p. 721-722.
158. Candela, T., et al., *Roughness of fault surfaces over nine decades of length scales.* Journal of Geophysical Research: Solid Earth, 2012. **117**(B8).
159. Persson, B., *On the fractal dimension of rough surfaces.* Tribology Letters, 2014. **54**: p. 99-106.
160. Briggs, G. and B. Briscoe, *Effect of surface roughness on rolling friction and adhesion between elastic solids.* Nature, 1976. **260**(5549): p. 313-315.
161. Rosso, A. and W. Krauth, *Roughness at the depinning threshold for a long-range elastic string.* Physical Review E, 2002. **65**(2): p. 025101.
162. Abhijeet, G., et al., *Nanocrystalline Diamond (Version 2).* 2023.

F.Publications

F.1. Journal Article:

1. Jackson R, Jacobs T. Which asperity scales matter for true contact area? A multi-scale and statistical investigation. *Mechanics of Materials*. 2023 September;184:104746-. DOI: 10.1016/j.mechmat.2023.104746.
2. Jacobs TDB, Pastewka L. Surface topography as a material parameter. *MRS bulletin*. 2022;47(12):1205-1210. PubMed PMID: 36846501; PubMed Central PMCID: PMC9947057; DOI: 10.1557/s43577-022-00465-5.
3. Randolph AB, Reifler K, Chadha V, Jacobs TD, Beschorner KE. The need for better metrics for floor-tile topography: Conventional metrics correlate only modestly with shoe-floor friction. *Tribology International*. 2024 February 13;193:109366. https://doi.org/10.1016/j.triboint.2024.109366
4. Chadha V, Miller NC, Ding R. Evaluating scanning electron microscopy for the measurement of small-scale topography. Surface Topography: Metrology and Properties. 2024 July 15;12(3):035010. https://doi.org/10.1088/2051-672X/ad49b9
5. Sanner A, Kumar N, Dhinojwala A, Jacobs TDB, Pastewka L. Why soft contacts are stickier when breaking than when making them. Science advances. 2024 March 8;10(10):eadl1277. PubMed PMID: 38446897; PubMed Central PMCID: PMC10917342; DOI: 10.1126/sciadv.adl1277.

F.2. Conference Proceedings & Abstracts:

1. Beschorner, K.E., Ing, H., Chadha, V., Randolph, A., Reifler, K. and Jacobs, T., 2023, Shoe-floor friction is predicted by high-frequency material properties and small-scale floor topographical features, Footwear Biomechanics Symposium, Osaka, Japan, July 26-28, 2023.

F.3. Dissertation/Thesis

1. Ing, H., 2024, Prediction of Oily Shoe-Floor Friction Using a Multiscale Hysteresis Mechanics Model, MS Thesis, University of Pittsburgh.

G.Inclusion Enrollment Table

Not applicable since there were not human participants.

H.Materials Available for Other Investigators*

1. Randolph, A.B., Reifler, K., Chadha, V., Jacobs, T.D.B., Beschorner, K.E., 2023. Data Set for Manuscript: The need for better metrics for floor-tile topography: Conventional metrics correlate only modestly with shoe-floor friction, http://d-scholarship.pitt.edu/id/eprint/45780.
2. Surface topography data (from flooring and other materials) have been published through contact.engineering. The following DOIs (organized by study) are now publicly available.
    a. Randolph, A.B., Reifler, K., Chadha, V., Jacobs, T.D. and Beschorner, K.E., 2024. The need for better metrics for floor-tile topography: Conventional metrics correlate only modestly with shoe-floor friction. *Tribology International*, 193, p.109366. See Study #1 for more details.
        i. APOL: https://doi.org/10.57703/ce-zcpbh
        ii. AUPS: https://doi.org/10.57703/ce-mdqfs
        iii. AH1: https://doi.org/10.57703/ce-9wzs6
        iv. AH2: https://doi.org/10.57703/ce-2j7be
        v. BPOL: https://doi.org/10.57703/ce-bpczg
        vi. BUPS: https://doi.org/10.57703/ce-cxyn8
        vii. CUPS: https://doi.org/10.57703/ce-8tzq3
        viii. EUPS: https://doi.org/10.57703/ce-b3tjf

ix. EHON: https://doi.org/10.57703/ce-4pq7x
x. FUPS: https://doi.org/10.57703/ce-57etj
xi. FSAT: https://doi.org/10.57703/ce-nu46d
xii. LMBP: https://doi.org/10.57703/ce-6qy4a
xiii. LMBM: https://doi.org/10.57703/ce-ynqrq
xiv. LMBS: https://doi.org/10.57703/ce-r5cau
xv. PPM: https://doi.org/10.57703/ce-wkq6z
xvi. PPP: https://doi.org/10.57703/ce-j5qtr
xvii. PBS: https://doi.org/10.57703/ce-yhzx9
xviii. PPS: https://doi.org/10.57703/ce-v6t8p
xix. PSW: https://doi.org/10.57703/ce-zaf32
xx. UMBP: https://doi.org/10.57703/ce-g4cym
xxi. UMBM: https://doi.org/10.57703/ce-crtwt
xxii. UMBS: https://doi.org/10.57703/ce-wbp5n
xxiii. VPOL: https://doi.org/10.57703/ce-mg4cy

b. Chadha, V., Miller N.C., Ding, R., Beschorner, K.E. and Jacobs, T.D., 2024. Evaluating scanning electron microscopy for the measurement of small-scale topography. *Surface Topography: Metrology and Properties*, 12, 035010. See Study #2 for more details.
   i. SEM-measured topography data for UNCD, created using Method 1: Wedge Deposition: https://doi.org/10.57703/ce-zwcjk
   ii. SEM-measured topography data for UNCD, created using Method 2: Simple Fracture: https://doi.org/10.57703/ce-mqta3
   iii. SEM-measured topography data for UNCD, created using Method 3: Mechanically Polished: https://doi.org/10.57703/ce-b6ptc
   iv. SEM-measured topography data for UNCD, created using Method 4: Ion Polished: https://doi.org/10.57703/ce-c57vn

c. Ing, H., Chadha, V., Randolph, A.B., Reifler, K., Jacobs, T.D.B. and Beschorner K.E. Validation of a multiscale hysteresis mechanics model in predicting oily shoe-floor friction across surfaces with varying finishes. ASME Journal of Tribology, **in revision**. See Studies #3 and 4 for more details.
   i. Floor 1: APOL: https://doi.org/10.57703/ce-8g7m7
   ii. Floor 2: AUPS: https://doi.org/10.57703/ce-2kt9w
   iii. Floor 3: BPOL: https://doi.org/10.57703/ce-gqp5a
   iv. Floor 4: BUPS: https://doi.org/10.57703/ce-6hyry
   v. Floor 5: CEXT: https://doi.org/10.57703/ce-pdqvs
   vi. Floor 6: CUPS: https://doi.org/10.57703/ce-rcce5
   vii. Floor 7: PBS: https://doi.org/10.57703/ce-5rett
   viii. Floor 8: PPM: https://doi.org/10.57703/ce-n94jp
   ix. Floor 9: PPP: https://doi.org/10.57703/ce-bzt2h
   x. Floor 10: PPS: https://doi.org/10.57703/ce-4mqh9

d. Jackson, R., Jacobs, T., 2023. Which asperity scales matter for true contact area? A multi-scale and statistical investigation. *Mechanics of Materials* 184, 104746. See Study #5 for more details.
   i. UNCD: https://doi.org/10.57703/ce-5cz7a

e. Sanner, A., Kumar, N., Dhinojwala, A., Jacobs, T.D. and Pastewka, L., 2024. Why soft contacts are stickier when breaking than when making them. Science Advances, 10(10), p.eadl1277. See Study #6 for more details.
   i. Adhesion Data: https://doi.org/10.5281/zenodo.10591746

* Note that data sets will be released for Studies #3 and #4 upon publication similar to the data set that was published for Study #1.

C. PRODUCTS

C.1 PUBLICATIONS

Are there publications or manuscripts accepted for publication in a journal or other publication (e.g., book, one-time publication, monograph) during the reporting period resulting directly from this award?

Yes

Publications Reported for this Reporting Period

Public Access Compliance	Citation
N/A: Not NIH Funded	Jackson R, Jacobs T. Which asperity scales matter for true contact area? A multi-scale and statistical investigation. Mechanics of Materials. 2023 September;184:104746-. DOI: 10.1016/j.mechmat.2023.104746.
N/A: Not NIH Funded	Chadha V, Miller NC, Ding R. Evaluating scanning electron microscopy for the measurement of small-scale topography. Surface Topography: Metrology and Properties. 2024 July 15;12(3):035010.
N/A: Not NIH Funded	Randolph AB, Reifler K, Chadha V, Jacobs TDB, Beschorner KE. The need for better metrics for floor-tile topography: Conventional metrics correlate only modestly with shoe-floor friction. Tribology international. 2024 May;193. PubMed PMID: 39781403; PubMed Central PMCID: PMC11708304; DOI: 10.1016/j.triboint.2024.109366.
N/A: Not NIH Funded	Randolph AB, Reifler K, Chadha V, Jacobs TDB, Beschorner KE. The need for better metrics for floor-tile topography: Conventional metrics correlate only modestly with shoe-floor friction. Tribology international. 2024 May;193. PubMed PMID: 39781403; PubMed Central PMCID: PMC11708304; DOI: 10.1016/j.triboint.2024.109366.

C.2 WEBSITE(S) OR OTHER INTERNET SITE(S)

NOTHING TO REPORT

C.3 TECHNOLOGIES OR TECHNIQUES

NOTHING TO REPORT

C.4 INVENTIONS, PATENT APPLICATIONS, AND/OR LICENSES

Have inventions, patent applications and/or licenses resulted from the award during the reporting period? No

If yes, has this information been previously provided to the PHS or to the official responsible for patent matters at the grantee organization? No

C.5 OTHER PRODUCTS AND RESOURCE SHARING

Category	Explanation
Data or Databases	Chadha, V., Miller N.C., Ding, R., Beschorner, K.E. and Jacobs, T.D., 2024. Evaluating scanning electron microscopy for the measurement of small-scale topography. Surface Topography: Metrology and Properties, 12, 035010. See Study #2 for more details. 1. SEM-measured topography data for UNCD, created using Method 1: Wedge Deposition: https://doi.org/10.57703/ce-zwcjk 2. SEM-measured topography data for UNCD, created using Method 2: Simple Fracture: https://doi.org/10.57703/ce-mqta3 3. SEM-measured topography data for UNCD, created using Method 3: Mechanically Polished: https://doi.org/10.57703/ce-b6ptc 4. SEM-measured topography data for UNCD, created using Method 4: Ion Polished: https://doi.org/10.57703/ce-c57vn
Data or Databases	Surface topography data (from flooring and other materials) have been published through contact.engineering. The following DOIs are now publicly available for the study: Sanner, A., Kumar, N., Dhinojwala, A., Jacobs, T.D. and Pastewka, L., 2024. Why soft contacts are stickier when breaking than when making them.Science Advances,10(10), p.eadl1277. See Study #6 for more details. 1. UNCD: https://doi.org/10.57703/ce-5cz7a
Data or Databases	Surface topography data (from flooring and other materials) have been published through contact.engineering. The following DOIs are now publicly available for the study: Jackson, R., Jacobs, T., 2023. Which asperity scales matter for true contact area? A multi-scale and statistical investigation. Mechanics of Materials 184, 104746. See Study #5 for more details. 1. UNCD: https://doi.org/10.57703/ce-5cz7a
Data or Databases	Surface topography data (from flooring and other materials) have been published through contact.engineering. The following DOIs are now publicly available for the study: Ing, H., Chadha, V., Randolph, A.B., Reifler, K., Jacobs, T.D.B. and Beschorner K.E. Validation of a multiscale hysteresis mechanics model in predicting oily shoe-floor friction across surfaces with varying finishes. ASME Journal of Tribology, in revision. See Studies #3 and 4 for more details. 1. Floor 1: APOL: https://doi.org/10.57703/ce-8g7m7 2. Floor 2: AUPS: https://doi.org/10.57703/ce-2kt9w 3. Floor 3: BPOL: https://doi.org/10.57703/ce-gqp5a 4. Floor 4: BUPS: https://doi.org/10.57703/ce-6hyry 5. Floor 5: CEXT: https://doi.org/10.57703/ce-pdqvs 6. Floor 6: CUPS: https://doi.org/10.57703/ce-rcce5 7. Floor 7: PBS: https://doi.org/10.57703/ce-5rett 8. Floor 8: PPM: https://doi.org/10.57703/ce-n94jp 9. Floor 9: PPP: https://doi.org/10.57703/ce-bzt2h 10. Floor 10: PPS: https://doi.org/10.57703/ce-4mqh9

Category	Explanation
Data or Databases	Surface topography data (from flooring and other materials) have been published through contact.engineering. The following DOIs are now publicly available for the study: Randolph, A.B., Reifler, K., Chadha, V., Jacobs, T.D. and Beschorner, K.E., 2024. The need for better metrics for floor-tile topography: Conventional metrics correlate only modestly with shoe-floor friction.Tribology International,193, p.109366. See Study #1 for more details. 1. APOL: https://doi.org/10.57703/ce-zcpbh 2. AUPS: https://doi.org/10.57703/ce-mdqfs 3. AH1: https://doi.org/10.57703/ce-9wzs6 4. AH2: https://doi.org/10.57703/ce-2j7be 5. BPOL: https://doi.org/10.57703/ce-bpczg 6. BUPS: https://doi.org/10.57703/ce-cxyn8 7. CUPS: https://doi.org/10.57703/ce-8tzq3 8. EUPS: https://doi.org/10.57703/ce-b3tjf 9. EHON: https://doi.org/10.57703/ce-4pq7x 10. FUPS: https://doi.org/10.57703/ce-57etj 11. FSAT: https://doi.org/10.57703/ce-nu46d 12. LMBP: https://doi.org/10.57703/ce-6qy4a 13. LMBM: https://doi.org/10.57703/ce-ynqrq 14. LMBS: https://doi.org/10.57703/ce-r5cau 15. PPM: https://doi.org/10.57703/ce-wkq6z 16. PPP: https://doi.org/10.57703/ce-j5qtr 17. PBS: https://doi.org/10.57703/ce-yhzx9 18. PPS: https://doi.org/10.57703/ce-v6t8p 19. PSW: https://doi.org/10.57703/ce-zaf32 20. UMBP: https://doi.org/10.57703/ce-g4cym 21. UMBM: https://doi.org/10.57703/ce-crtwt 22. UMBS: https://doi.org/10.57703/ce-wbp5n 23. VPOL: https://doi.org/10.57703/ce-mg4cy
Data or Databases	Randolph, A.B., Reifler, K., Chadha, V., Jacobs, T.D.B., Beschorner, K.E., 2023. Data Set for Manuscript: The need for better metrics for floor-tile topography: Conventional metrics correlate only modestly with shoe-floor friction, http://d-scholarship.pitt.edu/id/eprint/45780.

D. PARTICIPANTS

D.1 WHAT INDIVIDUALS HAVE WORKED ON THE PROJECT?

Commons ID	Sr/Key	Name	Degree(s)	Role	Cal	Aca	Sum	Foreign Org	Country	SS
BESCHORNER	Y	Beschorner, Kurt E	BS,PHD	PD/PI	1.2	0.0	0.0			NA
TDBJACOBS	Y	Jacobs, Tevis		PD/PI	1.9	0.0	0.0			NA
	N	Ing, Henry		GSR who left institution without Commons ID	12.0	0.0	0.0			NA

Glossary of acronyms:
Sr/Key - Senior/Key
Cal - Person Months (Calendar)
Aca - Person Months (Academic)
Sum - Person Months (Summer)
Foreign Org - Foreign Organization Affiliation
SS - Supplement Support
RS - Reentry Supplement
DS - Diversity Supplement
OT - Other
NA - Not Applicable

D.2 PERSONNEL UPDATES

D.2.a Level of Effort

Not Applicable

D.2.b New Senior/Key Personnel

Not Applicable

D.2.c Changes in Other Support

Not Applicable

D.2.d New Other Significant Contributors

Not Applicable

D.2.e Multi-PI (MPI) Leadership Plan

Not Applicable

E. IMPACT

E.1 WHAT IS THE IMPACT ON THE DEVELOPMENT OF HUMAN RESOURCES?

Not Applicable

E.2 WHAT IS THE IMPACT ON PHYSICAL, INSTITUTIONAL, OR INFORMATION RESOURCES THAT FORM INFRASTRUCTURE?

NOTHING TO REPORT

E.3 WHAT IS THE IMPACT ON TECHNOLOGY TRANSFER?

Not Applicable

E.4 WHAT DOLLAR AMOUNT OF THE AWARD'S BUDGET IS BEING SPENT IN FOREIGN COUNTRY(IES)?

NOTHING TO REPORT

G. SPECIAL REPORTING REQUIREMENTS SPECIAL REPORTING REQUIREMENTS

G.1 SPECIAL NOTICE OF AWARD TERMS AND NOTICE OF FUNDING OPPORTUNITIES REPORTING REQUIREMENTS

NOTHING TO REPORT

G.2 RESPONSIBLE CONDUCT OF RESEARCH

Not Applicable

G.3 MENTOR'S REPORT OR SPONSOR COMMENTS

Not Applicable

G.4 HUMAN SUBJECTS

G.4.a Does the project involve human subjects?

Not Applicable

G.4.b Inclusion Enrollment Data

NOTHING TO REPORT

G.4.c ClinicalTrials.gov

Does this project include one or more applicable clinical trials that must be registered in ClinicalTrials.gov under FDAAA?

G.5 HUMAN SUBJECTS EDUCATION REQUIREMENT

NOT APPLICABLE

G.6 HUMAN EMBRYONIC STEM CELLS (HESCS)

Does this project involve human embryonic stem cells (only hESC lines listed as approved in the NIH Registry may be used in NIH funded research)?

No

G.7 VERTEBRATE ANIMALS

Not Applicable

G.8 PROJECT/PERFORMANCE SITES

Not Applicable

G.9 FOREIGN COMPONENT

No foreign component

G.10 ESTIMATED UNOBLIGATED BALANCE

Not Applicable

G.11 PROGRAM INCOME

Not Applicable

G.12 F&A COSTS

Not Applicable

I. OUTCOMES

I.1 What were the outcomes of the award?

The primary goal of this R21 study was to use novel measurements of small-scale floor topography to develop and validate a mechanics-based predictive model for shoe-floor friction. This project was motivated by the high rate of slip-and-fall accidents and the opportunity for high friction footwear and flooring to ameliorate the impacts of these injurious events. In this research study, we developed novel methods to characterize the topography of flooring across 7 orders of magnitude and characterized time-dependent shoe materials across 9 orders of magnitude. We developed an implementation of a friction mechanics model to predict coefficient of friction based on these inputs. Shoe-floor coefficient of friction data was collected in oily conditions for 184 shoe-floor combinations to assess the ability of traditional roughness metrics as well as mechanics models to predict shoe-floor friction. We implemented both statistical analyses and mechanics-based analyses to determine the predictive ability of floor topography across different scale ranges. The key accomplishment in this study was the validation of such a computational model that predicts the impact of time-dependent shoe materials and scale-dependent flooring topography. This model has high potential for impact given its high degree of accuracy for predicting oily friction, the extensive validation that was performed in this study demonstrating its ability to predict both impacts of flooring and shoe materials, and its low required level of expertise required to use the model. The implementation of the model was made possible because of advances in characterizing flooring surfaces and shoe materials that were facilitated during this research. The model also revealed the scales of flooring topography and the frequencies of shoe materials that contribute most to oily friction. Thus, findings of the model already have generated knowledge that inform design for footwear and flooring manufacturers.